Vorticity Dynamics of Hydrodynamic Instabilities Occurring at Material Interfaces:
Application to High-Energy-Density Systems

by

Samuel Pellone

A dissertation submitted in partial fulfillment
of the requirements for the degree of
Doctor of Philosophy
(Mechanical Engineering)
in The University of Michigan
2021

Doctoral Committee:

Associate Professor Eric Johnsen, Chair
Dr. Carlos Di Stefano
Professor Robert Krasny
Associate Professor Carolyn Kuranz
Assistant Professor Aaron Towne

Samuel Pellone
spellone@umich.edu
ORCID iD: 0000-0001-8234-7179

DEDICATION

To my parents and my wife.

ACKNOWLEDGMENTS

"By faith we understand that the worlds were framed by the word of God, so that the things which are seen were not made of things which are visible."
— Hebrews 11:3

I would like to first acknowledge my advisor, Prof. Eric Johnsen, for his mentorship over the last five years as a PhD graduate student. Prof. Johnsen welcomed me to the Scientific Computing and Flow Physics Laboratory even before starting my PhD, as a Master student to finish my Master's degree. I am very grateful to him for giving me this opportunity and a chance to succeed in the US. I extend my gratitude to my committee members, Dr. Carlos Di Stefano, Prof. Robert Krasny, Prof. Carolyn Kuranz, and Prof. Aaron Towne. I am very grateful to Prof. Krasny and Prof. Ling Xu for their numerous and valuable discussions and help on the point insertion procedure applied to the vortex-sheet model.

This section would be incomplete without acknowledging my family and the friendships developed at the University of Michigan. Thank you to all my labmates that I had the pleasure to work with but also to know on a personal level. I am very grateful to Harish, who became a dear friend of mine with whom I had the pleasure to share deep philosophical, metaphysical, and personal conversations. To Suyash for all the shared coffee breaks and his knowledge of the next high-performance computing technology, to Mauro for his in-depth white board analyses, first-class analogies and metaphors, and our shared-passion of basketball, to Marc

for being against using a mouse and doing everything in a Linux terminal, for his helpful advice during my early graduate years, his inspiring work ethic, and our kayak adventures, to Brandon for partaking in respectful conversations about our different political and religious opinions, his valuable guidance on graduate life, and his candid friendship, to Siddhesh for sharing a tent at Brandon's wedding (Despacito man!), to Kevin for his funny cartoon animations and his interest in getting to know people's personalities, to Griffin for his fishing stories and terminal-commands cheat sheet, to Minki for living in the lab, to Mike for his eloquent and amazing presentations and his mushroom stories, to Kazuya for building his own computer and his tenacity toward spherical harmonics, to Eunhye for her turbulence knowledge, to Phil for refusing to use a smartphone, to Shahab for coming in at 5pm and working in the lab all night, to Lauren for her inspiring work-life balance while pursing a PhD and an MD, to Pooya for his help on VisIt, to Adaleena for her passion for dogs, to TJ for going together to progressive rock concerts, to Brian for his house parties and happy hours, to Justin for the long soccer game at my house, to John for experiencing an NFL football game, to Louise for sharing her life stories, to Joel for his relaxed mindset and his running skills, to Stephanie for all the treats she baked, to Greg for his knowledge on OpenACC, to Ali for sharing his coffee grounds, and to Sarah for early-morning conversations about graduate life.

I would like to further acknowledge my family and friends that know me beyond the lab. I am ever grateful to my parents, Christian and Isabelle, for their love and education they gave me, and having always encouraged me to pursue my dreams. But more importantly, they are also my spiritual parents, and I am so blessed to be able to share my faith with them on a deep level. Their journey in the ministry is a true inspiration, and I love our deep conversations about the universe, the Lord, and the secrets revealed in the Torah. To my amazing sister, Pri, for never

giving up and her selflessness. Thank you to Jan and Rog, my American parents, who welcomed me in their home as their own son. They gave me everything to be able to succeed in the US, and they are the reason why I was able to start pursuing my dream in America. This PhD would not have been possible without them. To Steve and Cyndi, my in-laws, who have always supported me and make me feel welcome and a part of their family. To my close friends from high-school and church, J'aib for his phenomenal six-pack, Bast for our ever-ending one-on-one basketball game, and Franck for his inspiring life journey and the brotherly bond we still share. This PhD journey would not have been the same without my wife, Missy, who has been by my side since the first day, through the hills and valleys of a PhD student. Through her love, grace, and encouragements, I came farther than I could have ever imagined, and I cannot wait to see and embrace the rest of my journey with her. I am ever grateful to God for having put her on my path and excited to share this bonding love forever.

This work was supported in part by the National Science Foundation under grant no. PHY-1707260 and by the Los Alamos National Laboratory under contract 89233218CNA000001 with Triad National Security LLC.

TABLE OF CONTENTS

LIST OF FIGURES

Figure

LIST OF TABLES

Table

LIST OF APPENDICES

Appendix

ABSTRACT

Inertia-dominated hydrodynamic instabilities at material interfaces are ubiquitous phenomena observed in nature and man-made applications, spanning core collapse supernovae, inertial confinement fusion, supersonic combustion, and cavitation bubble collapse. When subjected to accelerations, perturbations along an interface may grow due to the Rayleigh-Taylor (RT) or Richtmyer-Meshkov (RM) instability, while in the presence of shear, they may grow due to the Kelvin-Helmholtz (KH) instability. The main focus of this thesis is the RM instability.

The RM instability occurs when a perturbed interface separating two fluids of different densities is impulsively accelerated, e.g., by the passage of a shock wave. During the interaction of the shock with the interface, baroclinic vorticity is generated along the interface due to the misalignment between the density and pressure gradients, thus leading to perturbation growth. The subsequent interface evolution can be described using vorticity dynamics. Although the early stage of vorticity deposition along the interface is relatively well understood, the late-time vorticity dynamics and their effects on the interface evolution are less well known. Our objective is to understand the role of vorticity dynamics in the late-time evolution of RM-type problems. To examine the vorticity dynamics of the RM instability, we implement a vortex-sheet model allowing us to isolate the different contributions of vorticity production in the evolution of the interface.

We first use the vortex-sheet model to understand the relative importance between RM and KH in the evolution of perturbations subjected to an oblique shock under

high-energy-density (HED) conditions. At early times, the perturbation growth is dominated by the impulsive acceleration of the shock (RM), as evidenced by our proposed scaling accounting for the normal and tangential components of the shock. At later times, the perturbation growth is modulated by the positive and negative vorticity generated by the shear and the decompression due to the arrival of the rarefaction produced by laser turn off. As the tilt angle is increased, the onset of the shear-dominated dynamics occurs earlier and becomes more pronounced. We further demonstrate the ability of the vortex-sheet model to reproduce roll-up dynamics for non-zero Atwood numbers by comparing to past laser-driven HED experiments.

We then explain the mechanisms of vorticity generation in the late-time evolution of the single-mode RM instability. In particular, we explore the generation of secondary opposite-sign vorticity occurring inside the roll-ups as the interface spirals inward. We show that, in the case of a zero Atwood number (i.e., matched density at the interface), opposite-sign vorticity never develops. In this case, the vorticity distribution along the interface is only governed by the rate of change of the sheet surface. Near the vortex core, the rate of change of the sheet surface alternates between positive and negative values, indicating that the interface near the vortex core undergoes a series of contractions and expansions, thus giving rise to oscillations in the corresponding sheet strength. These oscillations have a frequency corresponding to approximately half the orbital frequency of the points along the interface. In the case of small Atwood numbers, performing a vorticity budget suggests that opposite-sign vorticity is generated by the nonlinear vorticity advection along the interface. The onset of this opposite-sign vorticity generation is referred to as the onset time. To quantify the amount of opposite-sign vorticity generated along the interface, we consider positive and negative circulations, and their dependence of the strength of the incident shock and the Atwood number. For a positive

Atwood number (i.e., light-to-heavy) in the range $0.2 \leq A \leq 0.8$, we show that after a short time following the onset time, opposite-sign (negative) circulation behaves as $\sim t^{-3/2}$. When varying the strength of the incident shock, we discover that the interface evolution scales in time with respect to the shock Mach number, resulting in the curves of opposite-sign circulation vs. time to collapse onto one.

Finally, we discuss how the vortex-sheet model may be appropriately initialized to study the vorticity dynamics of finite-size perturbations

CHAPTER 1

The Occurrence of Hydrodynamic Instabilities

This chapter introduces fundamental concepts needed to understand the occurrence of inertia-dominated hydrodynamic instabilities at material interfaces relevant to natural phenomena and man-made applications. A brief review of canonical instabilities is presented, and their relevance to high-energy-density applications motivate the focus of this work. Finally, I lay down the objective and overview of this thesis, along with contributions.

1.1 Fundamental concepts

The fundamental problem of hydrodynamic stability may be traced back to the pioneering work of Reynolds (1883) on the transition of a smooth laminar flow in a pipe to a turbulent state. Reynolds (1883) observed that this transition occurs at a critical velocity, sensitive to some disturbances at the inlet of the tube. Below the critical velocity, small disturbances do not grow and the flow is stable, whereas above the critical velocity, small disturbances grow exponentially and the flow is unstable. The problem of hydrodynamic stability can be described as being that of finding whether small disturbances introduced in a steady-state flow grow, and if so, whether these disturbances grow to reach a new equilibrium, or if the flow breaks down to turbulence. Several tools are available to study the time evolution of small disturbances (or perturbations). If the amplitude of the perturbations is small compared to the relevant state variables of the base flow, and that the latter is steady, a linear stability analysis may be performed using the method of normal modes (Chandrasekhar, 2013; Drazin

& Reid, 2004). The governing equations are linearized about small sinusoidal perturbations to the base flow, and solutions growing exponentially in time are sought in the form e^{nt}, for some complex number n. Beyond the linear growth of perturbations, the method of normal modes does not apply, as the modes cannot be considered linearly independent due to the rise of non-linearities, causing different modes to interact with each other. One approach to couple non-linear effects to growing perturbations, known as weakly non-linear stability analysis (Landau, 1944), is to account for higher-order terms in the Taylor expansion of the growth rate in powers of the perturbation amplitude. Eventually, the non-linear effects become so important that theoretical analyses become intractable, requiring the use of computational methods. With the latter, all stages of perturbation growth, from early exponential growth to late turbulent and chaotic state, can be described.

Hydrodynamic instabilities are ubiquitous in many areas of science and occur in a wide range of engineering applications and natural phenomena. Their occurrence affects systems of all size in the spectrum of length scales; from millimeter-size to stellar-size objects. The type of instabilities that may grow in a system depends on the physical mechanisms driving the instability. The system may contain a single fluid or multiple fluids, which can be at rest or in motion, ionized, in thermal equilibrium or transporting heat, subjected to accelerations, etc. A dimensional analysis based on the characteristic scales of the system can be useful in determining the relative importance of the different mechanisms involved. For example, the breakup of a liquid jet into droplets, which is dependent upon the Rayleigh-Plateau instability, can be described as a competition between the destabilizing action of surface tension, and the stabilizing action of fluid inertia. The Rayleigh-Bénard instability, which occurs when a fluid layer is heated from below is an example of a thermal instability, controlled by the relative importance of the destabilizing force of buoyancy and the stabilizing thermal diffusion.

The present thesis focuses on inertially driven hydrodynamic instabilities, where the equilibrium of the external forces is perturbed by the presence of fluid accelerations and/or

velocity gradients. Such instabilities typically occur in high-Reynolds number flows, where viscous stresses can be considered small compared to the fluid inertia.

1.2 Inertia-driven hydrodynamic instabilities at interfaces

Hydrodynamic instabilities give rise to fluid mixing and affect the overall flow dynamics of the system in which they occur. Material interfaces are found in flows involving density inhomogeneities, i.e., multi-fluid flows, and physically represent the mutual boundary between different fluids present in a system. When subjected to accelerations, small perturbations on the interface may grow due to the Rayleigh-Taylor (RT) or the Richtmyer-Meshkov (RM) instability, while in the presence of shear, they may grow due to the Kelvin-Helmholtz (KH) instability. Each one of these instabilities is important in a wide range of applications, and are briefly described below.

1.2.1 The Kelvin-Helmholtz instability

The Kelvin-Helmholtz instability (Thomson Lord Kelvin, 1871; Helmholtz, 1868) is a shear instability, i.e., occurring when two parallel streams move at different nominal velocities. The instability is characterized by the formation of billows, or co-rotating vortices, which eventually may break down to turbulence. Examples where this instability is observed in nature and engineering applications are shown in Figure 1.1. The interaction between solar winds and the boundary layer of planetary atmospheres has been shown to lead to the growth of the KH instability (Masters *et al.*, 2010, 2009; Johnson *et al.*, 2014), as illustrated in Figure 1.1a. On a much smaller scale, the stability of a round jet coming out of a nozzle in propulsion systems, is greatly affected by the KH instability, leading to a turbulent combustion region (Yule *et al.*, 1981), as illustrated in Figure 1.1b. The mechanism of the KH instability can be described in different ways. If the separating shear layer is a rippled

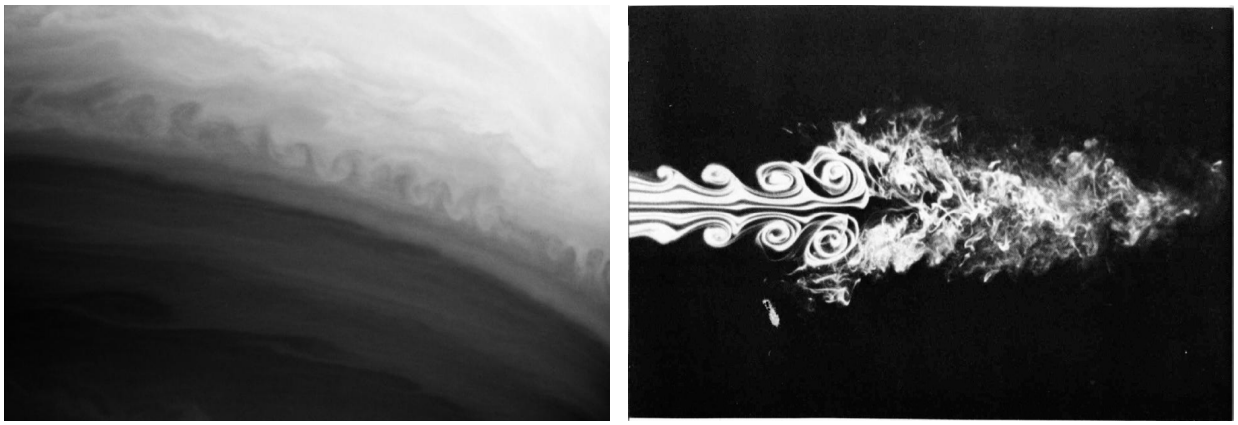

(a) KH billows in Saturn's atmosphere. (b) KH billows along a round jet.

Figure 1.1: Examples of the Kelvin-Helmholtz instability. Photographs credit: (a) National Aeronautics and Space Administration (Cassini spacecraft), and (b) R. Drubka and H. Nagib (Van Dyke, 1982).

interface, the fluid velocity near the crest (on one side of the interface) and trough (on the other side of the interface) increases, due to a reduction of the cross-sectional area, creating a "Bernoulli effect". A lift force, similar to that experienced by airfoils, is therefore created on each side of the interface, leading to exponential growth of the perturbation amplitude (Charru, 2011). Batchelor (2000) provides a description of the KH instability in terms of vorticity. The flows on each side of the interface can be considered irrotational, such that the only non-zero vorticity in the system is at the interface, due to the sharp velocity gradient. The vorticity is distributed along the interface (usually sinusoidally), and induces a velocity on the interface itself, which, in the case of incompressible fluids, can be determined from the Biot-Savart law. According to the Biot-Savart law, the x-component of a point velocity located on the interface depends on the y-coordinate difference between that point and the other points along the interface. As such, the x-component of the velocity for points located on the crests is opposite to that of the points located on the troughs. As a result, the fluid tends to rotate around points located halfway between crests and troughs, leading to the perturbation growth. In both approaches, the linear stability analysis yields the same

perturbation growth rate

$$n = -ik\frac{\rho_1 U_1 + \rho_2 U_2}{\rho_1 + \rho_2} \pm \sqrt{\frac{k^2 \rho_1 \rho_2 \Delta U^2}{(\rho_1 + \rho_2)^2}}, \tag{1.1}$$

where $\rho_{1,2}$ and $U_{1,2}$ are the densities and velocities on each side of the interface, respectively, $\Delta U = U_1 - U_2$, and k is the perturbation wavenumber. The imaginary part does not contribute to exponential growth, but only adds modulations. The operand under the square root is always positive, showing that the positive mode of the real part is always unstable given $\Delta U \neq 0$. If $\rho_1 = \rho_2$, we recognize the familiar growth rate, $n = \frac{k\Delta U}{2}$, and shows that perturbations are subjected to the KH instability even if there is no density gradient across the interface (as long as $\Delta U \neq 0$).

1.2.2 The Rayleigh-Taylor instability

The Rayleigh-Taylor instability (Rayleigh, 1900; Taylor, 1950) occurs when a heavier fluid is accelerated into a lighter one, causing any disturbance at the interface to grow. The RT instability results in the interpenetration of the two fluids, eventually leading to a turbulent mixing region. A particular case is when a heavy fluid lies on the top of a relatively lighter fluid subjected to the action of gravity. A force balance between the weight of the heavy fluid and buoyancy shows that the light fluid rises into the heavy fluid (analogous to an air bubble rising into water), while the heavy fluid falls into the light fluid as a spike. Figure 1.2a shows an example of buoyant clouds forming a mushroom-like shape rising into the Earth's atmosphere. The formation of supernovae from the collapse of dying stars involves the development of filament structures due to the RT instability, causing material mixing with the interstellar medium, as illustrated in Figure 1.2b. A generalization of the buoyancy-driven configuration is whenever a heavy fluid is accelerated or decelerated into a lighter fluid, causing a pressure gradient, $\boldsymbol{\nabla} P$, in the direction opposite to that of the density gradient, $\boldsymbol{\nabla}\rho$, i.e., $\boldsymbol{\nabla} P \cdot \boldsymbol{\nabla}\rho < 0$. As for the KH instability, the mechanism of RT instability

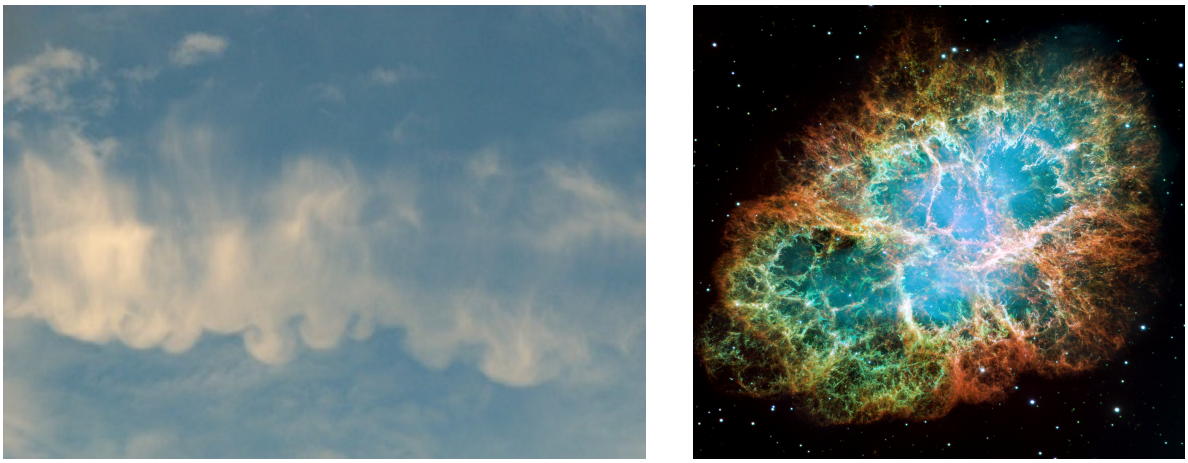

(a) Buoyant clouds due to RT instability. (b) RT filaments in Crab nebula.

Figure 1.2: Examples of the Rayleigh-Taylor instability. Photographs credit: (a) Prof. David Jewitt, University of California, Los Angeles. From Zhou (2017*a*), reproduced with permission from Elsevier, Copyright (2017), and (b) National Aeronautics and Space Administration (Hubble Space Telescope).

can be described in terms of vorticity (Roberts & Jacobs, 2016). The misalignment of the pressure gradient, from the acceleration of the heavy fluid into the lighter fluid, with the density gradient at the interface, generates baroclinic vorticity along the interface, such that $\boldsymbol{\nabla}\rho \times \boldsymbol{\nabla}P \neq 0$, which amplifies any perturbation due to the induced velocity, as illustrated in Figure 1.3. In the canonical case of two incompressible, inviscid fluids, with no surface tension, the linear stability analysis reveals that a small perturbation of initial amplitude η_0

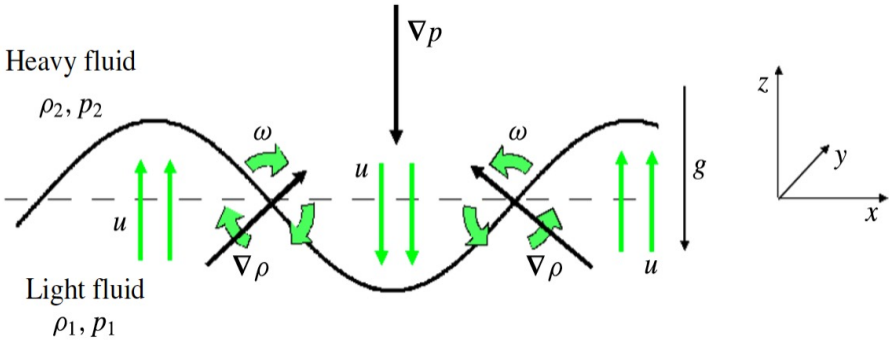

Figure 1.3: Mechanism of RT instability from baroclinic torque. From Roberts & Jacobs (2016), reproduced with permission from Cambridge University Press, Copyright (2015).

and wavenumber k grows exponentially in time as (Chandrasekhar, 2013)

$$\eta(t) = \eta_0 e^{\sqrt{Agk}t}, \tag{1.2}$$

where $A = (\rho_2 - \rho_1)/(\rho_2 + \rho_1)$ is the Atwood number. This equation indicates that the system is unstable only in the case $\rho_2 > \rho_1$.

1.2.3 The Richtmyer-Meshkov instability

The Richtmyer-Meshkov instability (Richtmyer, 1960; Meshkov, 1969) occurs whenever a perturbed interface separating two fluids of different density is impulsively accelerated, e.g., by the passage of a shock wave. This instability is of fundamental importance in shock-induced turbulent mixing applications, such as inertial confinement fusion (Hicks *et al.*, 2012; Meezan *et al.*, 2013) and fuel combustion in supersonic aircrafts (scramjets) (Waitz *et al.*, 1993; Yang *et al.*, 1994*a*). The RM instability may also play a role in diagnostic-ultrasound-induced lung hemorrhage (Patterson & Johnsen, 2018). The driving mechanism of the RM instability is the baroclinic vorticity generated along the interface. As in the RT instability, the misalignment of the pressure gradient, now across the shock, and the density gradient, across the interface, generates a baroclinic torque, leading to perturbation growth. As opposed to the RT instability, however, the RM configuration is always unstable, regardless of the relative position of the heavy and light fluids. Another difference with the RT instability is that, once the shock has traversed the interface, there is no sustained mechanism (like gravity) feeding energy to the system. Using the linear stability theory of Taylor (1950) performed for RT, Richtmyer (1960) replaced the constant acceleration by an impulsive acceleration, i.e., $g = \Delta v \delta(t)$, where Δv is the change in interface velocity due to the shock, and δ is the Dirac delta function. Doing so, Richtmyer (1960) obtained an

impulsive relation for the perturbation growth rate as

$$\dot{\eta}(t) = k\Delta v A \eta_0. \tag{1.3}$$

This equation reveals that the perturbation growth rate is constant, showing that the amplitude grows linearly in time. If the shock propagates from a light fluid to a relatively heavier fluid, the perturbation amplitude only increases, whereas if the shock propagates from a heavy fluid to a lighter fluid, the perturbation first decreases before increasing, a phenomenon called phase inversion (Brouillette, 2002).

1.3 Hydrodynamic instabilities under High-Energy-Density conditions

As described above, hydrodynamic instabilities due to inertia such as KH, RT, and RM are ubiquitous in nature and man-made applications. Of particular interest in this thesis is the role of these instabilities in high-energy-density (HED) systems.

The study of HED physics in the laboratory is a relatively new area of research, and is concerned with the behavior of matter when the energy-density is high. Energy density, i.e., the amount of energy available in a given volume, has the same dimensions as pressure. Drake (2018) defines a system operating under HED conditions when the pressure exceeds approximately 1 Mbar, or 1 million atmospheres. At such high pressures, matter is typically ionized and behaves differently than the conventional solid/fluid states, overlapping with behaviors observed in stars and other astrophysical systems. Plasma effects, radiation transport, electron heat conduction, and magnetic fields are only a few examples of additional physics that one needs to consider when studying such systems. Fig. 1.4 shows a map of different physical and astrophysical systems based on their density and temperature, with the approximate boundary of 1 Mbar (=0.1TPa) separating the realm of HED systems. Gas,

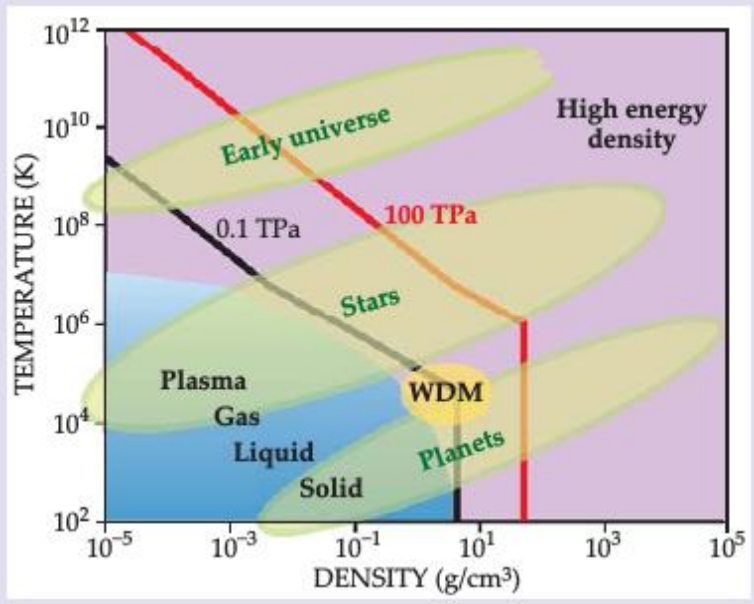

Figure 1.4: Map of different physical systems based on their density and temperature. Reproduced from Drake (2010) with the permission of the American Institute of Physics. DOI: https://doi.org/10.1063/1.3455249.

liquid, and solid states of matter, which are relevant to most applications on Earth, can be sustained until temperatures of about 10,000 K and densities of a few orders of magnitude lower than the density of water. The region where matter is in a plasma state corresponds to systems where the temperature is high enough and the density low enough that matter may be ionized. If electric and magnetic fields, viscous effects, and radiation effects are negligible, the behavior of plasmas is known as "ideal plasmas" and can be described as a simple fluid, i.e., with the Euler equations for a polytropic gas.

With the invention of the laser in the mid-twentieth century, scientists appreciated that the process of energy production occurring in stars by nuclear fusion may be possible to reproduce on Earth, which led to the growing interest in developing technologies able to harness energy from nuclear fusion.

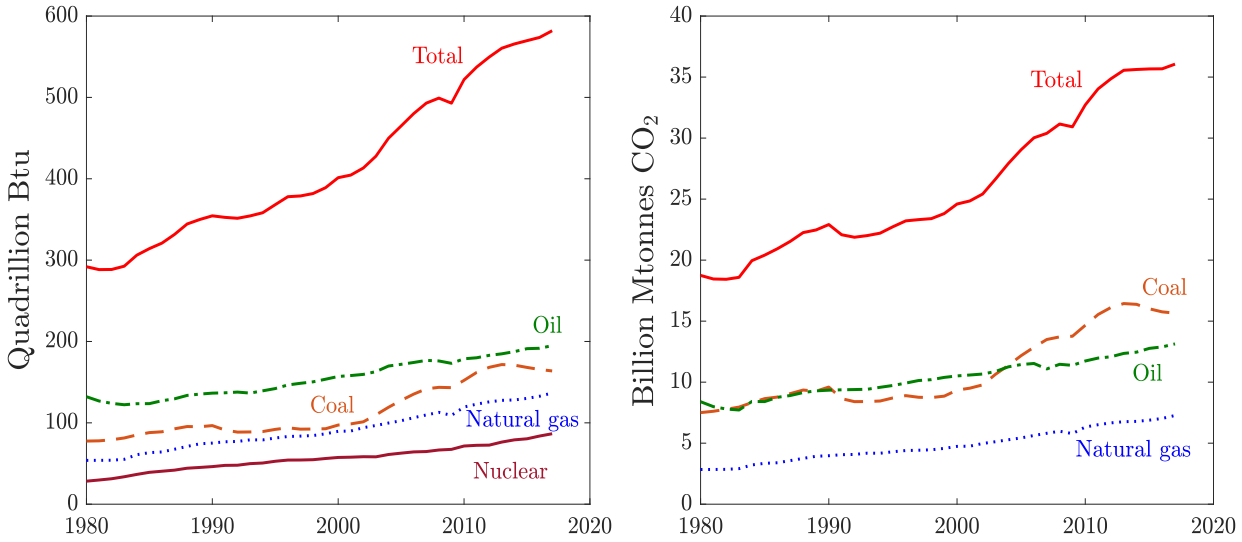

(a) Energy consumption. Btu: British Thermal Unit.

(b) Carbon dioxide emission. Mtonnes: metric ton.

Figure 1.5: History of the world energy consumption and carbon dioxide emission for different sources of primary energy since 1980. Source: U.S. Energy Information Administration (EIA).

1.3.1 Inertial-Confinement Fusion

1.3.1.1 The need for future sources of energy

The production of energy on a global scale is becoming more and more a central topic of concern due to the Earth's continually increasing population, along with the increase of energy consumption per capita. The world total energy consumption has been increasing for the last forty years, with oil still being the dominant source of primary energy fuel, as shown in Fig. 1.5a. Energy consumption can be measured in British Thermal Unit (Btu), which corresponds to the amount of energy needed to raise the temperature of one pound of water by one degree Fahrenheit. Future projections further predict an increase of almost 50% of the world energy by 2050, see the International Energy Outlook 2019 of the U.S Energy Information Administration. Along with the increasing trend of the world energy consumption, carbon dioxide emission into the atmosphere, which is one the main gases contributing to greenhouse pollution, is also increasing, as shown in Fig. 1.5b.

Resources of the Earth's primary energy, such as coal, oil, etc., are limited, and the trends shown in Fig. 1.5 demonstrate the need of new sources of energy for the future of planet Earth. Although not developed to the point of producing energy from fusion power plants, Inertial Confinement Fusion (ICF) has the potential to provide energy without carbon dioxide emission and with reduced amount of nuclear waste, generated by current fission plants.

1.3.1.2 General description and principles

Inertial Confinement Fusion is a technology aiming at producing energy from nuclear fusion, which is the process by which two nuclei are combined together. Fusion between two nuclei occurs when the Coulomb force, the repulsive force existing between protons of the nuclei, is overcome by the nuclear strong force, the attractive force binding neutrons and protons together, resulting in the nuclei to fuse. When the mass of the resulting reaction product is smaller than the mass of the initial nuclei, huge amounts of energy are released, as described by Einstein's relationship between mass and energy, $E = mc^2$. To overcome the Coulomb barrier, i.e., the energy required to overcome the Coulomb repulsion, very high temperatures and densities must be achieved. For instance, most fusion reactions produced in the laboratory today use Deuterium (D) and Tritium (T) elements, known as DT fuel, requiring temperatures of tens of millions of degree Fahrenheit (Betti & Hurricane, 2016). In these conditions, the fuel is a plasma, i.e., an ionized, electrically conducting gas. One of the key elements in achieving thermonuclear fusion, is that these high temperatures and densities be sustained long enough, hence the plasma has to be confined in some way. In stars, for example, confinement is achieved through gravitational compression. On Earth, confinement through inertia is one possibility.

The basic idea behind ICF is to compress the DT fuel to thermonuclear conditions, which can be obtained by imploding a spherical capsule, called a target. Two main approaches are commonly used to drive the target implosion: indirect drive and direct drive. In the United States, the indirect-drive approach is mostly developed at the National Ignition Fa-

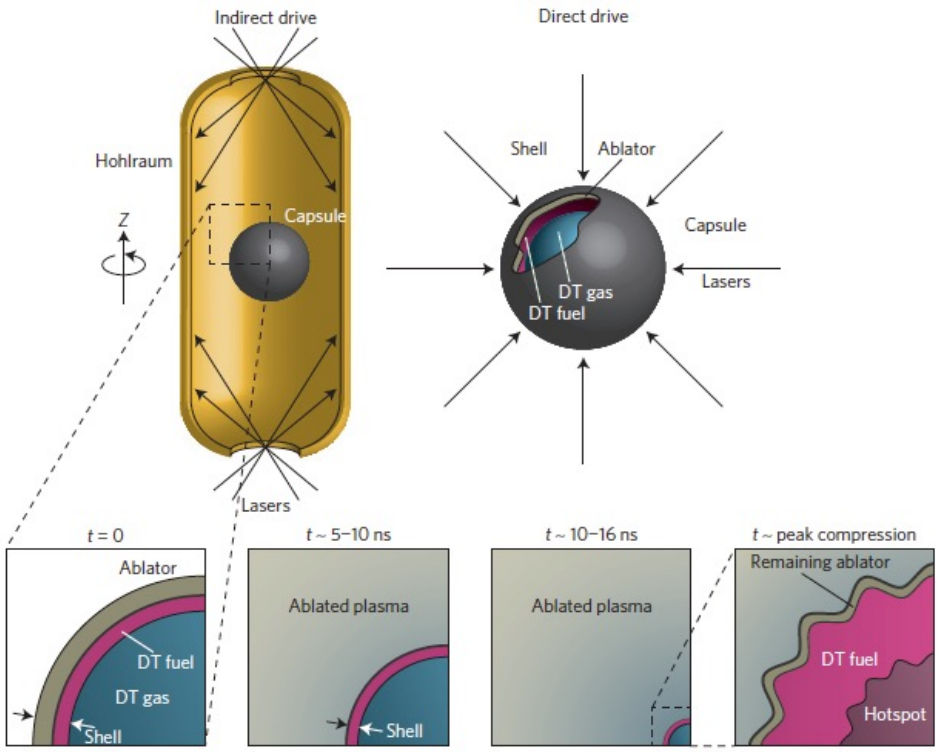

Figure 1.6: Schematic of an ICF capsule implosion in the case of indirect and direct drives. From Betti & Hurricane (2016), reproduced with permission from Springer Nature, Copyright (2016).

cility (NIF) (Campbell & Hogan, 1999; Moses, 2008) at the Lawrence Livermore National Laboratory. The direct-drive approach is mostly developed on the OMEGA Laser Facility (Boehly *et al.*, 1997) at the Laboratory for Laser Energetics and the Nike laser (Obenschain *et al.*, 1996) at the Naval Research Laboratory. In the indirect-drive approach (Lindl, 1995; Lindl *et al.*, 1992), the target is suspended inside a gold vessel, called a hohlraum, in which lasers irradiate the inner walls, producing X-rays, which bathe the capsule, as seen in the left schematic of Fig. 1.6. In the direct-drive approach (Brueckner & Jorna, 1974; McCrory *et al.*, 2008), the capsule is directly irradiated by incident lasers, as seen in the right schematic of Fig. 1.6. Typical target sizes are of the order of the millimeter, and are generally composed of an outer plastic shell (or other low-atomic-number material), called the ablator, encapsulating the DT fuel, made of a layer of DT ice followed by DT gas, as seen in Fig. 1.6. Whether indirect or direct drive, to reach the required high temperatures and densities,

the ablator is heated by absorption of sustained high-intensity-laser energy, from X-rays in the indirect-drive approach, or directly from the lasers in the direct-drive approach. This intense irradiation of the capsule produces high-enough pressures that material is ablated away from the capsule surface, flowing outward. As a consequence of Newton's third law, the remaining fuel is accelerated and compressed inward, behaving as a "spherical rocket". As the fuel is compressed, it eventually reaches a stagnation point at the center of the target, where kinetic energy is converted into internal energy, leading to a hot, dense core, called the hot-spot, where fusion reactions take place and may ignite the fuel.

1.3.1.3 Role of hydrodynamic instabilities and transition to turbulence

One of the key challenges during capsule implosion is the growth of hydrodynamic instabilities, which are responsible for degrading the conditions necessary to achieve ignition. In the early time of the implosion (Fig. 1.6a.), laser irradiation of the outer shell of the capsule produces a pressure pulse, which launches a shock wave propagating into the target. Any modulations on the ablator material, for example originating from target fabrication, will therefore grow due to the RM instability. In the acceleration phase (Fig. 1.6b.), these perturbations grow exponentially due to the acceleration of the relatively high-density ice layer into the relatively low-density DT gas, leading to the development of RT instability. Subsequently, the initial shock wave moving ahead of the accelerating shell, reflects from the target center and interacts back with the converging shell, decelerating it (Fig. 1.6c.). Multiple shock reflections can occur during the implosion, such that the combination of the shell deceleration and its interaction with the reflected shocks seeds further growth for the RT and RM instabilities. The RT and RM instabilities play a critical role into the implosion dynamics of ICF capsules, as they initiate mixing between the hot fuel and the relatively cooler outer shell, thus reducing the temperature necessary for ignition in the hot-spot. Another challenge in ICF is to be able to achieve the most efficient compression, which requires to implode the target as symmetric as possible. This constraint of a spherical implosion is

challenged by the presence of asymmetries, e.g., a non-uniform pressure distribution originating from a non-uniform laser irradiation. Such asymmetries in the laser-energy input, called asymmetric drive, results in asymmetrical implosions, which reduces the amount of fuel compression, ultimately reducing the required temperature at the core. Furthermore, asymmetric drives could launch non-spherical shocks, i.e., the normal direction to the shock is misaligned with respect to the radial direction, introducing elements of shear in addition to the radial momentum propagation. In this case, we say that the shock is oblique with respect to streamwise direction of propagation.

1.4 Previous work

In this section, we review some of the past work most relevant to this thesis on the RM instability achieved under classical fluid conditions and high-energy-density conditions. For an exhaustive review of past studies of RT and RM instabilities, the reader is referred to Zhou (2017*a*,*b*).

1.4.1 Laboratory experiments

The RM instability was first investigated experimentally by Meshkov (1969), who confirmed the earlier theoretical result predicted by Richtmyer (1960), i.e., the instability grows at a constant growth rate. Since then, a considerable amount of research has been dedicated to studying the RM instability. Great progress has been made in terms of new techniques to produce shocks (or impulsive accelerations), interfaces, as well as diagnostics to observe the instability.

1.4.1.1 Classical-fluids experiments

A common way of producing shock waves is by using shock tubes, in which a high pressure source is created, e.g., by a driving piston or puncturing a diaphragm. The resulting shock

wave then travels to meet a perturbed interface separating two different gases, and where the instability develops. One of the main difficulties when using gases is to create, and maintain, a well-defined sharp interface, due to their relatively high mass diffusion coefficients compared to liquids. The strength of the shock, measured by the shock Mach number, is typically in the range $1 \lesssim M_s \lesssim 3$. Different methods are used to create the interface. Early experiments in vertical shock tubes have used a solid barrier to separate two different gases, typically a horizontally sliding plate separating a layer of air above the plate from a test gas below the plate, e.g., helium or sulfur hexafluoride (SF_6) (Brouillette & Sturtevant, 1993, 1994; Bonazza & Sturtevant, 1996). Immediately before firing the shock, the plate is removed, which creates a wake behind the plate, serving as perturbation. This technique generates relatively diffuse thick interfaces ($\approx$ 1cm), which reduces the growth rate, and wall vortices created from shock boundary-layer interaction have to be carefully distinguished from the interface during the diagnostics. Instead of a solid barrier, other studies have used thin membranes to separate gases, which can be pre-shaped to form a sinusoidal perturbation (Aleshin *et al.*, 1988; Vasilenko *et al.*, 1992; Benjamin, 1988; Andronov *et al.*, 1976). One of the main shortcomings of this technique is that fragments of the broken membrane due to the passage of the shock interfere with the evolution of the interface, and hinder the use of advanced visualization techniques, such as Particle-Image Velocimetry (PIV) and Planar Laser-Induced Fluorescence (PLIF). Other studies were successful in creating relatively sharp interfaces by using liquids instead of gases (Benjamin & Fritz, 1987; Castilla *et al.*, 1993). However, the evolution of the interface in these experiments could only be visualized in the early development of the instability, due to the effect of gravity, which tends to stabilize the flow. To avoid this effect of gravity, Jacobs & Sheeley (1996) designed a setup in which the tank containing the liquids bounces off a spring, making the evolution of the instability essentially in free-fall. The initial perturbation along the interface was introduced by gently oscillating the tube in the lateral direction. Their experiments showed good agreement with the linear theory and collapse of the data at late time when scaled with the initial circulation.

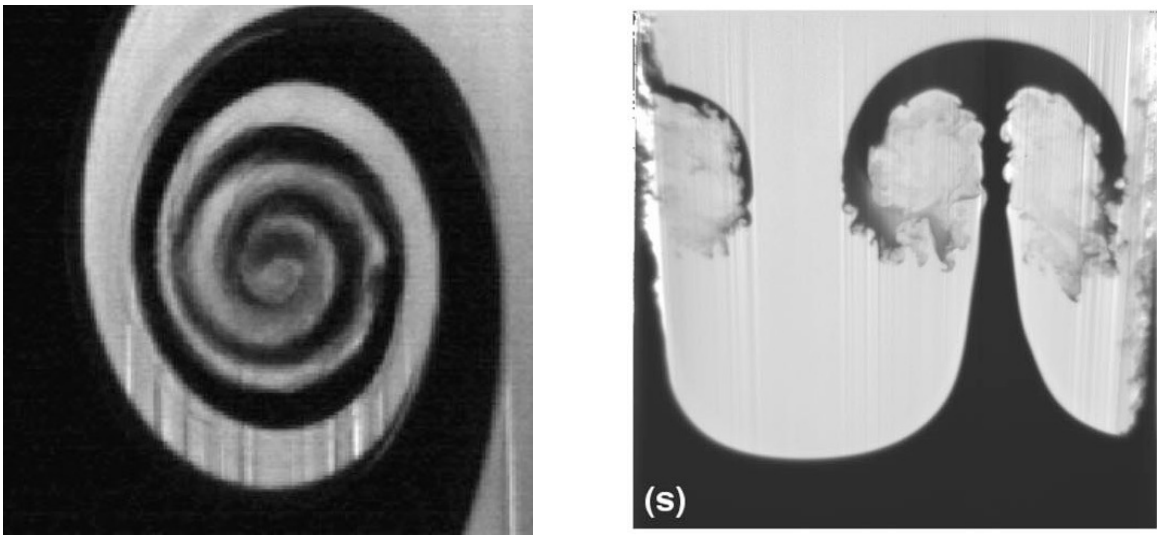

(a) Secondary instability (b) Roll-up disintegration

Figure 1.7: Examples of (a) the growth of secondary instabilities and (b) their consequence on the roll-ups behavior. (a) From Niederhaus & Jacobs (2003), reproduced with permission from Cambridge University Press, Copyright (2003), and (b) from Jacobs & Krivets (2005), reproduced with permission from AIP Publishing, Copyright (2005).

As part of this study, they developed a point-vortex model.

Although the early-time, linear regime of the perturbation growth is fairly well understood, the late-time, non-linear regime is less known. Experimental difficulties associated with the use of membranes were alleviated by Jones & Jacobs (1997), who designed a membrane-less technique for gas-gas interfaces in shock tubes. The insertion of fog in the tube allowed them to visualize the large mushroom-like structures far into the non-linear regime, but were unable to observe the smaller-scale structures developing inside the roll-ups. Using PLIF, Collins & Jacobs (2002) and Niederhaus & Jacobs (2003) were able to obtain detailed images of the roll-up morphologies, and observed the growth of small-scale secondary instabilities along the spirals of the roll-ups, as illustrated in Fig. 1.7a. These unstable structures first appear as some form of waviness, which subsequently grow into a KH-type instability, ultimately breaking down and destroying the vortex cores, leading to a fully turbulent region, as illustrated in Fig. 1.7b. Other studies also observed similar secondary instabilities in shock-cylinder interactions (Jacobs, 1993; Vorobieff *et al.*, 2003).

The flow transition to turbulence in RT- and RM-driven mixing environments is an active topic of research, and the quest for self-similarity is one of the most sought-after questions in the community.

1.4.1.2 High-energy-density experiments

Although classical-fluids experiments are extremely valuable in the understanding of hydrodynamic instabilities, they are typically limited to low-Mach numbers ($M_s \lesssim 3$) and face challenges in producing sharp interfaces, introducing uncertainties in the initial conditions. In contrast, HED experiments can produce much stronger shock waves ($M_s \gtrsim 20$), which is more relevant to ICF. Because the pre-shock materials are in the solid phase, well-defined, sharp interfaces can be accurately manufactured and easily reproduced. The laser-generated pressure can reach such extreme values ($\gtrsim$ 300Mbar) (Nora *et al.*, 2015), that the post-shock materials are in the plasma state. One of the downsides, however, is that HED experiments diagnostics are typically limited to x-ray imaging, and do not produce high-resolution images. HED experiments are generally conducted with high-intensity lasers available in facilities such as the NIF and OMEGA Laser Facility.

Early RM experiments under HED conditions mainly aimed at reducing discrepancies between theory and experiments that classical-fluids studies had revealed (Dimonte *et al.*, 1996; Dimonte & Remington, 1993). Validation of hydrodynamics codes was also important, further motivating the need for HED experimental data (Holmes *et al.*, 1999). The ability to create laser-produced plasma environments in the laboratory also motivated astrophysically relevant experiments, where conditions similar to those of supernovae formation could be achieved (Remington *et al.*, 1997; Kuranz *et al.*, 2011, 2018, 2005). Recently, experiments of single mode perturbation RM instability produced relatively clear images of the perturbation growth well into the non-linear regime (Nagel *et al.*, 2017). When more than one mode characterizes the initial shape of the perturbation, the perturbation growth into the non-linear regime is associated with mode interaction, which was studied in the case of two initial

modes (Di Stefano *et al.*, 2015*b*) and for a wide band of wavenumbers (Malamud *et al.*, 2013*a*; Di Stefano *et al.*, 2015*a*, 2017).

The first successful design of HED experiments for observation of the KH instability was developed by Hurricane (2008), although the first measurements of perturbation growth was performed by Harding *et al.* (2009). Beyond the early growth of the perturbation, the development of KH roll-ups, i.e., large co-rotating vortices, may lead to turbulent mixing (Smalyuk *et al.*, 2012; Doss *et al.*, 2013). The design of the shock/shear experiments on the NIF, where two counter-propagating shocks are used to induce a shear flow at an interface, allowed the instability to be observed at later times (Doss *et al.*, 2015), and to characterize the transition to turbulence with initial conditions (Flippo *et al.*, 2018). The KH instability was also observed for compressible flows (Wan *et al.*, 2015, 2017).

1.4.2 Numerical simulations and models

Because of the development of ever smaller length scales in the late-time evolution of the KH, RT, and RM instabilities, it is difficult to obtain precise measurements of the flow variables for all stages of perturbation growth, i.e., from linear growth to fully turbulent. Uncertainties in the initial conditions in classical-fluids experiments, and the constraint of sustaining a long enough laser drive in HED experiments make predictions challenging. The temporal and spatial resolution of the diagnostics is limited, making the flow turbulence challenging to study; numerical simulations and turbulence models may alleviate this issue. Furthermore, experiments typically do not generate large amounts of data (especially HED experiments). Developing theoretical models and performing numerical simulations may provide a way to complement experiments, and ultimately predict the late-time behavior of the flow.

Besides the linear impulsive model derived by Richtmyer (1960), other studies have developed linear models based on the linearization of the compressible Euler equations (Yang *et al.*, 1994*b*; Wouchuk & Nishihara, 1996, 1997). These models allowed the early growth of

the RM instability to be determined for more general cases than the impulsive model considered, e.g., reflected rarefaction, arbitrary incident shock strengths, and gases with different ratio of specific heats. Early compressibility and bulk vorticity effects were also considered. The linear phase of the RM instability being short-lived, these models fail to describe the growth when the size of the perturbation becomes of the order of the wavelength. Multiple models have therefore been developed to describe the non-linear regime.

The first simple model based on potential flow theory was developed by Layzer (1955), who derived an ordinary differential equation for the constant asymptotic bubble velocity for the RT instability. Hecht *et al.* (1994) used the same approach for the RM instability and showed that the asymptotic bubble velocity behaves as λt^{-1} (where λ is the perturbation wavelength). The approach of using potential flow theory was also used to derived buoyancy-drag models (Oron *et al.*, 2001). The basic idea is to express the bubble velocity as a balance between the buoyancy force and the kinematic drag, originating from the bubble of light fluid rising into a relatively heavier fluid. These Layzer-type models, however, are generally valid only in the asymptotic stage of perturbation growth and for infinite density ratio, i.e., $A = 1$. Layzer-type models were extended to arbitrary Atwood number by Goncharov (2002) for RT, and Sohn (2003) for RT and RM. Jacobs & Sheeley (1996) modeled the late-time RM instability for small Atwood number by using a point-vortex model, which assumes that the flow evolves into a row of point vortices, allowing them to provide a lower bound for the perturbation amplitude. One technique to obtain the perturbation growth analytically in the non-linear regime of the RM instability is to expand the potential flow equations in terms of power series of the initial perturbation amplitude. By matching the solution obtained from the compressible linear theory to the incompressible non-linear solution obtained by Padé approximations, the perturbation growth may be determined from the early-time to the late-time regime (Zhang & Sohn, 1996, 1997*a*,*b*).

Although theoretical models are valuable due to the analytical formulae they provide, they are limited to a specific range of parameters and quantities of interest, as well as initial

conditions. High-fidelity numerical simulations are therefore inevitable. In the linear regime of the RM instability, experiments, numerical simulations, and theories agree relatively well with each other. However, the behavior of the instability in the non-linear regime is still controversial and discrepancies still remain. The work of Holmes *et al.* (1999) provides comparisons between experiments, numerical simulations performed with three different codes, and analytical theories. Although they found good agreement with linear theories at early times, non-linear models struggle to predict the late-time growth rate. Similar discrepancies have been observed by Long *et al.* (2009), who found that the overall late-time growth rate behaves as $t^{-0.54}$, and that the spike velocity shows a $v_s \sim t^{-0.38}$ dependence, compared to the $\sim t^{-1}$ dependence predicted by nonlinear models. Dimonte & Ramaprabhu (2010) have also found disagreements between existing nonlinear models and their simulations but for Atwood numbers and initial amplitudes relevant to ICF conditions ($A \gtrsim 0.9$ and $k\eta_0 \gtrsim 1$). For moderate Atwood numbers and initial amplitudes, better agreement is achieved. One of the aspects of the RM instability that researchers have focus their attention on is the so-called "reshock" phenomenon. Reshock refers to when a second shock, originating from the reflection at a boundary for example, interacts with the perturbation, depositing additional baroclinic vorticity and enhancing mixing. The interaction of the second shock with the interface may also produce a rarefaction, which itself reflects off the boundary and interacts again with the interface. Many reflections can occur and are relevant to ICF capsule implosions, as a shock may be reflected from the point of convergence, interacting back with the converging shell. Using shock-capturing weighted essentially nonoscillatory (WENO) scheme, Latini *et al.* (2007*a*,*b*) were able to reproduce some of the observations of the experiments of Collins & Jacobs (2002), and obtained good agreement between linear/non-linear models and their simulations before reshock. Schilling *et al.* (2007) extended the simulation time of Latini *et al.* (2007*b*) to after reshock, and qualitatively described the reshock process by providing the evolution of the density and vorticity fields. They showed that the positive and negative circulation magnitudes are the same before and after reshock until the arrival of

the reflected rarefaction on the interface, introducing flow asymmetry and different evolution of positive and negative circulation. They further quantify the evolution of the mixing layer after reshock by considering energy spectra and turbulence statistics to show that reshock amplifies fluctuations in all fields. Movahed & Johnsen (2013) also considered the WENO scheme for the RM instability, but solving the Navier-Stokes equations. They developed a new approach in which a discontinuity sensor is introduced to differentiate between smooth and discontinuous regions, preventing spurious oscillations at the interface. Because the process of reshock includes a wide range of turbulent scales, methods such as Large-Eddy Simulations (LES) have also been used to estimate statistics of the unresolved scales of the turbulent mixing zone (Hill *et al.*, 2006; Lombardini *et al.*, 2011). When more than one wavenumber characterize the initial perturbation, direct simulations of the compressible Euler equations were performed by Leinov *et al.* (2009) in the case of a random multimode perturbation, and Cohen *et al.* (2002) for a two-scale initial perturbation. Finally, using the Discontinuous Galerkin method (Henry de Frahan *et al.*, 2015*b*), Henry de Frahan *et al.* (2015*a*) investigated the RM instability for successive material interfaces, a configuration relevant to ICF.

1.5 Vorticity paradigm and motivation for a vorticity-based approach

1.5.1 The vorticity paradigm

The late-time, non-linear evolution of RT-, RM-, and KH-driven flows is associated with the formation of large vortex structures (of the order of the perturbation wavelength), in which turbulent mixing may occur. By "vortex structures" we refer to the interface rolling over itself, forming roll-ups similar to those shown in Fig. 1.7. Since much of the vorticity in the flow is localized at the interface, a connection between the motion of the interface

and the vorticity dynamics exists. For example, in their study of the RM instability, Jacobs & Sheeley (1996) recognized that the late-time interface dynamics is related to the initial vorticity generated along the interface. Knowing how the vorticity is initially generated and distributed along the interface is therefore critical in the understanding of the subsequent evolution of the flow. For RT and RM instabilities, the source of this initial vorticity is baroclinic, i.e., caused by the misalignment between a density gradient and a pressure gradient. For RM, the density gradient is initially located at the interface, and the pressure gradient at the shock location (or more generally pressure wave). For RT, the density gradient is also initially located at the interface, but the pressure gradient comes from the acceleration due to gravity (or more generally fluid acceleration). For the KH instability, the mechanism of vorticity production is kinematic (velocity gradient across the interface), although baroclinic vorticity may also be generated if there is a density mismatch at the interface.

Zabusky (1999) and Hawley & Zabusky (1989) were the first to qualitatively describe the evolution of the RM instability in terms of vorticity dynamics, although similar descriptions for shock-bubble interactions were previously made (Picone & Boris, 1988). Zabusky (1999) introduced a vorticity paradigm by decomposing the perturbation evolution in four different phases: the vorticity deposition phase, the linear and early non-linear phase until the interface becomes multivalued, the intermediate non-linear phase where the roll-ups form, and the late-time phase leading to mixing and turbulence. The vorticity-deposition phase is crucial to understand, as it dictates the subsequent flow evolution. During the vorticity deposition phase, the shock deposits baroclinic vorticity along the interface until the shock leaves the interface. As the incident shock interacts with the interface, a transmitted shock and a reflected wave (shock or rarefaction) propagate into each media. In Chapter 2, we will give more details on shock refraction. When the speed of the transmitted shock is larger (smaller) than the speed of the incident shock, the refraction is known as "slow-fast" ("fast-slow"). The amount of deposited vorticity therefore depends on the size of the perturbation, the media on each side of the interface, and the strength of the incident shock.

Using shock-polar analysis, Samtaney & Zabusky (1994) obtained an analytical expression for the circulation deposited on an inclined interface in the fast-slow case, while Samtaney *et al.* (1998) obtained the counterpart expression for the slow-fast case (see Chapter 2).

1.5.2 Vortex-sheet modeling of vorticity dynamics

After the vorticity-deposition phase, the interface is left to evolve according to two elements: the amount of vorticity that was deposited, and the changes in the vorticity distribution along the interface over time. Because of the large number of degrees of freedom in numerical simulations, it is challenging to obtain these elements and isolate the role of vorticity dynamics in the evolution of the interface from numerical simulations. The latter may provide the knowledge of the vorticity field, but their Eulerian-based framework makes it challenging to understand the vorticity contributions to the interface evolution. Even if infinite resolution was available, numerical simulations do not allow for a consistent way of interpreting the evolution of the vorticity distribution along the interface. Consequently, an approach in which vorticity is directly represented in the reference frame of the interface may be more useful in understanding the vorticity-dominated dynamics of the interface. A unique approach specifically designed for this purpose is to model the interfacial vorticity distribution as a vortex-sheet strength, defined as the jump in the tangential velocity across the interface (see Chapter 2). Doing so allows the equations of motion (the Euler equations in our case) to be reduced to a weaker form, allowing both the motion of the interface and its corresponding vorticity distribution to be tracked over time. The uniqueness of the vortex-sheet model lies in the fact that the reduced-set of the governing equations describe the evolution of the vorticity kinematics and baroclinic vorticity (if surface tension is neglected) of a vortex sheet.

One of the main drawbacks that early vortex-sheet models faced was the formation of singularities, e.g., when simulating the KH instability, due to the fact that the vortex sheet stops to be analytic past a critical time, leading to infinite sheet curvature (Moore, 1979, 1985; Krasny, 1986*b*; Meiron *et al.*, 1982*a*). Similar singularities formation was also found

when simulating the RT instability (Baker *et al.*, 1993) and the RM instability (Matsuoka & Nishihara, 2006*c*). Some investigators have proposed methods allowing simulation of vortex sheets past the time of singularity, for example by using higher-order accurate methods (Higdon & Pozrikidis, 1985; Baker, 1980), or by applying some kind of smoothing (Krasny, 1986*a*; Chorin & Bernard, 1973). The method of kernel smoothing introduced by Krasny (1986*a*) (see Chapter 2) is now widely used in vortex-sheet computations. While the vortex-sheet model has been used to study the RT instability (Tryggvason, 1988; Baker *et al.*, 1980; Kerr, 1988; Zufiria, 1988; Sohn, 2011) and the KH instability (Krasny, 1986*a*,*b*; Meiron *et al.*, 1982*b*; Sohn *et al.*, 2010), only a few studies considered the RM instability. The first study to have applied a vortex-sheet model to the RM instability was by Matsuoka *et al.* (2003), who were able to observe the early stage of roll-up formation. Sohn (2004) performed simulations until later times and for different values of the density ratio. Other studies have also used the vortex-sheet model for the RM instability in convergent, cylindrical geometries (Matsuoka & Nishihara, 2006*a*,*b*), and the recent work of Matsuoka & Nishihara (2020) investigated the interaction of bulk vortices with vortex sheets. In the HED community, the vortex-sheet model has yet to be used for KH, RT, and RM instabilities, with the exception of the recent work by Rasmus *et al.* (2019), which did not include a density mismatch at the interface.

One of the most difficult tasks when implementing vortex-sheet computations is the determination of the initial conditions. For example, in the case of the RM instability, an appropriate evaluation of the sheet-strength distribution and interface morphology after the passage of the shock over the interface is required. If the perturbations are small enough ($ka \ll 1$), the sheet strength may be evaluated from the velocity potentials on either side of the interface (Jacobs & Sheeley, 1996; Sohn, 2004), and the interface shape may be assumed to be unchanged. For analyses focused more on the improvement of the numerics, one may choose a fairly arbitrary sheet-strength distribution, e.g., a sinusoidal distribution. However, these initialization techniques do not account for changes in the interface morphology, and may become invalid when applied to more general problems, e.g., arbitrary perturbations,

arbitrary incident wave, non-ideal equations of state. One attempt to initialize vortex-sheet computations under HED-relevant conditions was made by Rasmus *et al.* (2019), but provided a kinematics-only description of the interface. Furthermore, there are no techniques to date available allowing the determination of the sheet-strength distribution for finite amplitude perturbations.

1.6 Thesis overview and contributions

As illustrated in this chapter, flows induced by the growth of RT, RM, and KH instabilities are complex, due to their multi-physics character and the wide range of spatial and temporal scales they involve. These flows are unsteady, compressible, involve sharp gradients (shocks, interfaces), and may evolve to a state of turbulence. Under HED conditions, this picture is even further complicated by additional complex physics, e.g., radiation, magnetic fields, and non-ideal gas equations of state.

The research undertaken in the present thesis is motivated by the realization that the late-time behavior of these interfacial instabilities is connected to the vorticity generated along the interface initially. The overarching hypothesis guiding this work is that perturbation growth can be described by the vorticity dynamics of the interface. Because experiments and numerical simulations include all field variables in the entire domain of interest, they cannot isolate the vorticity-dominated dynamics of the flow. The objective of this work is to understand the role of vorticity dynamics in:

- The evolution of perturbed interfaces driven by combined effects of KH, RT, and RM, arising simultaneously, Chapter 3. Our vortex-sheet model allows us to readily control the relative importance between KH and RM by an appropriate choice of the initial vorticity distribution, and to account for time-dependent acceleration related to RT.

- The late non-linear regime of the RM instability, Chapter 4. We first explore the origin of opposite-sign vorticity generation, and its connection to roll-up behavior in the late

stage of RM instability. We then investigate vorticity deposition on finite-amplitude perturbation, and cast the results in the context of reshock environments, Appendix C.

The main contributions of the work reported in this thesis to the field of interfacial hydrodynamic instabilities are:

- Vortex-sheet simulations of combined KH, RM, and RT instabilities under HED conditions
  - Determination of dominant mechanism (RM vs. KH) based on the evolution of the vorticity distribution along the interface
  - Scaling of perturbation growth with initial vorticity, demonstrating the early dominance of the impulsive acceleration, and the amplification of shear at later times
  - Extension of the vortex-sheet model to time-dependent acceleration
- Identification of vorticity-dominated mechanisms responsible for generation of opposite-sign vorticity
  - Connection between vortex-core oscillatory behavior and sheet-strength oscillations
  - Discovery of a time scaling of perturbation evolution with initial vorticity
  - Determination of power-law behavior for opposite-sign circulation

CHAPTER 2

Vortex-Sheet Model and Numerical Methods

In this chapter, we review some of the concepts necessary to understand the description of shock-driven interfaces in terms of vorticity dynamics. The governing equations of the vortex-sheet model are presented, along with their numerical discretization. A point-insertion procedure is also presented, along with the determination of the initial conditions.

2.1 Description of the physical problem

In the context of RT, RM, and KH flows, the velocity field typically exhibits sharp gradients across a thin layer separating two different fluids (the interface). An important feature of these type of flows is that vorticity is localized to only well-defined regions (typically at the interface), such that the flow away from the interface can be considered irrotational. Furthermore, the thickness of the interface is typically small compared to its wavelength (approximately 10% of the wavelength (Jones & Jacobs, 1997; Collins & Jacobs, 2002; Latini *et al.*, 2007*b*)), such that effects due to a diffuse interface can be neglected. In this context, it is not unreasonable to assume that the interface is sharp, i.e., a zero-thickness layer, and that the density and velocity are discontinuous across the interface. The density gradient at the interface is therefore infinite, and the vorticity field, $\boldsymbol{\omega}(\boldsymbol{x}, t)$, is zero everywhere except at the interface, where it is also infinite. Such a singular vorticity distribution is known as

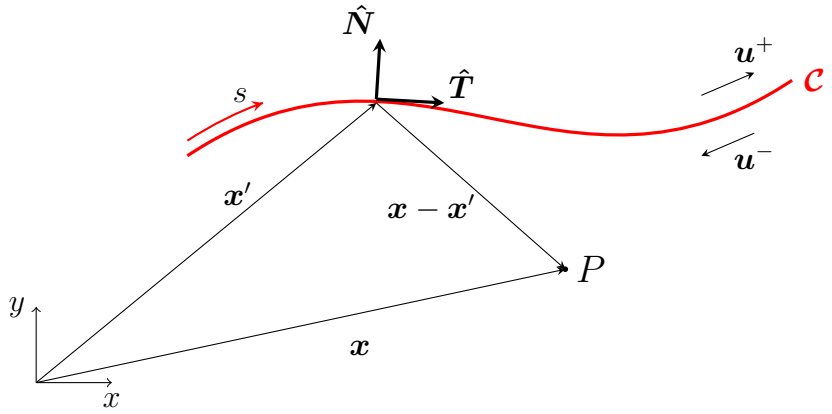

Figure 2.1: Schematic of a two-dimensional vortex sheet.

a vortex sheet, defined, in two dimensions, as

$$\omega(\boldsymbol{x},t) = \gamma(\boldsymbol{x},t)\delta(\boldsymbol{x}), \tag{2.1}$$

where γ is the scalar vortex-sheet strength, and $\delta(\boldsymbol{x})$ is the Dirac delta function in the normal direction to the sheet, n, as depicted in Fig. 2.1. The sheet strength is defined as the jump in the tangential velocity across the sheet as

$$\gamma = (\boldsymbol{u}^- - \boldsymbol{u}^+)\cdot\hat{\boldsymbol{T}} = \Delta\boldsymbol{u}\cdot\hat{\boldsymbol{T}}, \tag{2.2}$$

where $\Delta\boldsymbol{u} \equiv \boldsymbol{u}^- - \boldsymbol{u}^+$ and $\hat{\boldsymbol{T}}$ is the tangential vector to the sheet. Only the tangential component of the velocity across the sheet is discontinuous, as conservation of mass requires that the normal component be continuous. Therefore, a vortex sheet is a zero-thickness surface (or line in two dimensions) where the vorticity magnitude is infinite, and across which the velocity tangential component is discontinuous. In such configurations, it is not appropriate to use the governing equations of the flow in their strong form. A weak form, in which discontinuities are handled more appropriately, is therefore necessary. For a discussion on the existence of weak solutions to the governing equations, we refer the reader to Majda & Bertozzi (2001) and Cottet *et al.* (2000). In Sec. 2.2.3, I show that the velocity induced

by a vorticity distribution (such as a vortex sheet for example) can be expressed in a simple form if the fluids on each side of the sheet are assumed to be incompressible.

Next, I present the equations governing the flow evolution, i.e., the Navier-Stokes equations, and the corresponding vorticity equation. Under appropriate assumptions, I show how an alternative formulation to the vorticity equation can be obtained when considering vortex sheets.

2.2 Vorticity formulation of the equations of motion

2.2.1 The Navier-Stokes equations

The continuum physical model describing the evolution of Newtonian fluids motion is based on the Navier-Stokes equations, which describe the conservation of mass, momentum, and energy. For the purposes of this work, which mainly focuses on the RM instability, the fluids can be considered incompressible once all pressure waves have propagated away from the interface. In Sec. 2.2.3, I show how the incompressibility condition allows the velocity vector to be written in terms of vorticity (i.e., the Biot-Savart law). The Navier-Stokes equations for incompressible flows can be written as

$$\begin{aligned} &\nabla \cdot \boldsymbol{u} = 0 \\ &\frac{\partial \boldsymbol{u}}{\partial t} + (\boldsymbol{u} \cdot \nabla)\, \boldsymbol{u} = \boldsymbol{g}(t) - \frac{1}{\rho}\nabla p + \nu \nabla^2 \boldsymbol{u} \end{aligned} \tag{2.3}$$

where ρ and $\boldsymbol{u}$ are the fluid density and velocity, respectively, $\boldsymbol{g}(t)$ is a general reference frame acceleration that may be time-dependent, p the pressure, and ν the kinematic viscosity. In the context of RT, RM, and KH instabilities, it is reasonable to assume that the fluids have constant temperature, such that heat transfer through conduction can be neglected. If no additional heat sources are present, such as combustion, radiation, or electromagnetic forces, and that viscous effects can be neglected, only the conservation of mass and momentum are

relevant.

2.2.2 Mechanism of baroclinic vorticity generation

To better understand the vorticity evolution along the interface, it is convenient to express the equations of motion in terms of vorticity. In addition, for flows with singular vorticity distributions (as in RT, RM, and KH), a vorticity formulation allows the equations of motion to be solved only in these regions, greatly reducing the computational cost. By taking the curl of the momentum equation in Eq. 2.3, the vorticity equation is given by (where the compressible term is included to be more general)

$$\frac{\partial \boldsymbol{\omega}}{\partial t} + \underbrace{(\boldsymbol{u}\cdot\nabla)\,\boldsymbol{\omega}}_{\text{advection}} - \underbrace{(\boldsymbol{\omega}\cdot\nabla)\,\boldsymbol{u}}_{\text{vortex stretching}} + \underbrace{\boldsymbol{\omega}\,(\nabla\cdot\boldsymbol{u})}_{\text{compressibility}} = \underbrace{\frac{\nabla\rho\times\nabla p}{\rho^2} - \frac{\nabla\rho\times\boldsymbol{g}}{\rho}}_{\text{baroclinic}} + \underbrace{\nu\nabla^2\boldsymbol{\omega}}_{\text{diffusion}}, \tag{2.4}$$

where $\boldsymbol{\omega} = \nabla\times\boldsymbol{u}$ is the vorticity vector. The second, third, and fourth terms on the left-hand side represent the advection of vorticity with the flow velocity, vorticity production due to the stretching of vortex tubes, and vorticity production due to compressibility, respectively. In two dimensions, the vortex-stretching term vanishes. The first term on the right-hand side represents the production of vorticity through baroclinic torque, while the last term represents the diffusion of vorticity through viscosity. By an appropriate choice of characteristic scales, we can obtain the dimensionless form of the momentum equation as (where the tilde denotes the dimensionless variables),

$$\frac{\partial\tilde{\boldsymbol{u}}}{\partial\tilde{t}} + (\tilde{\boldsymbol{u}}\cdot\nabla)\,\tilde{\boldsymbol{u}} = \frac{1}{\mathrm{Fr}^2}\tilde{\boldsymbol{g}} - \frac{\mathcal{P}}{\rho_0 V^2}\nabla\tilde{p} + \frac{1}{\mathrm{Re}}\nabla^2\tilde{\boldsymbol{u}}, \tag{2.5}$$

and the corresponding vorticity equation

$$\frac{\partial\tilde{\boldsymbol{\omega}}}{\partial\tilde{t}} + (\tilde{\boldsymbol{u}}\cdot\nabla)\,\tilde{\boldsymbol{\omega}} - (\tilde{\boldsymbol{\omega}}\cdot\nabla)\,\tilde{\boldsymbol{u}} + \tilde{\boldsymbol{\omega}}\,(\nabla\cdot\tilde{\boldsymbol{u}}) = \frac{\mathcal{P}}{\rho_0 V^2}\frac{\nabla\tilde{\rho}\times\nabla\tilde{p}}{\tilde{\rho}^2} - \frac{1}{\mathrm{Fr}^2}\frac{\nabla\tilde{\rho}\times\tilde{\boldsymbol{g}}}{\tilde{\rho}} + \frac{1}{\mathrm{Re}}\nabla^2\tilde{\omega}. \tag{2.6}$$

Two important dimensionless numbers appear

$$\begin{aligned} &\text{Reynolds number:} \quad \mathrm{Re} = \frac{VL}{\nu} \\ &\text{Froude number:} \quad \mathrm{Fr} = \frac{V}{\sqrt{gL}} \end{aligned} \tag{2.7}$$

where L, V, and $\mathcal{P}$ are characteristic length, velocity, and pressure scales, respectively. We see that if the Reynolds number is large ($\mathrm{Re} \gg 1$), and the flow considered incompressible and two-dimensional, the vorticity equation simplifies to

$$\frac{\partial \tilde{\boldsymbol{\omega}}}{\partial \tilde{t}} + (\tilde{\boldsymbol{u}} \cdot \nabla)\, \tilde{\boldsymbol{\omega}} = \frac{\mathcal{P}}{\rho_0 V^2} \frac{\nabla \tilde{\rho} \times \nabla \tilde{p}}{\tilde{\rho}^2} - \frac{1}{\mathrm{Fr}^2} \frac{\nabla \tilde{\rho} \times \tilde{\boldsymbol{g}}}{\tilde{\rho}}. \tag{2.8}$$

Eq. 2.8 is the main equation driving the discussion of the present work, and shows that for an RT-, RM-, and KH-type flow, the only source of vorticity is baroclinic. If the Froude number is also large ($\mathrm{Fr} \gg 1$), neglecting the effect of gravity is a reasonable assumption.

2.2.3 Vorticity-velocity formulation

Although the dependent variable in Eq. 2.8 is the vorticity, the equation still depends on the velocity. To simplify the amount of algebra, the following discussion is restricted to two-dimensional flows, though the final result is similar in three dimensions. From the incompressibility condition, the components of the velocity $\boldsymbol{u}$ can be expressed in terms of the scalar stream function ψ as

$$u = \frac{\partial \psi}{\partial y}, \qquad v = -\frac{\partial \psi}{\partial x}, \tag{2.9}$$

which leads to a Poisson equation for the stream function forced by the vorticity in the $z-$direction

$$\omega = -\nabla^2 \psi. \tag{2.10}$$

A solution to this equation is given by the convolution of a Green's function $\mathcal{G}(\boldsymbol{x})$ with the vorticity, such that

$$\psi(\boldsymbol{x}) = (\mathcal{G} * \omega)(\boldsymbol{x}) = \int_{\mathbb{R}^2} \mathcal{G}(\boldsymbol{x} - \boldsymbol{x}')\omega(\boldsymbol{x}')dA(\boldsymbol{x}'), \tag{2.11}$$

where A is an infinitesimal surface element, and $\mathcal{G}$ is a fundamental solution (Neumann potential) for the Laplace operator ∇^2 (Majda & Bertozzi, 2001)

$$\nabla^2 \mathcal{G}(\boldsymbol{x}) = -\delta(\boldsymbol{x}), \tag{2.12}$$

where $\delta(\boldsymbol{x})$ is the Dirac delta function. In two dimensions, a solution to Eq. 2.12 is

$$\mathcal{G}(\boldsymbol{x}) = -\frac{1}{2\pi} \log |\boldsymbol{x}|. \tag{2.13}$$

Substituting Eq. 2.13 into Eq. 2.11, the stream function is given by

$$\psi(\boldsymbol{x}) = -\frac{1}{2\pi} \int_{\mathbb{R}^2} \log |\boldsymbol{x} - \boldsymbol{x}'| \omega(\boldsymbol{x}')dA(\boldsymbol{x}'), \tag{2.14}$$

and we can recover the velocity field from Eq. 2.9

$$\boldsymbol{u}(\boldsymbol{x}, t) = \int_{\mathbb{R}^2} \boldsymbol{K}(\boldsymbol{x} - \boldsymbol{x}')\omega(\boldsymbol{x}')dA(\boldsymbol{x}'), \tag{2.15}$$

which is known as the Biot-Savart law, and where the kernel $\boldsymbol{K}$ is given by

$$\boldsymbol{K}(\boldsymbol{x} - \boldsymbol{x}') = \frac{1}{2\pi} \left(\frac{-(y - y')}{|\boldsymbol{x} - \boldsymbol{x}'|^2} \quad , \quad \frac{x - x'}{|\boldsymbol{x} - \boldsymbol{x}'|^2} \right)^T. \tag{2.16}$$

From Eq. 2.15, we see that any vorticity distribution in the flow induces a velocity at any point. Eq. 2.8 with Eq. 2.15 represent the vorticity-velocity formulation of the governing equations.

2.3 Singular vorticity distribution: vortex sheets

2.3.1 Self-induced Lagrangian sheet velocity

In the present study, the two-dimensional vortex sheet is described parametrically by introducing the arclength parameter s such that $\boldsymbol{x} = \boldsymbol{x}(s,t)$. Using this parametrization and substituting Eq. 2.1 into Eq. 2.15 yields the transformation of the surface integral into a line integral along the vortex sheet $\boldsymbol{\mathcal{C}}$ as

$$\boldsymbol{u}(\boldsymbol{x},t) = \int_{\boldsymbol{\mathcal{C}}} \boldsymbol{K}(\boldsymbol{x}-\boldsymbol{x}')\gamma(s,t)ds. \tag{2.17}$$

In three dimensions, the integral would be transformed from a volume integral to a surface integral. Eq. 2.17 represents the velocity at any point P in the flow induced by the vortex sheet. Since we are interested in the motion of the vortex sheet, Eq. 2.17 needs to be evaluated at a point on the sheet itself, i.e., when $\boldsymbol{x} \in \boldsymbol{\mathcal{C}}$, which represents the velocity of the sheet induced by itself. The value of the velocity when the point P is on the interface depends on which side P is approaching the interface from, and can be given by the Plemelj formulas (Levinson, 1965)

$$\begin{aligned} \boldsymbol{u}^+ \equiv \lim_{\substack{P\to\boldsymbol{\mathcal{C}} \\ \text{from above}}} \boldsymbol{u} &= \fint_{\boldsymbol{\mathcal{C}}} \boldsymbol{K}[\boldsymbol{x}(s,t)-\boldsymbol{x}(s',t)]\gamma(s',t)\ ds' + \frac{1}{2}\gamma(s,t) \\ \boldsymbol{u}^- \equiv \lim_{\substack{P\to\boldsymbol{\mathcal{C}} \\ \text{from below}}} \boldsymbol{u} &= \fint_{\boldsymbol{\mathcal{C}}} \boldsymbol{K}[\boldsymbol{x}(s,t)-\boldsymbol{x}(s',t)]\gamma(s',t)\ ds' - \frac{1}{2}\gamma(s,t), \end{aligned} \tag{2.18}$$

where now both $\boldsymbol{x}$ and $\boldsymbol{x}'$ belong to the sheet, such that when $\boldsymbol{x} = \boldsymbol{x}'$, the Cauchy principal value of the integral must be taken. In practice, it is common to choose the self-induced velocity of the sheet, denoted by $\boldsymbol{u}^{\text{vs}}$, as the average of the two limiting values, such that

$$\boldsymbol{u}^{\text{vs}} \equiv \frac{\boldsymbol{u}^+ + \boldsymbol{u}^-}{2} = \fint_{\boldsymbol{\mathcal{C}}} \boldsymbol{K}[\boldsymbol{x}(s,t)-\boldsymbol{x}(s',t)]\gamma(s',t)ds'. \tag{2.19}$$

From the value of this velocity, the Lagrangian position of the sheet can be integrated from the relation

$$\frac{d\boldsymbol{x}}{dt} = \boldsymbol{u}^{\text{vs}}. \tag{2.20}$$

2.3.2 Equation governing the sheet strength

Since the sheet strength in Eq. 2.19 is a function of time, its value and spatial distribution along the sheet change as the sheet evolves. An equation describing the evolution of γ is therefore necessary. If one assumes that the sheet strength is independent of time, then $\partial\gamma/\partial t = 0$, and Eq. 2.19 can be solved given appropriate initial and boundary conditions. In this limit, the problem is purely kinematic. In reality, the sheet strength varies in space and time due to the dynamics of motion. Although this thesis is concerned with two-dimensional vortex sheets, great insights into the physical interpretation of the sheet-strength governing equation can be gained from the three-dimensional case. We will therefore derive the sheet-strength equation in 3D first, followed by the derivation in 2D. The following derivations can be found in greater detail in other studies (Pozrikidis, 2000; Wu, 1995; Wu *et al.*, 2005, 2007; Stock, 2006).

2.3.2.1 Three-dimensional vortex sheets

A vortex sheet described in three dimensions is actually a two-dimensional surface that can deform in a 3D fashion. In this case, a vortex sheet is defined as

$$\boldsymbol{\omega} = \boldsymbol{\zeta}\delta(n), \tag{2.21}$$

where $\boldsymbol{\zeta}$ is now the vectorial sheet strength with two components in the plane of the sheet, and defined as

$$\boldsymbol{\zeta} = \hat{\boldsymbol{N}} \times \Delta\boldsymbol{u}. \tag{2.22}$$

From the definition of the sheet velocity, Eq. 2.19, we can express the fluid velocity on each side of the sheet in terms of the sheet velocity and the velocity jump as

$$\boldsymbol{u}^{+} = \boldsymbol{u}^{\text{vs}} - \frac{1}{2}\Delta\boldsymbol{u} \qquad , \qquad \boldsymbol{u}^{-} = \boldsymbol{u}^{\text{vs}} + \frac{1}{2}\Delta\boldsymbol{u}. \tag{2.23}$$

The goal is then to derive an evolution equation for the velocity jump $\Delta\boldsymbol{u}$, which allows us to relate it to the vortex sheet strength $\boldsymbol{\zeta}$. To this end, we start from the Euler equations on each side of the interface

$$\frac{\partial \boldsymbol{u}^{\pm}}{\partial t} + \left(\boldsymbol{u}^{\pm} \cdot \nabla\right) \boldsymbol{u}^{\pm} = \boldsymbol{g} - \frac{1}{\rho^{\pm}} \nabla p^{\pm}. \tag{2.24}$$

After taking the curl of Eq. 2.24, the problem where the right-hand-side of Eq. 2.24 is ignored is first examined, which corresponds to the case where the effects of baroclinic vorticity are ignored. Doing so allows me to identify the kinematic contributions to the evolution of the sheet strength. After multiple steps described in Appx. A.1.1, the evolution equation of the sheet strength when there is no baroclinic mechanism is

$$\frac{D\boldsymbol{\zeta}}{Dt} = \underbrace{\left(\boldsymbol{\zeta} \cdot \nabla\right) \boldsymbol{u}^{\text{vs}}}_{\text{vortex stretching}} - \underbrace{\boldsymbol{\zeta} \nabla_s \cdot \boldsymbol{u}^{\text{vs}}}_{\text{sheet expansion}} , \tag{2.25}$$

where $\frac{D(\cdot)}{Dt} = \frac{\partial(\cdot)}{\partial t} + \left(\boldsymbol{u}^{\text{vs}} \cdot \nabla\right)(\cdot)$ is the total derivative with respect to the sheet velocity, and $\nabla_s \cdot \boldsymbol{u}^{\text{vs}} \equiv \left(\boldsymbol{P} \cdot \nabla\right) \cdot \boldsymbol{u}^{\text{vs}}$ is the surface divergence, where $\boldsymbol{P} = \boldsymbol{I} - \hat{\boldsymbol{N}} \otimes \hat{\boldsymbol{N}}$ is a tangential projection operator, with $\boldsymbol{I}$ the identity matrix. The surface divergence emerges when considering the evolution of a material surface in curvilinear coordinates. Eq. 2.25 reveals that the rate of change of the sheet-strength with time is a combination of vorticity stretching due to velocity gradients (the familiar vortex-stretching term), and vorticity change due to the sheet-velocity distribution (second term). The second term represents the rate of change of the surface area, and expresses the expansion or contraction of the sheet in the tangential direction. This term is not to be associated with the compressible term in the vorticity

equation (Eq. 2.4). As opposed to dilatation due to compressibility, which is a volumetric process, the sheet-expansion term is a surface process, which is non-zero even in the case of incompressible flows.

Let us now take into account the mechanism of baroclinic vorticity generation, and follow similar steps, shown in detail in Appx. A.1.2. The final equation for the sheet-strength evolution is then

$$\frac{D\boldsymbol{\zeta}}{Dt} = \underbrace{(\boldsymbol{\zeta}\cdot\nabla)\,\boldsymbol{u}^{\text{vs}}}_{\text{vortex stretching}} - \underbrace{\boldsymbol{\zeta}\nabla_s\cdot\boldsymbol{u}^{\text{vs}}}_{\text{sheet expansion}} \underbrace{-2A\,\hat{\boldsymbol{N}}\times(\bar{\boldsymbol{a}}-\boldsymbol{g})}_{\text{baroclinic}} + \underbrace{\frac{2}{\rho^+ + \rho^-}\,\hat{\boldsymbol{N}}\times\nabla\left(p^+ - p^-\right)}_{\text{surface tension}}, \tag{2.26}$$

where $A = (\rho^- - \rho^+)/(\rho^- + \rho^+)$ is the Atwood number, and $\bar{\boldsymbol{a}}$ is the average of the fluid acceleration on each side of the sheet given by (see Appx. A.1.2 for details)

$$\bar{\boldsymbol{a}} \equiv \frac{1}{2}\left(\left.\frac{D\boldsymbol{u}^+}{Dt}\right|_{\text{fluid}} + \left.\frac{D\boldsymbol{u}^-}{Dt}\right|_{\text{fluid}}\right) = \underbrace{\frac{D\boldsymbol{u}^{\text{vs}}}{Dt}}_{\text{sheet acceleration}} + \frac{1}{4}\underbrace{(\Delta\boldsymbol{u}\cdot\nabla)\,\Delta\boldsymbol{u}}_{\text{strength advection}}. \tag{2.27}$$

We see that now the sheet strength is governed by two additional terms: the baroclinic term and a term that would correspond to a surface tension term (if surface tension was considered). Eq. 2.27 reveals that baroclinic vorticity is generated by the self-induced acceleration of the sheet, and by the advection of the jump velocity with 1/4 of the jump velocity.

2.3.2.2 Two-dimensional vortex sheets

In two dimensions, we can write Eq. 2.23 as

$$\boldsymbol{u}^+ = \boldsymbol{u}^{\text{vs}} - \frac{1}{2}\gamma\hat{\boldsymbol{T}} \qquad , \qquad \boldsymbol{u}^- = \boldsymbol{u}^{\text{vs}} + \frac{1}{2}\gamma\hat{\boldsymbol{T}}, \tag{2.28}$$

such that, when substituting it in Eq. 2.24 and projecting onto the tangential direction, the following expression is obtained (see Appx. A.2)

$$\frac{D\gamma}{Dt} = \underbrace{-\gamma \frac{\partial \boldsymbol{u}^{\text{vs}}}{\partial s} \cdot \hat{\boldsymbol{T}}}_{\text{sheet expansion}} \underbrace{- 2A\left(\bar{\boldsymbol{a}} - \boldsymbol{g}\right) \cdot \hat{\boldsymbol{T}}}_{\text{baroclinic}} + \underbrace{\frac{2}{\rho^+ + \rho^-} \nabla \left(p^+ - p^-\right) \cdot \hat{\boldsymbol{T}}}_{\text{surface tension}}, \tag{2.29}$$

where

$$\bar{\boldsymbol{a}} \cdot \hat{\boldsymbol{T}} = \frac{D\boldsymbol{u}^{\text{vs}}}{Dt} \cdot \hat{\boldsymbol{T}} + \frac{1}{8} \frac{\partial \gamma^2}{\partial s}. \tag{2.30}$$

Eq. 2.30 is the two-dimensional counterpart of Eq. 2.27, and indicates that the advection of the jump velocity is related to the sheet-strength advection; it is a nonlinear advection term similar to a nonlinear advection equation.

2.4 Summary of the governing equations

In light of the previous sections, we present here a summary of the governing equations that are solved in this work. We recall that we only consider the evolution of two-dimensional periodic vortex sheets with no surface tension effects. Furthermore, since we adopt a Lagrangian description of the vortex-sheet motion, i.e., the equations are solved in the reference frame of the sheet, the total derivative with respect to the sheet velocity, $\frac{D(\cdot)}{Dt} = \frac{\partial(\cdot)}{\partial t} + \left(\boldsymbol{u}^{\text{vs}} \cdot \nabla\right)(\cdot)$, reduces to the Lagrangian derivative $\frac{d(\cdot)}{dt}$. The vortex sheet governing equations are then

$$\text{Sheet velocity:} \quad \frac{d\boldsymbol{x}}{dt} = \boldsymbol{u}^{\text{vs}} = \int_{\boldsymbol{\mathcal{C}}} \boldsymbol{K}[\boldsymbol{x}(s,t) - \boldsymbol{x}(s',t)]\gamma(s',t)ds' \tag{2.31}$$

$$\text{Sheet strength:} \quad \frac{d\gamma}{dt} = -2A\left(\frac{d\boldsymbol{u}^{\text{vs}}}{dt} \cdot \hat{\boldsymbol{T}} + \frac{1}{8}\frac{\partial \gamma^2}{\partial s} - \boldsymbol{g}(t) \cdot \hat{\boldsymbol{T}}\right) - \gamma \frac{\partial \boldsymbol{u}^{\text{vs}}}{\partial s} \cdot \hat{\boldsymbol{T}}, \tag{2.32}$$

where $\boldsymbol{K}$ is the periodic Biot-Savart kernel

$$\boldsymbol{K} = \frac{1}{2\lambda}\left(\begin{array}{c} \dfrac{-\sinh[k(y-y')]}{\cosh[k(y-y')]-\cos[k(x-x')]+\delta^2} \\ \\ \dfrac{\sin[k(x-x')]}{\cosh[k(y-y')]-\cos[k(x-x')]+\delta^2}, \end{array}\right), \tag{2.33}$$

which is desingularized by a smoothing parameter δ (Krasny, 1986*a*), such that the Cauchy principal value integral does not need to be taken when evaluating the velocity. In all the results presented in the next chapters, $\delta = 0.1$ is chosen, which was also used in previous investigations (Sohn, 2011). The Atwood number is defined as $A = \frac{\rho^- - \rho^+}{\rho^+ + \rho^-}$, where $\rho^{\pm}$ is the fluid density on either side of the sheet (see Fig. 2.1). The three terms multiplying the Atwood number represent the change in vortex-sheet strength due to generation of baroclinic vorticity. The first term is the acceleration of a point on the interface $d\boldsymbol{u}^{\mathrm{vs}}/dt$ due to the self-induced motion of the sheet. The second non-linear term corresponds to the advection of the sheet strength along the sheet. When combined together, these two terms represent the average of the fluid acceleration on each side of the sheet in the tangential direction (Tryggvason, 1988; Pozrikidis, 2000). The third term $\boldsymbol{g}(t)$ is a time-dependent acceleration accounting for the fact that the interface may not be in an inertial reference frame. The fourth term represents the expansion/contraction of the sheet in the tangential direction.

The initial conditions are determined by the shape of the initial perturbation, and the corresponding sheet-strength distribution. The initial perturbation is characterized by its wavelength λ (wavenumber $k = 2\pi/\lambda$), and the amplitude-to-wavelength ratio a_0/λ. In Sec. 2.6, I show how the sheet-strength distribution is determined for RM-type problems. Because we are considering periodic perturbations, periodic boundary conditions are applied. The important parameters governing the problem are the amplitude-to-wavelength ratio, the Atwood number, and the magnitude of the initial sheet-strength distribution, γ_0.

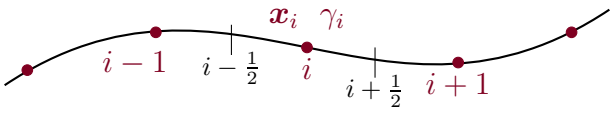

Figure 2.2: Schematic of the vortex sheet discretization

2.5 Numerical discretization

2.5.1 Discretization of the governing equations

A common approach to discretize the equations is to use the point vortex method first introduced by Rosenhead (1931). In this approach the vortex sheet is discretized into N arclength elements of length $\Delta s_i = s_{i+1/2} - s_{i-1/2}$, $i = 1 : N$, with position $\boldsymbol{x}_i$, each corresponding to a point vortex of strength γ_i, as depicted in Fig. 2.2. The arclength element ds is defined as $ds = \sqrt{dx^2 + dy^2}$, where the elements dx and dy are given by $dx = x_{i+1/2} - x_{i-1/2}$ and $dy = y_{i+1/2} - y_{i-1/2}$ such that

$$\Delta s_i = \sqrt{\left(x_{i+1/2} - x_{i-1/2}\right)^2 + \left(y_{i+1/2} - y_{i-1/2}\right)^2}. \tag{2.34}$$

The point $\boldsymbol{x}_{i+1/2}$ (respectively, $\boldsymbol{x}_{i-1/2}$) is evaluated halfway between the points $\boldsymbol{x}_i$ and $\boldsymbol{x}_{i+1}$ (respectively, $\boldsymbol{x}_{i-1}$ and $\boldsymbol{x}_i$), i.e., $\boldsymbol{x}_{i+1/2} = (\boldsymbol{x}_i + \boldsymbol{x}_{i+1})/2$ and $\boldsymbol{x}_{i-1/2} = (\boldsymbol{x}_{i-1} + \boldsymbol{x}_i)/2$, such that $\Delta s_i = \frac{1}{2}|\boldsymbol{x}_{i+1} - \boldsymbol{x}_{i-1}|$. The circulation Γ_i enclosed by a contour around Δs_i is given by

$$\Gamma_i = \int_{s_{i-1/2}}^{s_{i+1/2}} \gamma_i ds = \gamma_i \Delta s_i. \tag{2.35}$$

For convenience, in the results presented in Chapter 4, we sometimes use a Lagrangian parameter α_i instead of the arclength to plot the quantities of interest. Eqs. 2.31 and 2.32 are discretized by second-order finite differences, with the exception of the second term in Eq. 2.32, which is a non-linear flux term solved using the Godunov method (LeVeque, 1992;

Toro, 2013). The physical flux, $f(\gamma) = \frac{2A}{8}\gamma^2$, is used to evaluate the numerical flux, F, by solving a Riemann problem at the cell boundaries $s_{i\pm1/2}$, such that $F_{i+1/2} = F(\gamma_i, \gamma_{i+1})$ and $F_{i-1/2} = F(\gamma_{i-1}, \gamma_i)$. The integral in Eq. 2.31 is discretized by using the midpoint rule. The coupled Eqs. 2.31 and 2.32 constitute a Fredholm equation of the second kind, whose solution is complicated by the presence of the term $d\boldsymbol{u}^{\rm vs}/dt$ on the right-hand-side of Eq. 2.32. This difficulty is resolved by following an iterative procedure (Tryggvason, 1988). The discretized version of Eqs. 2.31 and 2.32 form a set of $3N$ ordinary differential equations

$$\begin{aligned}
\frac{dx_i}{dt} &= \frac{1}{2\lambda}\sum_{j=1}^{N} \frac{-\sinh[k(y_i - y_j)]}{\cosh[k(y_i - y_j)] - \cos[k(x_i - x_j)] + \delta^2}\ \gamma_j \Delta s_j \\
\frac{dy_i}{dt} &= \frac{1}{2\lambda}\sum_{j=1}^{N} \frac{\sin[k(x_i - x_j)]}{\cosh[k(y_i - y_j)] - \cos[k(x_i - x_j)] + \delta^2}\ \gamma_j \Delta s_j \\
\frac{d\gamma_i}{dt} &= -2A\left(\frac{d\boldsymbol{u}_i^{\rm vs}}{dt}\cdot\hat{\boldsymbol{T}}_i - \boldsymbol{g}_i\cdot\hat{\boldsymbol{T}}_i\right) - \frac{F_{i+1/2} - F_{i-1/2}}{\Delta s_i} - \gamma_i \frac{\boldsymbol{u}_{i+1}^{\rm vs} - \boldsymbol{u}_{i-1}^{\rm vs}}{2\Delta s_i}\cdot\hat{\boldsymbol{T}}_i.
\end{aligned} \tag{2.36}$$

By definition, the tangential vector is given by

$$\hat{\boldsymbol{T}}(s) = \frac{\boldsymbol{x}'(s)}{|\boldsymbol{x}'(s)|} = \frac{d\boldsymbol{x}}{ds}, \tag{2.37}$$

and is numerically computed using $\hat{\boldsymbol{T}}_i = (\boldsymbol{x}_{i+1/2} - \boldsymbol{x}_{i-1/2})/\Delta s_i$. The system of equations is advanced in time using an explicit second-order Runge-Kutta scheme. To provide sufficient spatial resolution to accurately describe the interface distortion and roll-up features at late time, a point insertion procedure is implemented, and is described next.

2.5.2 Point-insertion procedure

The point-insertion procedure is based on the relative distance between neighboring points (Krasny, 1987; Feng *et al.*, 2009), as depicted in Fig. 2.3. If either of the two distances d or h are greater than a certain threshold, two additional points (red points) are inserted,

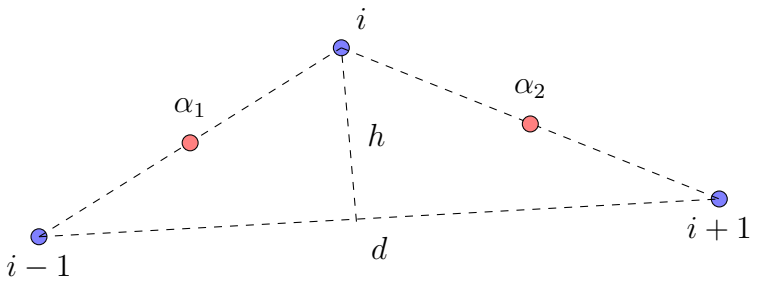

Figure 2.3: Schematic of the point-insertion procedure. Original points: blue, inserted points: red.

one between the points $\boldsymbol{x}_{i-1}$ and $\boldsymbol{x}_i$, and the other between the points $\boldsymbol{x}_i$ and $\boldsymbol{x}_{i+1}$. These two additional points are inserted with respect to a Lagrangian parameter α, such that $\alpha_1 = (\alpha_{i-1} + \alpha_i)/2$ and $\alpha_2 = (\alpha_i + \alpha_{i+1})/2$. The position, velocity, and sheet strength at the new points are then determined by a third-order Lagrange interpolation. To verify this procedure, we consider two cases allowing us to observe the convergence of the results when applying our point-insertion procedure. For convenience, we call the point-insertion procedure "AMR" (Adaptive-Mesh Refinement),

The first case considers the evolution of an initially flat interface with no density mismatch ($A = 0$), subjected to velocity perturbations of the form (Rikanati *et al.*, 1998)

$$\begin{cases} u(x,y) = v_0 \sin(kx)\,(2H(y) - 1)\,e^{-k|y|} \\ v(x,y) = v_0 \cos(kx) e^{-k|y|}, \end{cases} \tag{2.38}$$

where $v_0 = 0.01$ m/s is the initial velocity, $k = 2\pi/\lambda$ is the wavenumber ($\lambda = 0.01$ m), and $H(y)$ is the Heaviside function given by

$$H(y) = \begin{cases} 1 & \text{if } \; y > 0 \\ 0 & \text{if } \; y < 0. \end{cases} \tag{2.39}$$

Since $A = 0$, by Kelvin's theorem of circulation, the total circulation along a contour around

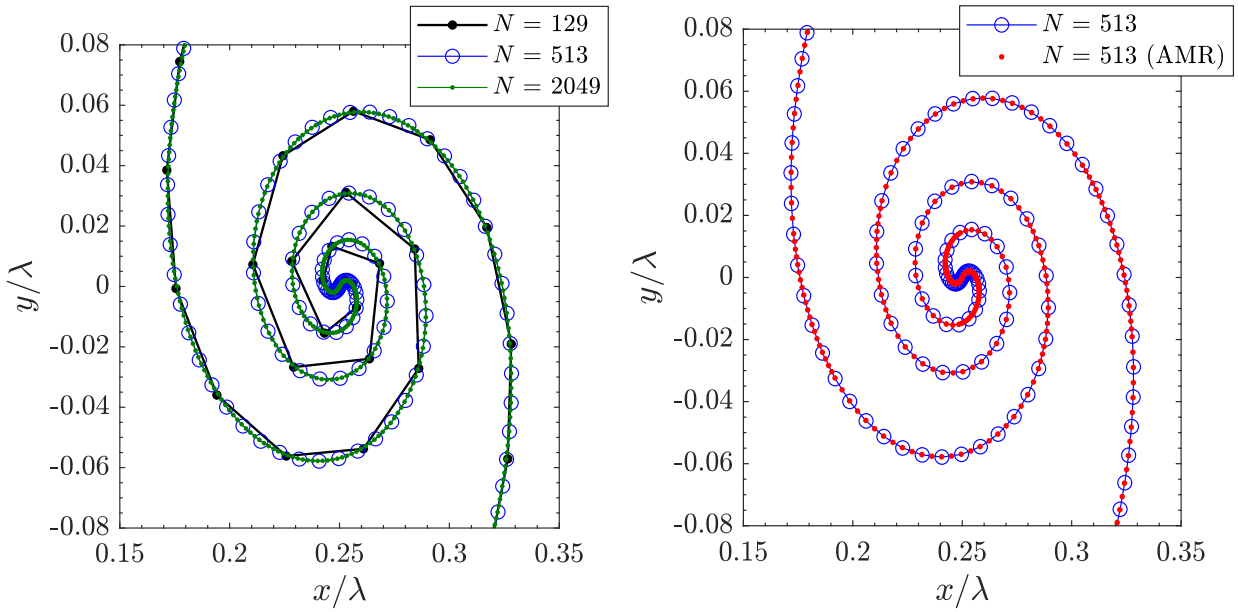

(a) Without AMR.

(b) With AMR.

Figure 2.4: Interface morphology for the velocity-perturbations case (a) without AMR for different resolutions, and (b) with AMR. The red points on the right figure corresponds to the solution obtained with AMR (starting with $N = 513$ points).

the interface stays constant over time and is given by

$$\Gamma = \frac{4v_0}{k}. \tag{2.40}$$

To non-dimensionalize the variables, we choose the wavelength and sound speed ($c = 1$ m/s) as characteristic length and velocity, respectively. In this case, the dimensionless exact circulation is $\Gamma/(\lambda c) \approx 6.37 \cdot 10^{-3}$. Fig. 2.4 shows the interface morphology at a given time for three different resolutions, and for the procedure with AMR (starting with $N = 513$ points). The solution obtained without AMR converges with the number of points when $N \to \infty$. For a chosen initial number of points, the solution obtained with AMR gives a more accurate representation of the roll-up than the one obtained without AMR. Fig. 2.5 shows the convergence of the total circulation to the exact solution (Eq. 2.40) when increasing the number of points, along with the interface length. The solution obtained when using AMR slightly overpredicts the total circulation compared to the $N = 2049$ case.

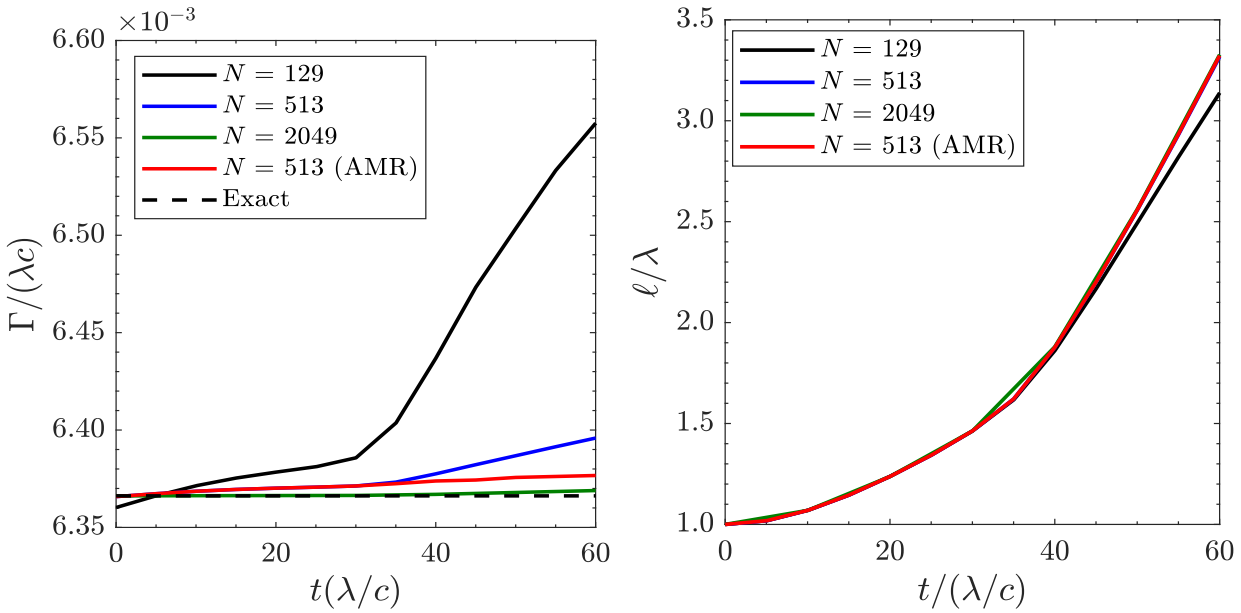

(a) Total circulation.

(b) Interface length.

Figure 2.5: Time evolution of (a) the total circulation over half a wavelength, and (b) the interface length, for different resolutions in the velocity-perturbations case. The red line corresponds to the solution obtained with AMR (starting with $N = 513$ points).

Since the AMR solution is not as resolved as the $N = 2049$ solution ($N = 1393$ by the end of the simulation), one may argue that the discrepancy is due to the fewer number of points in the AMR solution. However, the discrepancy is due to the fact that the improvement of the solution obtained with AMR is relative to the number of points chosen initially. In our case, the initial number points is $N = 513$, thus improving the solution with respect to the one obtained with a fixed number of points corresponding to $N = 513$.

Next, we consider the case corresponding to the RM experiments of Collins & Jacobs (2002), where the Atwood number is $A \approx 0.6$, and is investigated in great detail in Chapter 4. We therefore do not include the problem set-up again here. Fig. 2.6 shows the convergence of the interface morphology and the total circulation when using our AMR procedure.

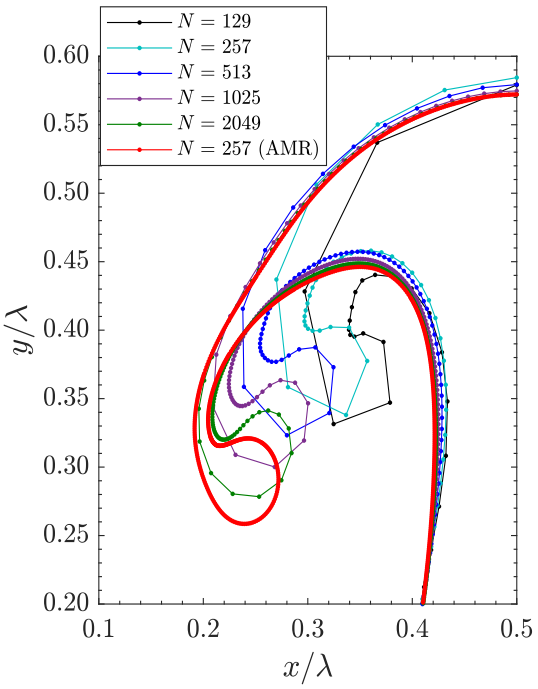

(a) Interface morphology

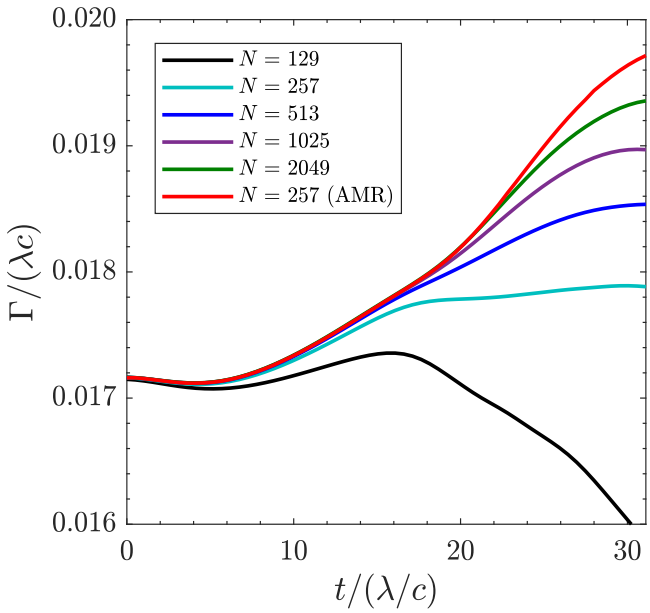

(b) Total circulation

Figure 2.6: (a) Interface morphology, and (b) total circulation over half a wavelength for different resolutions and AMR in the RM case.

2.6 Initial conditions

The set of Eqs. 2.31 and 2.32 constitutes an initial-value problem, thus requiring initial values for the position of the interface $\boldsymbol{x}$ and the sheet-strength γ. Because the present work focuses on RM-type problems, i.e., a shock wave impinging upon an interface, the sheet strength before the shock reaches the interface is zero. Therefore, the initial conditions of a vortex sheet in an RM environment must be determined after the passage of the shock over the interface. This requirement poses great challenges when initializing vortex sheet computations, as one must know the change in the initial shape of the perturbation caused by the passage of the shock, and the corresponding sheet-strength distribution.

In a light-to-heavy configuration (when there is no phase inversion), if the initial amplitude of the perturbation is small relative to its wavelength, the change in interface morphology due to the passage of the shock may be neglected. In this case, the pre-shock

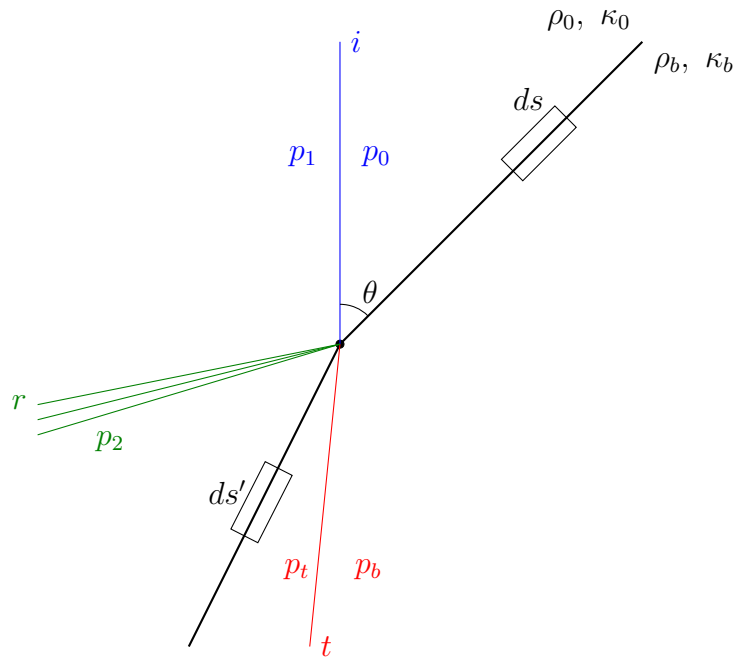

Figure 2.7: Schematic of shock refraction at an inclined planar interface. Blue: incident shock (i), red: transmitted shock (t), green: reflected shock or rarefaction (r), and black: interface.

perturbation is the same as the post-shock one. This configuration is adopted in Chapter 4. However, in a heavy-to-light configuration (when a phase inversion occurs), three cases need to be considered. The first is when the speed of the shocked interface, u_{int}, is greater than the speed of the incident shock, u_{shock}, called direct phase inversion (Holmes *et al.*, 1999), such that the perturbation inverts during shock transit. The second is when $u_{\text{int}} < u_{\text{shock}}$, called indirect phase inversion, in which case the perturbation inverts after the passage of the shock. The third is when $u_{\text{int}} \approx u_{\text{shock}}$, in which case the perturbation is flat at the time the shock leaves the interface. The latter case is the one relevant to Chapter 3; in the HED experiments, the shocked interface speed is nearly identical to the incident shock, such that the post-shock interface can be considered flat.

Samtaney & Zabusky (1994) developed a model allowing the determination of the circulation per unit length, i.e., the sheet strength, on planar tilted interfaces, as shown in Fig. 2.7. For convenience, we refer to their model as the SZ model. The SZ model is based on shock-polar analysis, which considers the deviation of the flow due to the refraction of the

incident shock at the interface. By definition (Henderson, 1989), shock refraction occurs when the speed of an incident shock i changes when propagating from one fluid (density ρ_0, ratio of specific heat κ_0) to another (density ρ_b, ratio of specific heat κ_b). The interaction between an incident shock and an interface produces a transmitted wave t, and a reflected wave r. The transmitted wave is always a shock, whereas the reflected wave can be a shock or a rarefaction. If the speed of the transmitted shock is larger (respectively, smaller) than the speed of the incident shock, the refraction is known as "slow-fast" (respectively, "fast-slow"). If the refraction is regular, i.e., the system of waves meets at a single node, the circulation per unit length can be derived analytically, and is given, for the fast-slow case, by

$$\frac{d\Gamma}{ds} = c_0 \left[\sqrt{F_1 + \frac{M_s^2}{\sin^2\theta}} - \sqrt{F_2 + \frac{M_s^2}{\sin^2\theta}} \right] \frac{\cos\theta}{\cos(\theta - \delta_b)}, \tag{2.41}$$

where c_0 is the sound speed in fluid 0, M_s is the incident shock Mach number, and F_1 and F_2 are two functions given by

$$\begin{aligned} F_1 &= \frac{2\kappa_b}{\kappa_0(\kappa_b - 1)} \frac{1 - A}{1 + A} \left[1 - \psi\left(\frac{p_2}{p_0}, \mu_b \right) \right] \\ F_2 &= \frac{2}{\kappa_0 - 1} \left[1 - \psi\left(\frac{p_2}{p_1}, \mu_0 \right) \psi\left(\frac{p_1}{p_0}, \mu_0 \right) \right] \end{aligned} \tag{2.42}$$

where $\mu_i^2 \equiv (\kappa_i - 1)/(\kappa_i + 1)$ $(i = 0, b)$, and p_1/p_0, p_2/p_0, and p_2/p_1 are the pressure ratios across the incident, transmitted, and reflected waves, respectively. The function $\psi(\xi, \zeta)$ is a function of two variables defined as

$$\psi(\xi, \zeta) = \xi \frac{1 + \zeta^2 \xi}{\zeta^2 + \xi}. \tag{2.43}$$

The factor $\cos\theta / \cos(\theta - \delta_b)$ is a geometric factor taking into account the change in interface length due to the passage of the incident shock. The angle δ_b is the streamline deflection in the fluid b due to the transmitted wave, and is determined by the equations of shock polars. The pressure ratio p_2/p_0 can be determined by solving a twelve-degree polynomial in p_2/p_0,

which also depends on the streamline deflections due to each wave. Note that the functions F_1 and F_2 are implicitly dependent on the shock Mach number as well.

When the refraction is irregular, e.g., due to large tilt angles θ, Eq. 2.41 does not hold, as no physically relevant solutions to the polynomial solving for the pressure ratio p_2/p_0 exist. In such cases, Samtaney & Zabusky (1994) derived an approximate expression by expanding the exact expression into a Taylor series about $\sin\theta = 0$

$$\frac{d\Gamma}{ds} = \sigma_1 \sin\theta + \sigma_3 \sin^3\theta + \mathcal{O}(\sin^5\theta), \tag{2.44}$$

where

$$\sigma_1 = \frac{c_0}{2M_s}\left(\tilde{F}_1 - \tilde{F}_2\right), \tag{2.45}$$

and $\tilde{F}_{1,2}$ are the values of the functions F_1 and F_2 evaluated at p_2/p_0 in the limiting case $\theta \to 0$. In this case, the pressure ratio p_2/p_0 is the solution to the algebraic equation of the one-dimensional Riemann problem

$$\frac{p_1/p_0 - 1}{\sqrt{\mu_0^2 + p_1/p_0}} - \frac{p_2/p_1 - 1}{\sqrt{\mu_0^2 + p_2/p_1}}\sqrt{\psi\left(\frac{p_1}{p_0}, \mu_0\right)} - \sqrt{\frac{1-A}{1+A}}\frac{p_2/p_0 - 1}{\sqrt{\mu_b^2 + p_2/p_0}}\sqrt{\frac{\kappa_0 + 1}{\kappa_b + 1}} = 0. \tag{2.46}$$

The expression for the coefficient σ_3 is too complicated to be considered here, and was shown to have a negligible influence on the circulation value. Therefore, we only consider the approximation to first order in $\sin\theta$. Eq. 2.44 directly gives the expression for the sheet strength γ, since by definition,

$$\gamma = \frac{d\Gamma}{ds}. \tag{2.47}$$

In the case of a sinusoidal perturbation, the angle θ between the shock and the interface varies along the interface, such that a distribution for the sheet strength is obtained. Note that the above equations are valid for the fast-slow case only, where the reflected wave is a shock. For the slow-fast case, where the reflected wave is a rarefaction, Samtaney *et al.* (1998) derived similar expressions.

CHAPTER 3

Vortex-Sheet Modeling of Hydrodynamic Instabilities Produced by an Oblique Shock Interacting with a Perturbed Interface in the HED Regime

This chapter is adapted from Pellone *et al.* (2021)

3.1 Abstract

We consider hydrodynamic instabilities produced by the interaction of an oblique shock with a perturbed material interface under high-energy-density (HED) conditions. During this interaction, a baroclinic torque is generated along the interface due to the misalignment between the density and pressure gradients, thus leading to perturbation growth. Our objective is to understand the competition between the impulsive acceleration due to the normal component of the shock velocity, which drives the Richtmyer-Meshkov instability, and the shear flow across the interface due to the tangential component of the shock velocity, which drives the Kelvin-Helmholtz instability, as well as its relation to perturbation growth. Since the vorticity resulting from the shock-interface interaction is confined to the interface, we describe the perturbation growth using a two-dimensional vortex-sheet model. We demonstrate the ability of the vortex-sheet model to reproduce roll-up dynamics for non-zero Atwood numbers by comparing to past laser-driven HED experiments. We determine the dependence of the interface dynamics on the tilt angle and propose a time scaling for the

perturbation growth at early time. Eventually, this scaling will serve as a platform for the design of future experiments. This study is the first attempt to incorporate into a vortex-sheet model the time-dependent interface decompression and the deceleration (as well as the corresponding Rayleigh-Taylor instability) arising from laser turn-off.

3.2 Introduction

The growth of perturbations due to hydrodynamic instabilities at material interfaces plays an important role in the evolution of high-energy-density systems (HED), as it initiates multi-material mixing, possibly altering the overall flow dynamics of such systems. In inertial confinement fusion, for example, the growth of Rayleigh-Taylor (Rayleigh, 1900; Taylor, 1950) (RT), Richtmyer-Meshkov (Richtmyer, 1960; Meshkov, 1969) (RM), and Kelvin-Helmholtz (Thomson Lord Kelvin, 1871; Helmholtz, 1868) (KH) instabilities may cause the outer cold ablator material to mix with the central hot spot, thus degrading the performance of capsule implosions (Meezan *et al.*, 2013; Hicks *et al.*, 2012). At larger scales, the development of RT and RM instabilities in core-collapse supernovae also cause material mixing (Abarzhi *et al.*, 2018; Kane *et al.*, 1997). The KH instability plays a critical role in the development of turbulent boundary layers in planetary atmospheres (Johnson *et al.*, 2014). Under HED conditions, shock-driven instabilities have been investigated at high-energy laser facilities by depositing kilojoules of laser energy into millimiter-size targets, leading to instabilities growing over nanoseconds (Drake, 2010; Ryutov & Remington, 2002; Remington, 2005; Remington *et al.*, 2019).

Beyond the early linear stage, the flow dynamics resulting from the growth of these instabilities sometimes involve combined effects of RM, RT, and/or KH (Kuranz *et al.*, 2009). Much of the past work on shock-driven perturbation growth at interfaces has emphasized a single one of these instabilities (Jacobs & Krivets, 2005; Jacobs & Catton, 1988*a*,*b*; Zhou, 2017*a*,*b*); less attention has been paid to combinations. In the conventional RM instability,

the shock front propagates in the direction normal to the mean interface, thereby causing an impulsive acceleration (Malamud *et al.*, 2013*a*; Di Stefano *et al.*, 2015*b*,*a*; Nagel *et al.*, 2017; Dimonte *et al.*, 1996; Aglitskiy *et al.*, 2006, 2010). In a shock-driven KH geometry, the shock front propagates in the direction tangential to the mean interface, producing a shear across the interface (Harding *et al.*, 2009; Hurricane, 2008; Flippo *et al.*, 2018; Doss *et al.*, 2020; Malamud *et al.*, 2013*b*; Wan *et al.*, 2015, 2017). The intermediate case of a mean interface tilted with respect to the incident shock wave, or an oblique shock interacting with an interface, introduces elements of shear in addition to the impulsive acceleration from the shock, such that both RM and KH instabilities contribute to perturbation growth.

Rasmus *et al.* (2018, 2019) showed that varying the tilt angle alters the relative importance of KH and RM in their HED experiments. However, they studied only a small number of initial conditions and their model did not include post-shock baroclinic vorticity generation effects, which occur due to the misalignment of the density gradient across the interface with the pressure gradient across the incident shock. The late-time, non-linear dynamics of perturbation growth are characterized by the formation of large vortical structures, which dominate and eventually drive the mixing. Baroclinic vorticity generation alters the formation of these structures and is therefore critical to include in the description of the non-linear perturbation growth. Of particular interest to this work is the post-shock generation of baroclinic vorticity due to the self-induced acceleration of the interface and vorticity transport along the interface. As the shock interacts with the interface, a sheet of vorticity is generated along the interface due to the misalignment of the density gradient (across the interface) and the pressure gradient (across the shock) (Zabusky, 1999; Brouillette, 2002). This baroclinic torque causes interfacial perturbations to grow, eventually giving rise to familiar bubble and spike structures. Furthermore, in HED experiments, laser turn-off gives rise to a rarefaction that can affect perturbation growth. Experimental studies of these phenomena in the HED regime require specialized facilities and expertise, and generally do not yield large amounts of data. Numerical simulations of shock-driven interfacial instabilities necessitate

significant resolution and modeling of complex physics (laser-matter interaction, radiation-hydrodynamics, turbulence). Although such approaches are comprehensive in the physics they account for, it is difficult to isolate specific contributions to perturbation growth, e.g., the role of vorticity dynamics.

The initial growth of perturbations can be determined from the interface velocity induced by this baroclinic torque. The relationship between vorticity and velocity, i.e., the Biot-Savart law (Saffman, 1992; Pozrikidis, 2011), allows the problem to be reduced to evolving the interface from an initial distribution of vorticity along the interface. Vortex-sheet models are uniquely designed to represent vorticity-dominated interfacial dynamics. This paradigm is computationally attractive as it provides a one-dimensional parametrization of a two-dimensional interface, which allows for a detailed description of roll-up behavior lacking in current theoretical models of both linear (Richtmyer, 1960; Yang *et al.*, 1994*b*; Wouchuk & Nishihara, 1996, 1997) and non-linear (Zhang & Sohn, 1996, 1997*a*; Alon *et al.*, 1995; Oron *et al.*, 2001) phases of the growth. In classical fluid dynamics, Rosenhead (1931) considered the evolution of a vortex sheet discretized as a set of point vortices applied to the KH instability. Numerical difficulties associated with roll-up formation, leading to curvature singularity, have been investigated for cases with (Baker *et al.*, 1982; Higdon & Pozrikidis, 1985; Pozrikidis, 2000; Sohn *et al.*, 2010) and without (Krasny, 1986*b*,*a*, 1987; Tryggvason, 1989) a density jump across the interface. The inclusion of a density jump in the vortex-sheet formulation complicates both the physical model and the numerical treatment of the equations, as additional non-linear terms must be incorporated in the equation governing the time evolution of the vortex sheet. Previous studies have successfully investigated RT (Tryggvason, 1988; Sohn, 2011, 2004; Zufiria, 1988) and RM (Matsuoka *et al.*, 2003; Matsuoka & Nishihara, 2006*c*) instabilities using the vortex-sheet model with these additional terms. A challenge with vortex-sheet modeling lies in prescribing initial conditions as current strategies have been developed for traditional fluid systems (Samtaney & Zabusky, 1994). Under HED conditions, however, the dynamics of vortex sheets have yet to be used, with the exception

of the purely kinematic study of Rasmus *et al.* (2019).

In this work, we use a vortex-sheet model to investigate the growth of interfacial perturbations subject to an oblique shock under HED conditions. HED-relevant initial conditions are prescribed by combining an analytical model with complementary hydrodynamic simulations. To better understand the relative importance of impulsive acceleration vs. shear, we investigate the dependence of the interface morphology on the initial tilt angle. This work is the first account of using a vortex-sheet model to describe a problem in the HED regime and predict secondary effects from experimental laser turn-off, such as time-dependent interface deceleration and decompression, as opposed to prior vortex-sheet modeling of constant-acceleration RT instability (Tryggvason, 1988; Sohn, 2011, 2004; Zufiria, 1988). The manuscript is organized as follows. First, we describe the vortex-sheet paradigm and the governing equations, along with a strategy allowing the determination of the vortex-sheet strength distribution following the passage of the shock. Next, we investigate the dynamics for a given tilt angle and density jump, corresponding to the experiments performed by Rasmus *et al.* (2018, 2019). The role of the tilt angle on the perturbation growth is then examined, before ending with concluding remarks.

3.3 Governing equations and numerical discretization

During the interaction of a shock wave with a perturbed interface, a baroclinic torque is generated along the interface due to the misalignment between the density gradient across the interface, $\boldsymbol{\nabla}\rho$, and the pressure gradient across the shock wave, $\boldsymbol{\nabla}p$. The subsequent dynamics of the post-shock interface evolution can be described by the vorticity equation. The thin vortex sheet along the interface induces a velocity field whose solenoidal component is given by the Biot-Savart law (Saffman, 1992; Cottet *et al.*, 2000). The subsequent evolution of this vortex sheet is obtained by following the trajectories of Lagrangian markers located along the sheet (Pozrikidis, 2011). In this section, we describe the problem set-up, the

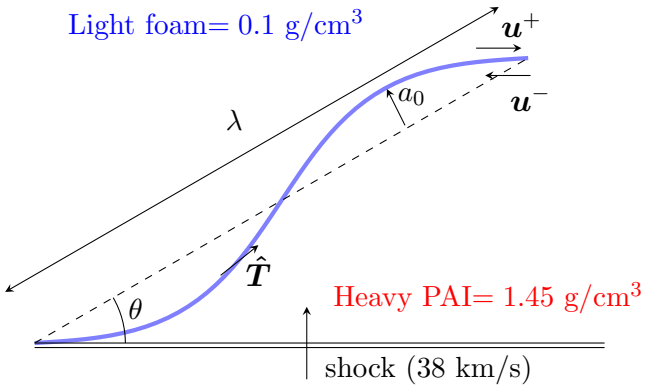

Figure 3.1: Problem set-up for the interaction of an oblique shock with a perturbed interface.

physical/numerical models, and the initial conditions.

3.3.1 Problem set-up

The problem set-up, shown in Fig. 3.1, is based on the experiments of Rasmus *et al.* (2018) and Rasmus *et al.* (2019), performed on the OMEGA-EP laser facility on a target composed of a layer of polyamide-imide (PAI of density 1.45 g/cm^3) next to a layer of foam (density 0.1 g/cm^3), resulting in a pre-shock Atwood number $A_{\text{pre}} \approx 0.87$. A shock wave travels from the heavy material into the light material, and interacts with a two-dimensional sinusoidal perturbation (wavelength $\lambda = 100$ μm, initial amplitude $a_0 = 0.1\lambda$) tilted by an angle $\theta = 30°$ with respect to the shock. The shock speed is approximately 38×10^3 m/s and the post-shock Atwood number is $A \approx 0.67$. We take our baseline case to be $\theta = 30°$ and investigate the dynamics as the tilt angle is varied between $0° \leq \theta \leq 50°$.

3.3.2 Vortex-sheet model

We start by performing a Helmholtz decomposition of the velocity field into solenoidal (rotational) and dilatational (irrotational) components. The equations governing the solenoidal component are solved using the vortex-sheet formulation described by Pozrikidis (2011). The high flow velocities in the experiments ($\sim 10^4$ m/s) result in high Reynolds numbers, such

that viscosity can be neglected. The effect of gravity is too weak at these time and length scales to play a significant role in the evolution of the interface. The equations governing the motion of the sheet and the numerical discretization are given in Sec. 2.4. As explained in Sec. 3.3.3, the dilatational velocity component is modeled using a factor accounting for shock compression and decompression due to laser-turn off, the latter represented by the third term in Eq. 2.32. Although investigations of similar problems have been conducted in the past (Sohn *et al.*, 2010; Sohn, 2011), the present study is the first report of highly resolved computations for oblique interfaces under HED conditions.

3.3.3 Deceleration and decompression due to laser turn-off

In the context of the problem under consideration, compressibility has two primary effects. First, velocity changes are accompanied by pressure changes, which give rise to density changes. Second, local flow changes are communicated to the rest of the domain at a finite speed (e.g., waves interacting with target boundaries), by contrast to incompressible flow where this information propagation speed is effectively infinite. Volumetric changes in the compressible component due to shock compression and laser turn-off are modeled by a decompression factor prescribed from corresponding one-dimensional simulations; a corresponding acceleration term must also be added to the vortex-sheet equation. With regard to transient wave propagation effects, experimental data do not suggest that such effects take place over the relevant observation time. Experimental data further indicates that the shock recedes from the interface at a higher velocity than the interface velocity such that shock proximity effects (Glendinning *et al.*, 2003) can be neglected.

Upon laser turn-off, a rarefaction is launched into the system, interacting with the interface at $t \approx 5$ ns, leading to decompression and deceleration of the interface (Rasmus *et al.*, 2019). Both effects result in modifications of the perturbation growth. The decompression is accompanied by a gradient of velocity across the interface, thus stretching the interface in the streamwise direction, while the deceleration causes a pressure gradient opposite to the

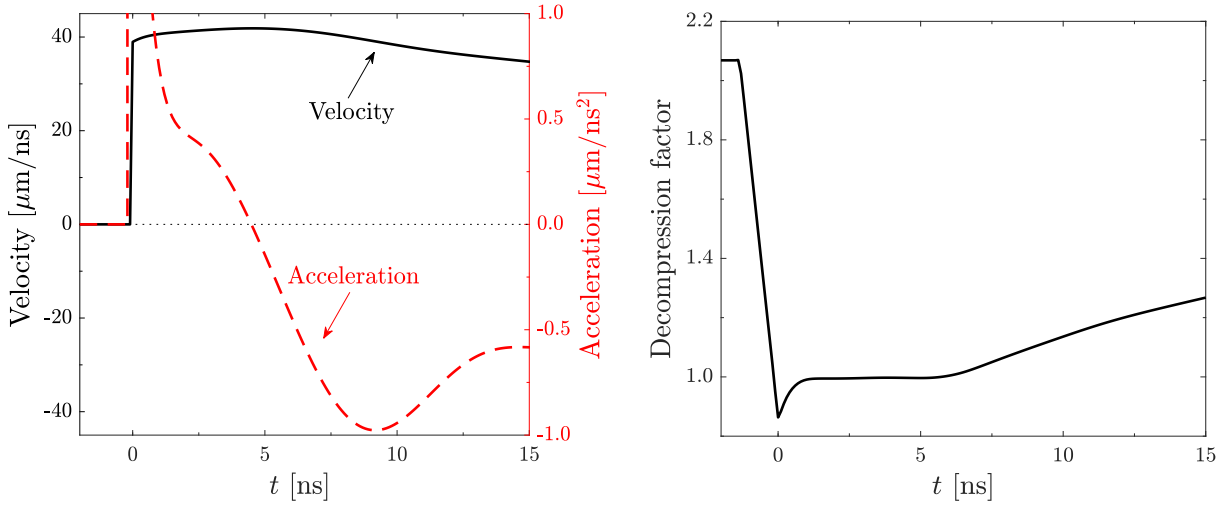

(a) Interface velocity and acceleration (b) Decompression factor

Figure 3.2: Time evolution of (a) the interface velocity and corresponding acceleration, and (b) the interface decompression factor from xRAGE simulations.

density gradient at the interface, such that the system is Rayleigh-Taylor unstable during the interaction with the rarefaction. This latter effect is represented by the third term on the right-hand-side of Eq. 2.32, and corresponds to a body force due to the non-inertial reference frame. The time-dependent acceleration profile $\boldsymbol{g}(t)$ is obtained from the interface velocity computed from one-dimensional simulations, using the radiation-hydrodynamics xRAGE code (Gittings *et al.*, 2008), as is shown in Fig. 3.2a. The time origin is taken to be when the shock reaches the interface, causing an impulsive interface velocity. Thereafter, the interface velocity increases slightly until $t \approx 5$ ns, after which it decreases, indicating the arrival of the rarefaction at the interface. Because of the heavy-to-light configuration, negative values of the acceleration give rise to the RT instability.

The effect of the interface decompression is taken into account by multiplying the perturbation amplitude by a decompression factor determined by the distance between two Lagrangian tracer particles relative to their distance before the arrival of the rarefaction. One tracer particle is located in the foam, while the other is located in the PAI material, each initially located 30 μm away from the interface. The position of each particle over time (y_{foam} and y_{PAI}) is obtained from 1D xRAGE simulations, such that the decompression

factor is given by

$$\left| \frac{y_{\text{foam}}(t) - y_{\text{PAI}}(t)}{(y_{\text{foam}} - y_{\text{PAI}})_{\text{post-refract}}} \right|, \tag{3.1}$$

where the "post-refract" subscript denotes the state after all waves produced during the refraction have crossed the tracer locations, as shown in Fig. 3.2b. Before the incident shock reaches the tracer particle in the PAI material ($t < 0$), the decompression factor is constant, as none of the particles have moved. After the shock has passed over the PAI particle, the decompression factor decreases, due to the positive velocity of the PAI particle and the fact that the shock has not yet reached the particle in the foam. As the shock interacts with the interface, a reflected rarefaction originates due to the heavy-to-light configuration, causing the particle in the PAI material to be accelerated towards the interface. During this time, there is also a transmitted shock propagating in the foam material, which reaches the tracer particle in the foam at $t \approx 0$ ns. As a result, this particle has a positive velocity, increasing the decompression factor after $t = 0$ ns. After the reflected rarefaction has passed over the particle in the PAI material ($t \approx 1$ ns), the decompression factor remains constant, and corresponds to the RT-stable phase. After $t \approx 5$ ns, the decompression factor increases, indicating the arrival of the rarefaction from laser turn-off.

Results with additional tracer particles initially located at ± 10 μm and ± 20 μm demonstrated that the decompression factor is not sensitive to the choice of initial tracer position (data not shown). The choice ± 30 μm is an example where the tracers are far enough from the interface that the mesh resolution at the interface is not an issue, but close enough to correctly represent the rarefaction conditions experienced by the interface structure.

Our approach to representing compressible phenomena has two main limitations. First, the acceleration $\boldsymbol{g}(t)$ and the decompression factor are prescribed from a 1D precursor simulation, rather than fully coupled to the 2D dynamics. Second, transient wave-propagation effects (e.g., reflections from boundaries) are ignored. We therefore expect the present approach to be applicable for nominally 1D base flows in geometries such that wave-propagation effects can be neglected, which are reasonable assumptions in the problem of interest.

3.3.4 Initial vortex-sheet strength distribution

The initial conditions consist of the shape of the interface and the corresponding distribution of the vortex-sheet strength along the interface immediately after the passage of the shock. Rasmus *et al.* (2019) showed that in the experiments the interface undergoes a marginal direct phase inversion, causing the interface to be compressed so strongly (by a factor of ∼20 of its original amplitude) that the post-shock shape of the interface can be considered flat.

We initialize the vortex-sheet strength distribution along the interface with the approach of Samtaney & Zabusky (1994), who showed that the circulation per unit length of the pre-shock interface is proportional, to first order, to the local angle between the incoming shock and the pre-shocked interface α as

$$\gamma \equiv \frac{d\Gamma}{ds} \approx \sigma \sin\alpha = \sigma \frac{dy}{ds}, \tag{3.2}$$

where σ is independent of the interface geometry but is a function of the material properties, the shock Mach number, and pressure ratios across the waves generated by the incident shock refraction at the interface. Note that the local angle α varies along the perturbed interface, whereas θ denotes the mean angle between the interface and the shock. The expression for σ provided by Samtaney & Zabusky (1994) is not valid under HED conditions given the exceedingly strong shock and the non-ideal gas equation of state. Instead, to determine σ, we use xRAGE to extract the total circulation Γ, as done by Rasmus *et al.* (2019), where a diagnostic box surrounding the post-shock flat interface is used to compute the total circulation. Integrating Eq. 3.2 directly with respect to the unit length of the pre-shock interface ds would not yield the amount of circulation obtained from xRAGE, due to the compression of the interface. After an appropriate change of variable (Rasmus *et al.*, 2019),

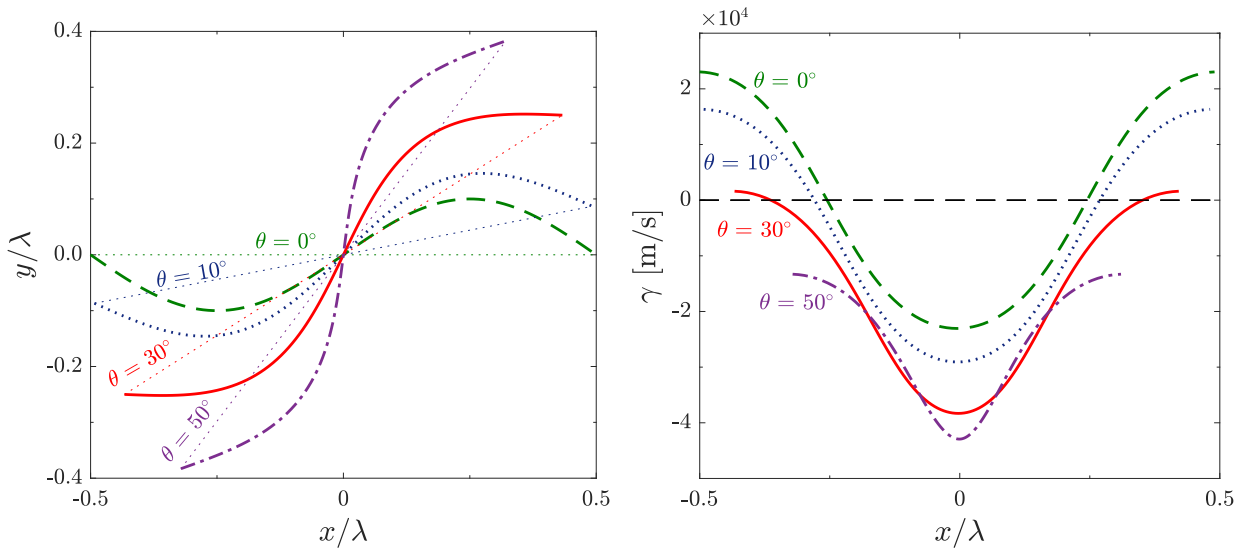

(a) Pre-shock interface

(b) Post-shock sheet-strength distribution

Figure 3.3: (a) Pre-shock interface and (b) corresponding post-shock sheet-strength distribution for $0° \leq \theta \leq 50°$. The red line represents the baseline case ($\theta = 30°$).

it can be shown that $\Gamma = \int \gamma dx$. For $\theta = 30°$ and $\lambda = 100$ μm, we obtain $\Gamma = 1.4$ m^2/s and

$$\sigma = \frac{\Gamma}{\int \frac{dy}{ds} dx} = 4.3 \times 10^4 \text{ m/s}. \tag{3.3}$$

Fig. 3.3 shows the initial conditions for different tilt angles up to the critical value $\theta = 50°$ for initial amplitude $a_0 = 0.1\lambda$. Beyond $\theta \gtrsim 50°$, part of the interface crosses the y-axis multiple times, in which case the assumption of a flat post-shock interface is not valid. In addition, higher-order terms need to be accounted for in Eq. 3.2 when the local angle α is too large. Such a scenario is beyond the scope of this study. In the case $\theta = 30°$, the sheet-strength distribution is mainly negative, with only minor positive values at the extremities. A closer inspection reveals that the sheet strength is entirely negative for a tilt angle $\theta \gtrsim 32°$. In our study of the role of the tilt angle in section 3.4.2, the largest negative value of the initial sheet-strength distribution γ_0, seen in Fig. 3.3b, is used as a characteristic velocity to non-dimensionalize the time variable as $\tilde{t} = \gamma_0 t/\lambda$. For a given value of $\tilde{t} = 3$, the corresponding physical time is given in table 3.1. We note that the perturbation in Fig. 3.3a is included for illustrative purposes; the present simulations are initialized with a flat interface and the

θ [°]	0	10	20	30	40	50
$\gamma_0 \times 10^4$ [m/s]	2.3	2.9	3.4	3.8	4.1	4.3
t [ns]	13	10	8.8	7.8	7.3	7.0

Table 3.1: Maximum magnitude of vortex-sheet strength γ_0 and corresponding physical time for different tilt angles and $\tilde{t} = 3$.

sheet-strength distributions in Fig. 3.3b.

3.4 Results and discussion

3.4.1 Dynamics of the baseline case

We first investigate the dynamics of our baseline case ($\theta = 30°$), including the role of interface deceleration and decompression due to laser turn-off. We also include, in Appendix B, a comparison to experiments and xRAGE simulations of the case $\theta = 0°$ (single-mode at normal incidence, i.e., RM instability (Di Stefano *et al.*, 2019)), which can be validated against existing well-established theory. The passage of the shock deposits vorticity along the interface, whose dynamics subsequently evolves according to the induced velocity field. Fig. 3.4 shows the post-shock time evolution of the interface and its associated sheet-strength distribution. The time evolution $t \leq 15$ ns corresponds to the experimental time range (Rasmus *et al.*, 2019). The width of each frame in Fig. 3.4a is $x/\lambda = 1$, but the post-shock interface wavelength corresponds to the effective wavelength $\lambda \cos\theta$, hence the extra space on the left and right of the interface.

As explained in the previous section and as supported by the experiments of Rasmus *et al.* (2019), the initial interface morphology is initialized as flat, with a mean sheet-strength distribution that is negative. This negative mean sheet strength indicates mean clockwise rotation. The location of the largest negative value of the sheet strength achieved over the course of the simulation is denoted by s_-, and initially coincides with $s = 0.5 s_N$. This point separates the interface into two parts: the part between the arclength of the first point and

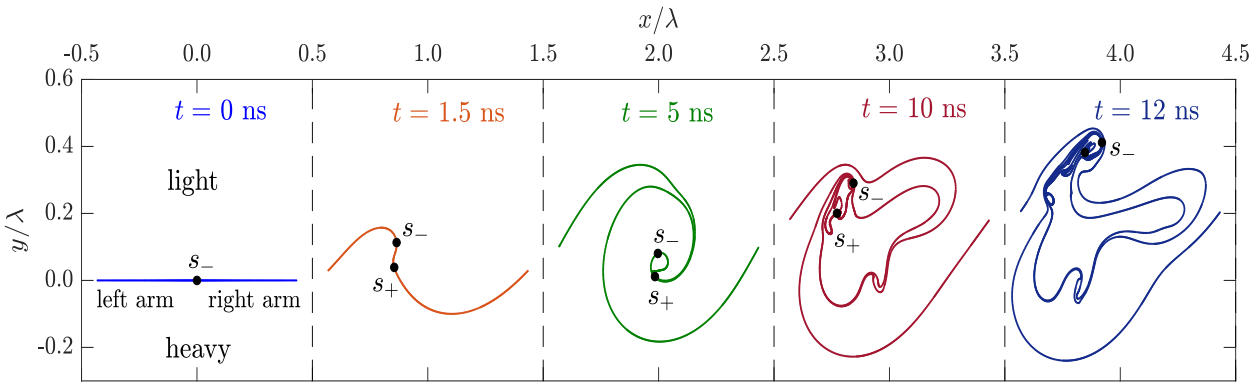

(a) Interface morphology

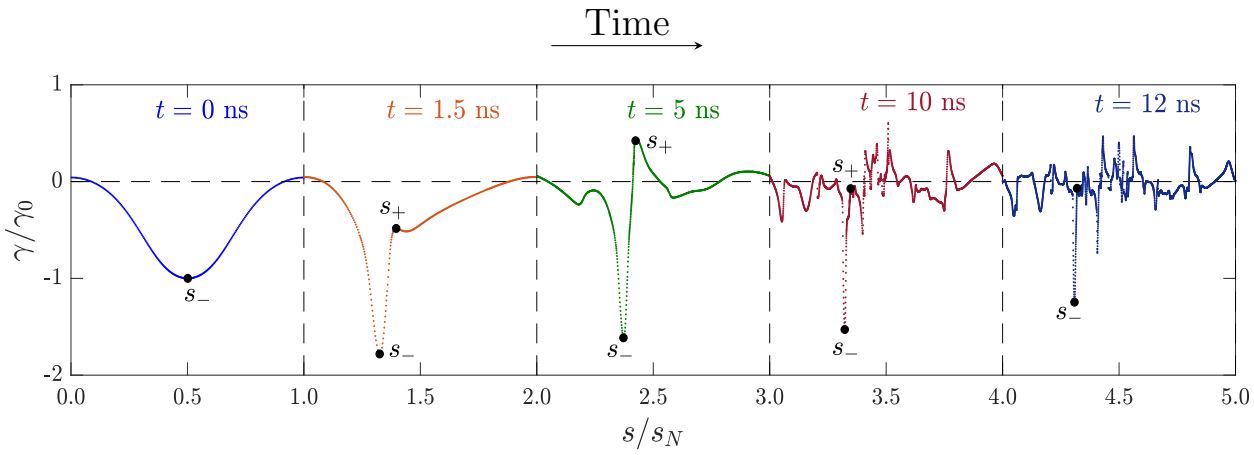

(b) Sheet-strength distribution

Figure 3.4: Time evolution of (a) the interface morphology, and (b) its associated sheet-strength distribution along the interface arclength normalized by the total length of the interface (arclength value of the last point s_N) for the baseline case ($\theta = 30°$).

s_- is referred to as the "left arm" of the interface, while the part between s_- and the last point is referred to as the "right arm" of the interface.

In the linear regime, the interface adopts a sinusoid-like shape (not shown for visualization purposes). The point s_- of the sheet-strength profile moves to the left and increases in magnitude, as the predominantly negative vorticity causes the left arm of the interface to rise and the right arm to sink. The point s_- is the point at which the average tangential component of the acceleration vanishes. The points on the left (right) of s_- have a positive (negative) average tangential acceleration, such that the points on each side of s_- move toward s_-, leading to an accumulation of vorticity near s_-. Heavy and light fluids start to penetrate each other.

By $t = 1.5$ ns, the perturbation amplitude is no longer small. The mean shear and mean negative vorticity cause the interface to start rolling up and become multivalued, i.e., for at least one x-coordinate along the interface there are two values of the corresponding y-coordinate. This first instance of a multivalued interface perturbation occurs along the right arm. Although gradually decreasing along the left arm, the rate of change of the sheet strength in s along the right arm changes abruptly at s_+ (inflection point), which eventually becomes the location of maximum positive strength.

After the interface has become multivalued, the perturbation rolls up, causing the interface to become multivalued along the left arm as well, and the crest to topple over, due to the large negative rotation at s_-. By $t = 5$ ns, the amount of heavy fluid separating the left and right arms on the rolled up side of the interface is vanishingly small, except for a blob near the vortex core. The roll-up has now a filament-like structure with the blob of primarily negative vorticity. At this time, the co-rotating vortex structure is evident. The centripetal acceleration causes the vorticity at s_+ to increase and eventually become positive (Peng *et al.*, 2003).

The large negative vorticity at and near s_- causes the blob to rotate with a local angular velocity, entraining some of the light fluid into the heavy fluid. As the blob rotates, its shape

changes, and eventually breaks down into smaller blobs, which themselves rotate with their own angular velocity. More filament-like structures form, and by $t = 10$ ns, the angular momentum associated with the original blob causes un upward velocity of the now broken-down blob. As the latter keeps on breaking down, by $t = 12$ ns, the upward velocity causes this region of broken blobs to separate itself from the main mixing region. At these late times, three-dimensional and diffusive effects may alter the behavior of the interface by reducing the angular momentum of the rotating blob, which are beyond the scope of this study.

The interface morphologies shown in Fig. 3.4 can be used to produce synthetic radiographs. Approximating the densities of the heavy and light sides of the parametrized interface as the post-shock densities reported by Rasmus *et al.* (2019), and modeling other properties of the radiograph, such as interface curvature (Di Stefano *et al.*, 2019), yields the synthetic radiographs in Fig. 3.5. The time evolution corresponds to the experiments (1 ns $\leq t \leq$ 11 ns) with increments of ≈ 1.32 ns. The result of this process is a blurring of the roll ups, thus making fine-scale filaments difficult to discern. In the experiments, the complicated structure of the roll-up at late times may seed smaller-scale 3D mixing, further blurring out the tips. This visualization demonstrates that blurry features observed in experimental radiographs could in fact be due to the finite resolution of the experimental diagnostics averaging out sub-pixel-scale flow dynamics, in addition to diffusion, as previously suggested (Haines *et al.*, 2014).

The above description of the time evolution of the vorticity distribution along the interface is important as it relates the interface morphology to the vorticity-dominated dynamics of the flow. Another important quantity is the time evolution of the mixing zone. Fig. 3.6 compares the time evolution of the perturbation amplitude obtained with the vortex-sheet model to the experiments of Rasmus *et al.* (2019). Error bars of ± 3 μm accounting for the uncertainty in the measured amplitude, and ± 0.5 ns accounting for the uncertainty in the shock timing are added. To distinguish between the effects of volumetric changes and (incompressible) Rayleigh-Taylor-induced growth produced when turning off the laser, four cases

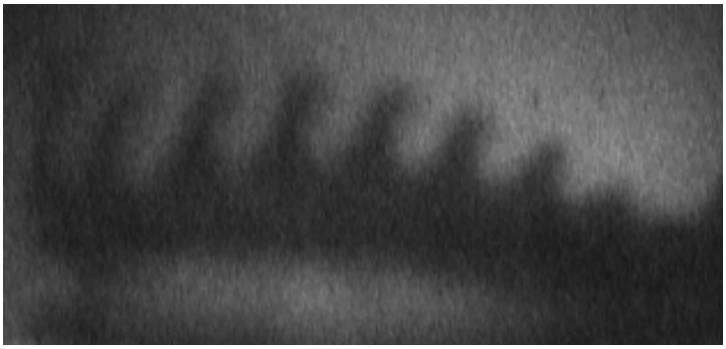

(a) Experimental radiograph

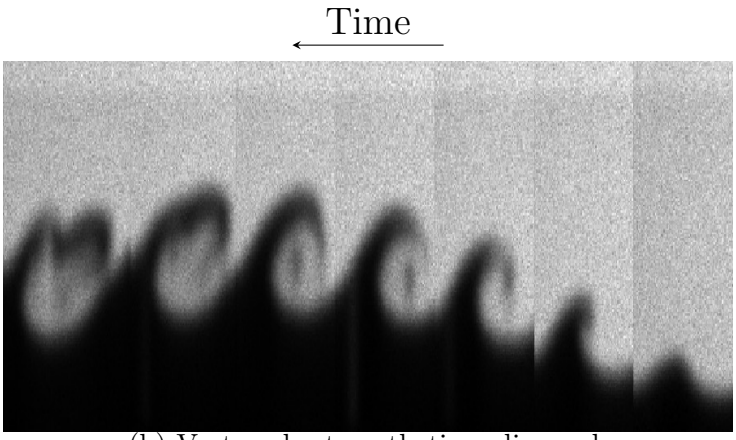

(b) Vortex-sheet synthetic radiograph

Figure 3.5: Roll-up morphology of the baseline case ($\theta = 30°$) from (a) the experiments (Rasmus *et al.* (2019)) (Reproduced from Rasmus, A. M. et al. "Shock-driven hydrodynamic instability of a sinusoidally perturbed, high-Atwood number, oblique interface." Physics of Plasmas 26.6 (2019): 062103, with the permission of AIP Publishing), and (b) reproduced synthetic image from vortex-sheet data.

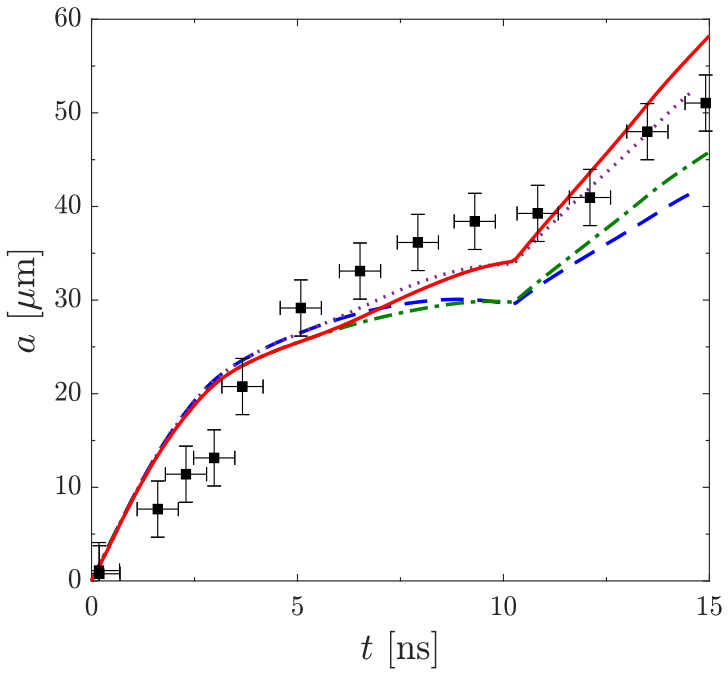

Figure 3.6: Time evolution of the perturbation amplitude obtained from the vortex sheet, without RT-acceleration or decompression (- - -), with RT-acceleration but without decompression (-·-·-), without RT-acceleration but with decompression (·····), with both RT-acceleration and decompression (—), and experiments (■).

are considered: the full dynamics, i.e., with RT-acceleration and decompression, the dynamics ignoring RT-acceleration, the dynamics ignoring the decompression, and the dynamics ignoring both the RT-acceleration and decompression. Until the arrival of the rarefaction at 5 ns, the four solutions are close to each other; the solutions ignoring the acceleration term show slightly more rapid growth due to the increase of the interface acceleration in the absence of the positive acceleration present until $t \approx 5$ ns. Until this point, decompression and baroclinic vorticity due to the mean acceleration field do not play a prominent role in the perturbation growth; growth is primarily dictated by the baroclinic vorticity due to the self-induced vortex-sheet acceleration and its elongation. Once the rarefaction reaches the interface, discrepancies between the different solutions become manifest. Both RT acceleration and decompression contribute to growth during this interaction, as evidenced by the fact that the solution ignoring these two effects shows the largest discrepancy with the experiments. Accounting for RT acceleration (but ignoring decompression) only affects the

growth at late times (after ~ 11 ns). For this problem, decompression plays a more prominent role in altering the perturbation amplitude growth starting at $t \approx 7$ ns. The late-time evolution of the perturbation growth is also altered by the above-mentioned upward velocity of the broken-down blob, resulting in a kink at $t \approx 10$ ns. This amplification of the growth is neither related to the RT acceleration nor to the decompression, since the solution ignoring these two effects exhibits the same behavior as well. Because of this growth amplification, the combination of RT acceleration and decompression produces a solution that slightly overpredicts the experimental results. The solution accounting for decompression (but ignoring RT acceleration) produces a solution closest to the experimental results. Discrepancies between the modeling and experimental results may be due to three-dimensional effects, the modeling of the decompression, equation-of-state effects, or diffusion effects.

3.4.2 Dependence of the dynamics on the tilt angle

Having related the interfacial dynamics to the vortex-sheet strength in the previous section, we now investigate the dependence of the interfacial dynamics on the tilt angle to understand the relative importance of impulsive acceleration vs. shear in the interface evolution. For simplicity, we neglect the effects of RT acceleration and interface decompression due to laser turn off. Upon inspection, the RT acceleration only has a minor effect on the roll-up morphology, and the interface decompression only scales the perturbation amplitude by the decompression factor.

3.4.2.1 Interface morphologies and vortex-sheet strength

As the tilt angle is increased, the pressure and density gradients become more misaligned, thus leading to an increased magnitude of the initial baroclinic torque. As confirmed by Fig. 3.3b, a larger tilt angle gives rise to a more skewed and narrow strength profile in the initial conditions. To perform a meaningful comparison when varying the tilt angle, we thus normalize time with the initial magnitude of the sheet strength γ_0, i.e., $\tilde{t} = \gamma_0 t/\lambda$. Figs.

3.7 and 3.8 show the time evolution of the interface morphology and its associated sheet strength until $\tilde{t} = 3$ for tilt angles between $0° \leq \theta \leq 50°$.

The case $\theta = 0°$ corresponds to the classical RM problem, which is characterized by the formation of counter-rotating vortices. The associated sheet-strength profile is initially symmetric with respect to the point s_0, which corresponds to the spike tip and point of zero vorticity; the interface remains symmetric about the vertical axis passing through this point and the sheet strength symmetric about this point. Tracking this point over time, the sheet strength is positive on the left of s_0, causing the interface to roll-up counterclockwise. On the right, the sheet strength is negative for the most part, eventually leading to clockwise roll up. This symmetry is sustained over time and leads to two peaks of equal and opposite strength, which correspond to the core of each counter-rotating vortices.

For $\theta = 10°$, the interface first forms a clockwise roll-up until $\tilde{t} \approx 1$ due to the non-zero (negative) mean sheet strength. The positive contributions to the initial baroclinic vorticity along the interface are thus smaller than the negative contributions, such that the interface rolls up in the clockwise direction. A consequence is that there is no longer a symmetry point like s_o. Eventually ($\tilde{t} \approx 2$) the sheet-strength on the left arm forms a positive peak, corresponding to a counterclockwise roll-up. This peak and physical size of the roll up are smaller in magnitude than those corresponding to the clockwise roll-up on the right arm. At the largest tilt angle under consideration ($\theta = 50°$), the initial sheet strength has a mean that is more negative than for lower tilt angles. Only co-rotating vortices develop and eventually form an intricate pattern as the vortices roll over.

Fig. 3.9 shows the time evolution of the mean value of the sheet-strength profile for the tilt angles under consideration. The mean value of the sheet strength physically corresponds to the bulk shear flow across the interface. Initially, the mean sheet-strength increases in magnitude with the tilt angle due to the initial increased shear with the latter. For $\theta = 0°$, which corresponds to pure RM, the mean sheet strength is zero throughout and there is no bulk shear across the interface. For $\theta > 0°$, as time progresses, the mean sheet strength

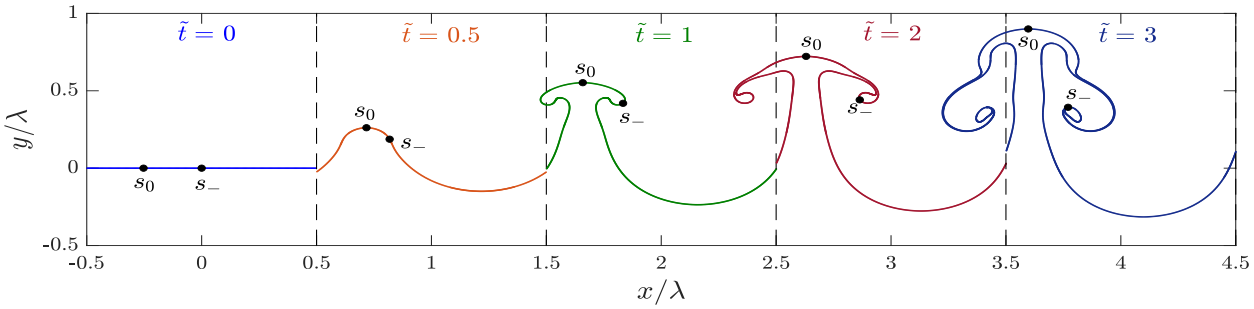

(a) $\theta = 0°$

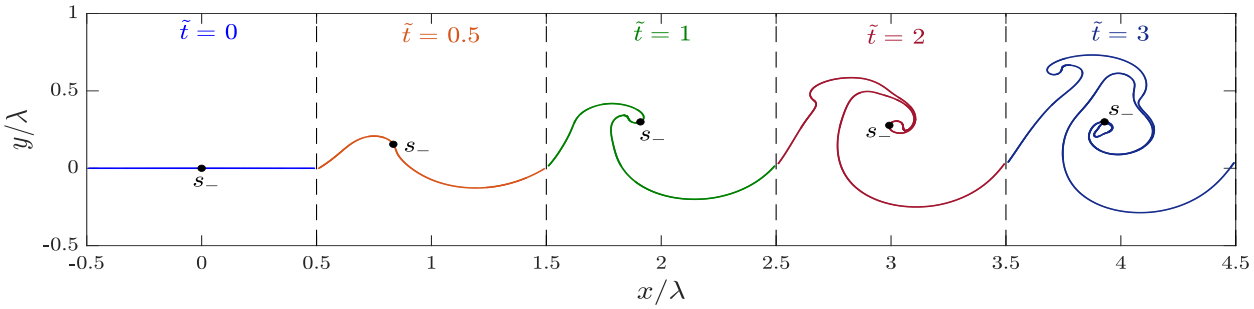

(b) $\theta = 10°$

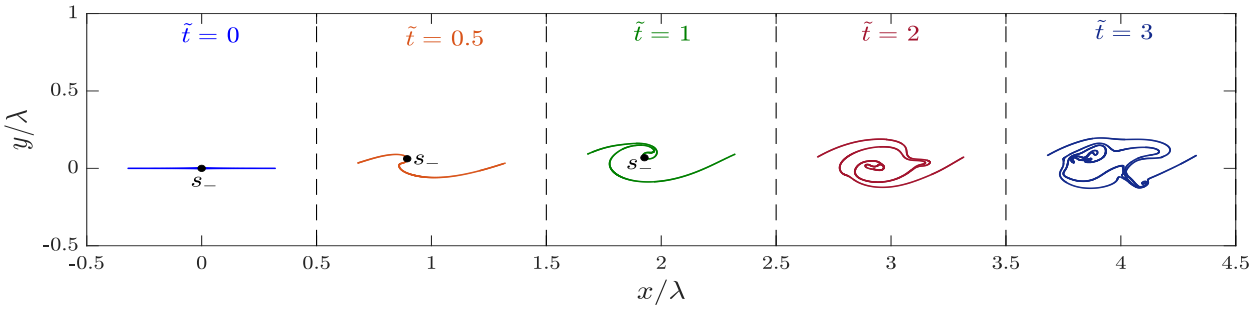

(c) $\theta = 50°$

Figure 3.7: Time evolution of the interface morphology for different tilt angles: (a) $\theta = 0°$ (RM), (b) $\theta = 10°$, (c) $\theta = 50°$. The left and right extremeties of the interface correspond to the effective wavelength $\lambda \cos\theta$.

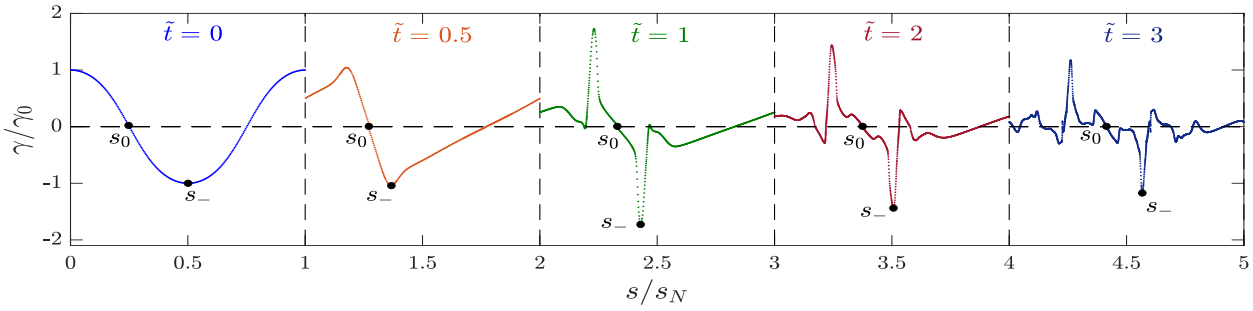

(a) $\theta = 0°$

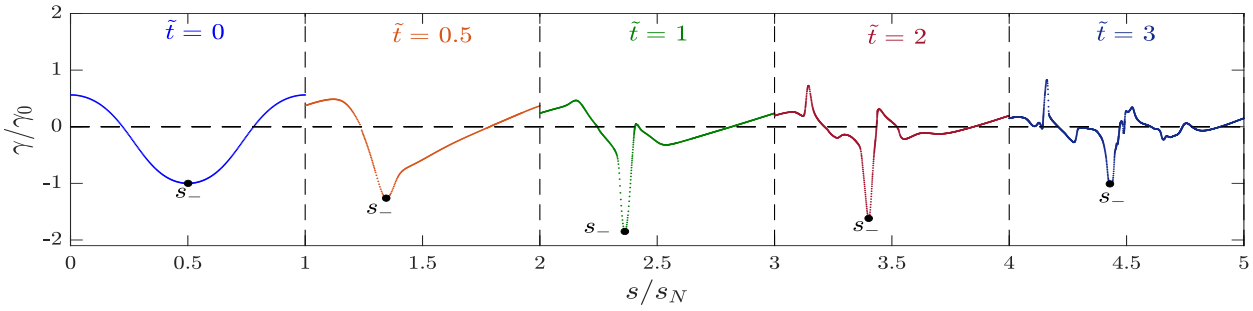

(b) $\theta = 10°$

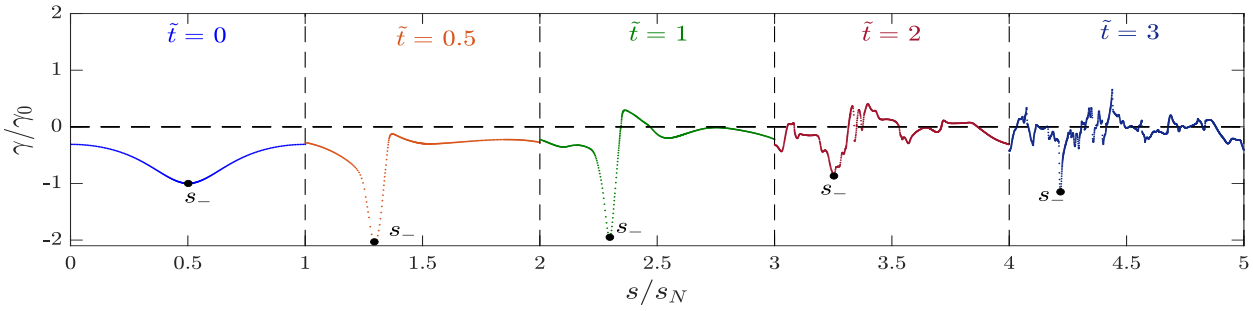

(c) $\theta = 50°$

Figure 3.8: Time evolution of the sheet-strength over the interface arclength for different tilt angles: (a) $\theta = 0°$ (RM), (b) $\theta = 10°$, (c) $\theta = 50°$. The arclength is normalized by the total length of the interface (arclength value of the last point s_N).

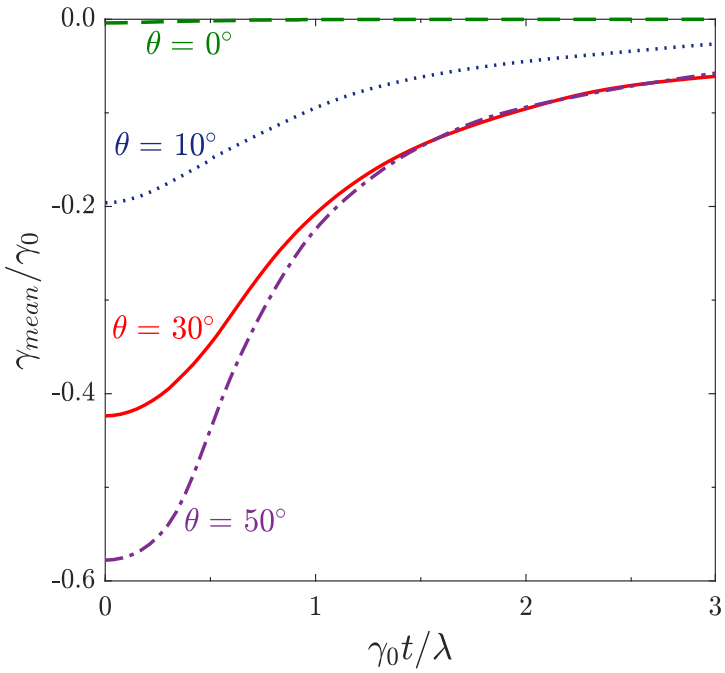

Figure 3.9: Time evolution of the mean sheet-strength value for different tilt angles.

becomes weaker and eventually reaches a non-zero asymptotic value, corresponding to a constant bulk shear flow. This reduction in magnitude of the sheet strength indicates that the amount of bulk shear decreases relative to its original value; the rate of decrease in strength magnitude is higher for higher tilt angles as the magnitude of the shear (characterized by a non-zero mean) is increased relative to that of the impulsive acceleration (characterized by the difference between the minimum and maximum of the initial distribution). The asymptotic value of the mean sheet strength increases with the tilt angle, except for $\theta = 30°$, which has a slightly larger value than that of $\theta = 50°$.

To better understand the role of shear vs. impulsive acceleration, Fig 3.10 shows the extrema of the sheet-strength profile with respect to its mean value for $0° \leq \theta \leq 50°$. Physically, the minimum sheet strength corresponds to the point of maximum vorticity in the flow (in magnitude) located at the vortex core, and is associated with the formation of the primary clockwise roll-up. Initially, the negative sheet strength amplitude relative to the mean increases (i.e., becomes more negative). This behavior is consistent with the observations of Rasmus *et al.* (2019), who showed that the mean value of the initial vorticity

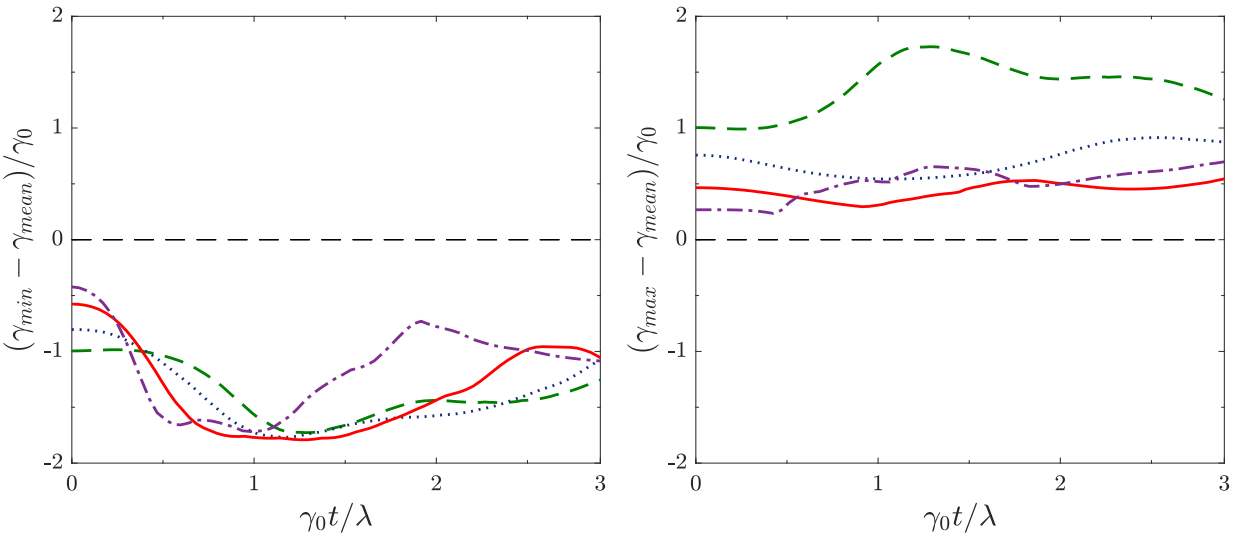

(a) Minimum sheet strength

(b) Maximum sheet strength

Figure 3.10: Time evolution of (a) the minimum and (b) the maximum sheet-strength with respect to its mean value for $\theta = 0°$ (- - -), $\theta = 10°$ (·····), $\theta = 30°$ (——), and $\theta = 50°$ (-·-·-).

profile becomes larger than the variations in the limit $\theta \to 90°$ (corresponding to pure KH). Eventually, each case reach a minimum in negative sheet strength, before decreasing in magnitude over time. This decrease is due to the development of opposite-sign vorticity associated with the centripetal acceleration of the roll-up, which cancels part of the primary vorticity. The maximum sheet-strength physically represents the point at which either a counterclockwise roll-up forms on the left arm, or opposite-sign vorticity develops. For $\theta = 0°$ and $10°$, the maximum sheet strength corresponds to the former and is located on the left of s_o, while for $\theta = 30°$ and $50°$, it corresponds to the latter and is located to the right of s_o. Note that for $\theta = 0°$, the evolution of the maximum and minimum relative strengths are the same due to the symmetry of the vorticity profile. Other than in the RM case, the largest negative strengths reach greater magnitudes than the maximum positive strengths. This preferential negative vorticity is a manifestation of the clockwise rotation imparted by the shear.

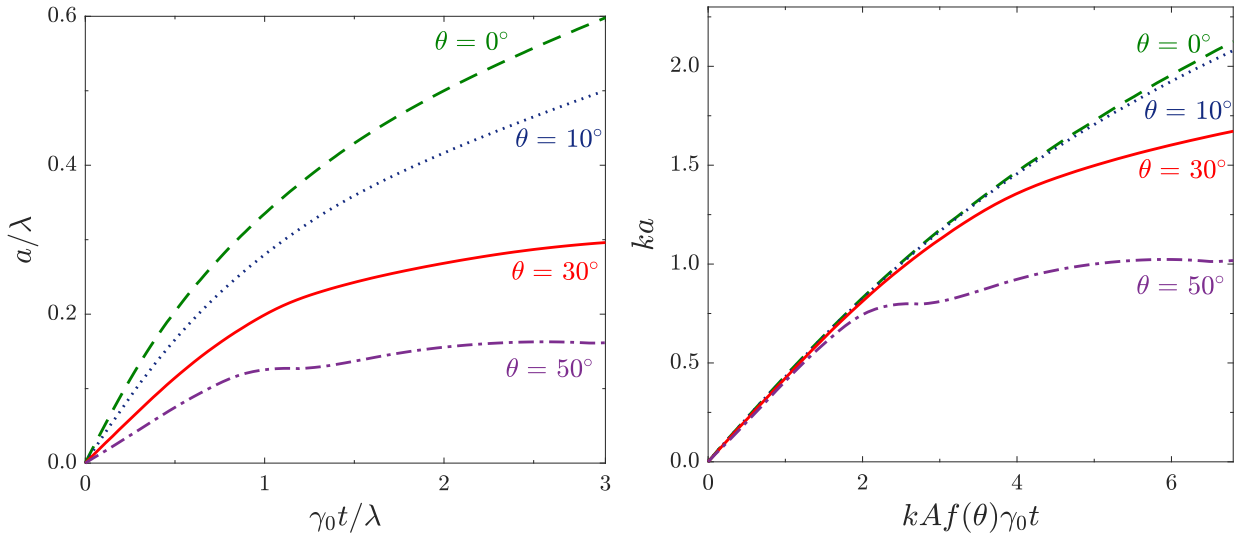

(a) Unscaled amplitude

(b) Scaled amplitude

Figure 3.11: Time evolution of the perturbation amplitude for different tilt angles when (a) unscaled, and (b) scaled using Eq. 3.10.

3.4.2.2 Early time scaling of the perturbation amplitude

When scaling time with the initial sheet strength, smaller perturbation growth is achieved over time with increasing tilt angle, as illustrated by Fig. 3.7. This behavior is quantitatively illustrated in Fig. 3.11, which shows the time evolution of the perturbation amplitude for $0° \leq \theta \leq 50°$. Here we investigate the early time growth of the perturbation and connect this behavior to the late time dynamics. Based on linear stability analysis of an oblique shock impinging upon a perturbed interface, Mikaelian (1994) found that the perturbation amplitude behaves as

$$\frac{a(t)}{a_0} = \cosh(\omega t) + 2\frac{\Delta V}{\Delta U}\frac{A}{\sqrt{1-A^2}}\sinh(\omega t), \tag{3.4}$$

where a_0 is the initial perturbation amplitude, ΔV is the change in the velocity normal to the interface from the shock, ΔU is the difference in shear velocity across the interface, and ω is the KH growth rate

$$\omega = \frac{k\Delta U}{2}\sqrt{1-A^2}. \tag{3.5}$$

In the linear regime, ωt is small enough that Eq. 3.4 may be linearized as

$$\frac{a(t)}{a_0} = 1 + kA\Delta V t, \tag{3.6}$$

thus indicating that the perturbation amplitude does not depend on the shear velocity ΔU at early times. In this case, the decrease of the amplitude with the tilt angle may be explained from the initial profile of the vorticity distribution along the interface. In the case $\theta = 0°$, the initial vorticity profile is symmetric with respect to s_0 (see first frame of Fig. 3.8a). When evaluated from the y-component of Eq. 2.31, the contributions of the vorticity profile to the integral, from the first point to s_-, double the velocity at the tip of the spike s_0. Additionally, the contributions from s_- to the last point cancel out. In the oblique case, however, the negative mean value of the vorticity profile leads to a lower tip velocity magnitude.

Eq. 3.6 suggests a scaling of the perturbation amplitude in time by $k\Delta V$. In practice, ΔV is obtained using the post-shock velocity of the interface, u^*. Both ΔU and ΔV can be written in terms of the corresponding projection along the tangential and normal directions to the interface: $\Delta U = u^* \sin\theta$ and $\Delta V = u^* \cos\theta$. If $\theta = 0°$ and if there is no interfacial perturbation, the velocity u^* is given by the solution to the one-dimensional Riemann problem. Therefore, Eq. 3.6 can be written as

$$\frac{a(t)}{a_0} = 1 + kA(u^* \cos\theta)t. \tag{3.7}$$

For our purposes, since the sheet-strength magnitude γ_0 is the characteristic velocity, it is convenient to replace u^* by γ_0. Recalling Eq. 3.2, the rotation matrix from the tilted frame of reference (τ, η) to the (x, y) coordinate system allows the sheet strength to be written as

$$\gamma = \sigma \frac{dy}{d\tau}\frac{d\tau}{ds} = \sigma(\sin\theta + ka\cos\theta\cos(k\tau))\frac{d\tau}{ds}. \tag{3.8}$$

The maximum magnitude of the sheet-strength γ_0 is located at $\tau = 0$. Upon inspection,

the term $d\tau/ds$ at $\tau = 0$ is close to unity for all tilt angles under consideration, with $(d\tau/ds)_{\tau=0} \approx 0.8$. Therefore, γ_0 can be written as

$$\gamma_0 \propto \sin\theta + ka\cos\theta. \tag{3.9}$$

As such, we propose the following scaling in time of the perturbation amplitude with the tilt angle

$$\frac{a(t)}{a_0} = 1 + kAf(\theta)\gamma_0 t, \tag{3.10}$$

where $f(\theta) = \cos\theta/(\sin\theta + ka\cos\theta)$. Fig. 3.11b shows the growth for the different tilt angles, with time scaled by $kAf(\theta)\gamma_0$. The curves collapse at early times, thus illustrating the dominance of the impulsive acceleration (and its geometrical decomposition into normal and tangential components) early on. Eventually, shear becomes important, such that a greater tilt (and hence stronger shear), leads to an earlier departure from this behavior. Our analysis confirms and extends the conclusion drawn by Rasmus *et al.* (2019) for the 30° case, namely that, for the HED problem under consideration, the instability is dominated at early times by RM, and at late times by shear. The effect of introducing a stronger shear is that the overall amplitude at late times is smaller, because part of the momentum drives the instability in the transverse direction, leading to a reduced growth, compared to pure RM driven by a momentum in the streamwise direction. As observed in Fig. 3.7, the structure becomes complex more rapidly, which could have ramifications for transition to turbulence.

3.4.3 Kinematics vs. dynamics

The roll-up behavior is affected by the flow dynamics, which are coupled to the kinematics (Eq. 2.31) through Eq. 2.32. Past studies of this problem (Rasmus *et al.*, 2019) assumed a constant sheet strength in time, thus effectively neglecting the dynamics. That study predicted that the roll-up develops symmetrically over time. As described in Sec. 3.3.2, the vortex-sheet dynamics are governed by two main mechanisms: baroclinic vorticity and

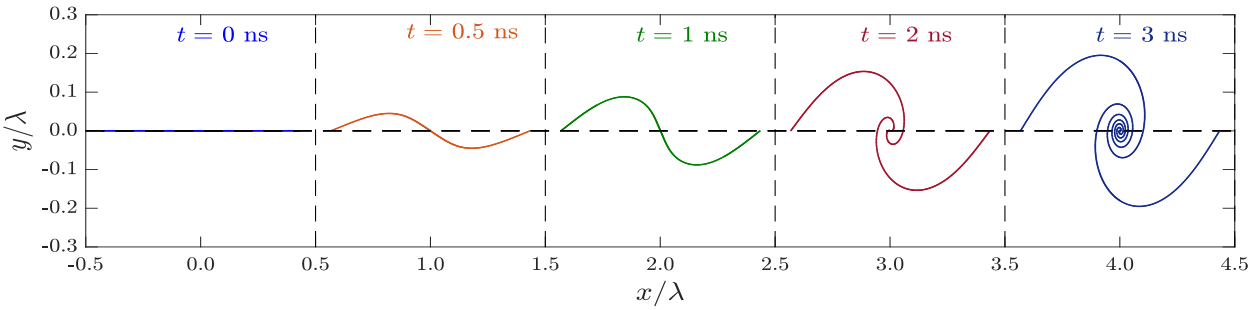

(a) Interface

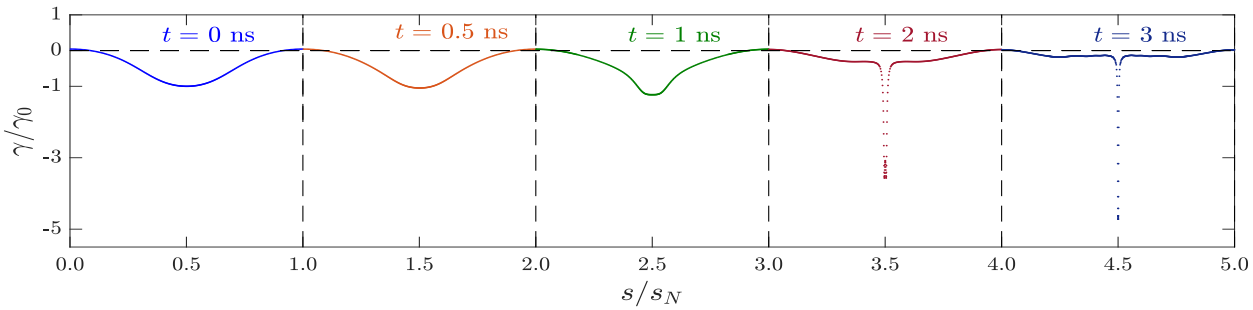

(b) Sheet strength

Figure 3.12: Time evolution of (a) the interface and (b) associated sheet-strength distribution for the baseline case ($\theta = 30°$) when solving the kinematics coupled with the dynamics assuming $A = 0$.

sheet elongation. The former is pre-multiplied by the Atwood number: assuming $A = 0$ effectively neglects generation of baroclinic vorticity, such that the sheet evolves according to its elongation only (fourth term on the right-hand-side of Eq. 2.32). As such, we expect that the asymmetry of the roll-up originates from non-zero Atwood number effects. To demonstrate this behavior, we consider the interface evolution and the corresponding sheet strength for the baseline case with $A = 0$ (Fig. 3.12) and kinematics only (Fig. 3.13), in comparison to the full model with finite Atwood number (Fig. 3.4). In the baseline case with $A = 0$, the interface rolls up symmetrically with respect to its vortex core and the sheet-strength profile stays symmetric with respect to the mid-arclength over time. The only source of sheet-strength evolution is due to sheet-elongation, leading to an amplification of the sheet-strength magnitude at the vortex-core. Based on this observation, we conclude that the asymmetry in the roll-ups originates from finite Atwood number effects, namely the acceleration terms, which generate vorticity. When considering the kinematics only, the

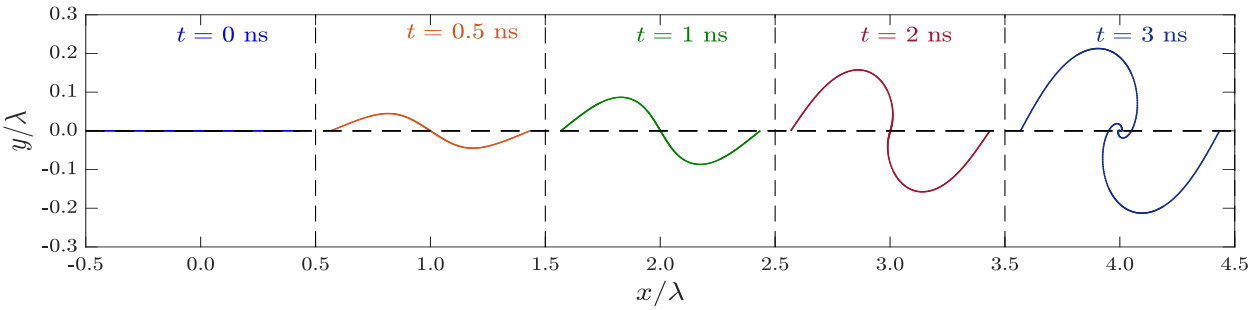

(a) Interface

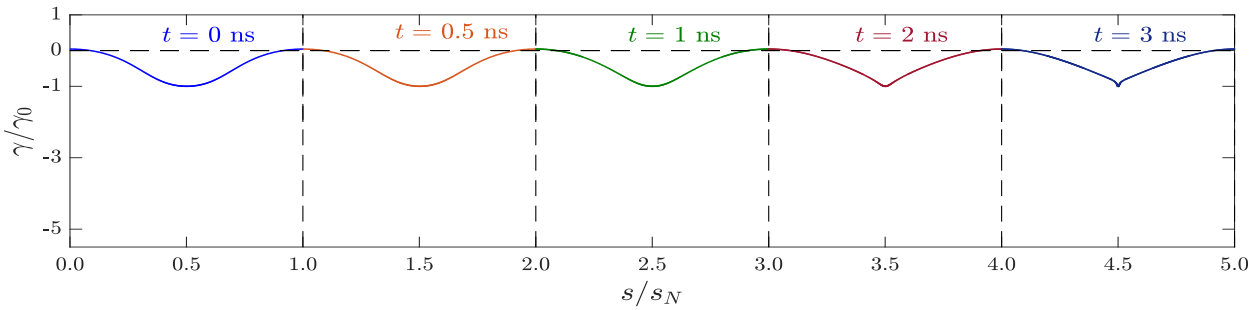

(b) Sheet strength

Figure 3.13: Time evolution of (a) the interface and (b) associated sheet-strength distribution for the baseline case ($\theta = 30°$) when solving the kinematics only.

interface also rolls up symmetrically with respect to its vortex core and the sheet-strength profile is symmetric. However, the sheet strength being independent of time, there is no sheet-strength magnitude amplification due to sheet-elongation. As a result, the interface does not roll up as much as in the $A = 0$ case. This approach prohibits vorticity generation of any kind. Note that the sheet strength at the Lagrangian points and the total circulation do not change over time; the apparent changes in the shape of the strength in Fig. 3.13b are due to the increasing arc length in the region of high vorticity.

3.5 Conclusions

In this work, we use a vortex-sheet model to investigate the interaction of an oblique shock with a perturbed interface in two dimensions under HED conditions. At early times, the pertubation growth is dominated by the impulsive acceleration of the shock (RM), as evidenced by our proposed scaling accounting for the normal and tangential components of the

shock. At later times, the perturbation growth is modulated by the positive and negative vorticity generated by the shear and the decompression due to the arrival of the rarefaction produced by laser turn-off. As the tilt angle is increased, the onset of the shear-dominated dynamics occurs earlier and becomes more pronounced. We further demonstrate how Atwood number effects break the symmetry in the flow. By appropriately prescribing the initial conditions, accounting for the body force corresponding to the accelerating reference frame, and incorporating the effect of decompression, reasonable agreement with experimental data is achieved.

Having shown the applicability of our vortex-sheet model to an instance of single-mode oblique-shock-driven interfacial instability, a possibility for further study is to investigate the role of the Atwood number on the perturbation growth. Another possibility is to investigate more complex interface structure, such as multimode initial perturbations (Di Stefano *et al.*, 2015*b*,*a*; Malamud *et al.*, 2013*a*), relevant in practice, and their vorticity dynamics. The key challenge with multimode studies is to prescribe an initial vortex-sheet strength distribution consistent with the initial interface morphology, which can be achieved using the model of Samtaney & Zabusky (1994). This approach would be applicable to sufficiently small-amplitude perturbations for which the superposition principle can be leveraged. However, for finite-size perturbations, other strategies must be devised.

CHAPTER 4

Vorticity Dynamics of the Late-Time Richtmyer-Meshkov Instability

This chapter is adapted from Pellone & Johnsen (2021)

4.1 Introduction

The Richtmyer–Meshkov (RM) instability occurs following the interaction of a shock wave with a perturbed interface separating fluids of different densities. These perturbations grow over time, possibly into a turbulent mixing region. This instability is of fundamental importance in inertial confinement fusion (Meezan *et al.*, 2013; Hicks *et al.*, 2012) and core-collapse supernovae (Abarzhi *et al.*, 2018; Kane *et al.*, 1997). The RM instability may also occur in combustion systems for high-speed aircrafts (Yang *et al.*, 1994*a*), and may play a role in diagnostic-ultrasound-induced lung hemorrhage (Patterson & Johnsen, 2018).

The interaction between the shock wave and the perturbed interface generates a baroclinic torque along the interface due to the misalignment of the pressure gradient across the shock, and the density gradient across the interface. Richtmyer (1960) first showed that the early linear stage of perturbation growth is characterized by a constant growth rate, which was later confirmed by the experiments of Meshkov (1969). In the non-linear stage of the growth, a bubble of light fluid "rises" into the heavy fluid, while a spike of heavy fluid "falls" into the light fluid. Eventually, the initially single-valued interface becomes multivalued and

rolls over, leading to the formation of roll-ups. Additional instabilities become important at later times. For instance, shear (i.e., Kelvin-Helmholtz (KH)) instabilities develop along the interface as it rolls up (Niederhaus & Jacobs, 2003; Morgan *et al.*, 2012; Vorobieff *et al.*, 2004). Additionally, the radial centripetal acceleration originating from the roll ups gives rise to a secondary baroclinic vorticity as the interface spirals inward (Peng *et al.*, 2003; Zabusky *et al.*, 2003; Lee *et al.*, 2006). As a result, unstable vortex bilayers may form and vortex projectiles may be ejected (Zabusky & Zeng, 1998; Zabusky & Zhang, 2002; Gupta *et al.*, 2003; Zhang & Zabusky, 2003; Wadas & Johnsen, 2020). If one considers the vorticity along an initially single-mode interface from a bubble to a spike, the vorticity is of just one sign just after the interaction. At some point in time during the formation of the roll-up, vorticity of the opposite sign is generated (Peng *et al.*, 2003), which gives rise to the formation of smaller-scale flow features possibly important as the flow transitions to turbulence. However, the mechanism responsible for generation of opposite-sign vorticity is currently unknown.

Late-time vorticity-induced effects on the flow dynamics of RM are not well understood, although observed in previous numerical and experimental investigations. Peng *et al.* (2003) observed that, due to the generation of opposite-sign vorticity, the asymptotic growth rate of RM is a positive constant, in contrast with previously predicted zero asymptotic growth rate (Sadot *et al.*, 1998; Zhang & Sohn, 1997*a*). Additionally, Morgan *et al.* (2012) experimentally measured that the RM bubble velocity increases at late times, indicating flow acceleration attributed to the growth of boundary layers. Bubble reacceleration is not exclusive to the RM instability, but has also been observed during the evolution of the Rayleigh-Taylor (RT) instability. For example, Ramaprabhu *et al.* (2006) and Ramaprabhu *et al.* (2012) showed that KH roll-ups form along the interface between the bubble and spike, causing the bubble to reaccelerate past the time of constant terminal velocity predicted by potential flow theories (Oron *et al.*, 2001; Goncharov, 2002).

The above studies suggest that the evolution of the vorticity between the bubble and spike plays a significant role in the flow behavior, yet scarcely documented and not well

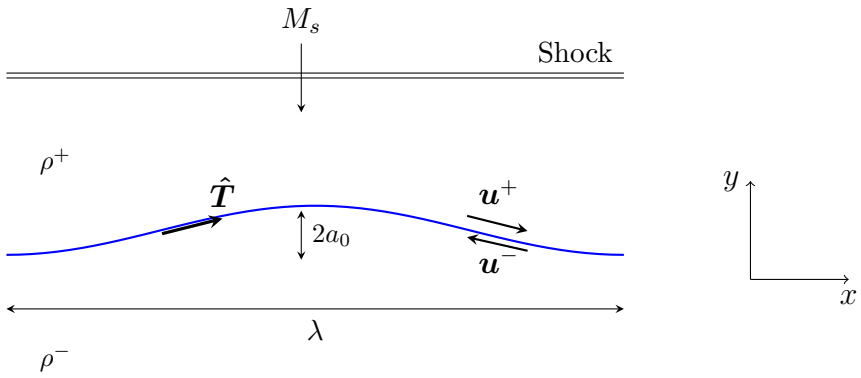

Figure 4.1: Problem set-up of the single-mode RM instability.

understood. Direct simulations and experiments typically focus on other quantities than vorticity (e.g., size of the mixing region, turbulent kinetic energy), and are unable to isolate the contributions of the vorticity-dominated dynamics in the evolution of the interface. Our objective is to explain the role of the vorticity dynamics in the evolution of a perturbed interface subjected to the RM instability. Our hypothesis is that, after the passage of the shock over the interface, the resulting vortex sheet can be described by the initial vorticity distribution between the bubble and spike. To understand the temporal and spatial evolution of this distribution, we use a vortex-sheet model, allowing us to isolate specific contributions to the vorticity evolution along the interface.

4.2 Problem set-up and methods

Fluids of density ρ^+ and ρ^- are adjacent to each other, separated by a sharp, nominally flat interface on top of which a perturbation $y_0(x) = a_0 \cos(kx)$ is superposed, where $k = 2\pi/\lambda$ is the wavenumber and λ is the wavelength. The pre-shock Atwood number is $A = (\rho^- - \rho^+)/(\rho^- + \rho^+)$. A shock of Mach number M_s is propagating in fluid ρ^+ at normal incidence to the interface, as illustrated in Fig. 4.1. The parameters governing the problem are the (normalized) initial amplitude, a_0/λ, the shock Mach number, M_s, and the Atwood number, A.

As a baseline, we consider the RM experiments of Collins & Jacobs (2002) performed

in a vertical shock tube consisting of an air layer ($\rho^+ = 1.351$ kg/m^3) next to a layer of SF_6 ($\rho^- = 5.494$ kg/m^3) at atmospheric pressure, and with corresponding ratio of specific heats, $\kappa_+ = 1.276$ and $\kappa_- = 1.093$. The incident shock ($M_s = 1.21$) propagates from air to SF_6, and meets a sinusoidal perturbation ($\lambda = 5.933$ cm, $a_0 = 0.03\lambda$). The Atwood number corresponding to the experiments is $A = 0.6053$. To investigate the role of the shock strength and density ratio on the vorticity dynamics, we consider Mach numbers in the range $1.21 \leq M_s \leq 5$, and Atwood number between $0 \leq A \leq 0.8$. The wavelength λ and the speed of sound in air, $c \approx 307$ m/s, are chosen as characteristic length and velocity to define the non-dimensional time $\tilde{t} = t/(\lambda/c)$.

As the shock traverses the interface, a layer of vorticity is generated along the interface due to the baroclinic torque originating from the misalignment of the pressure and density gradients. Diffusive effects are negligible over the time scales under consideration, so for an initially sharp interface this layer is a vortex sheet, i.e., a surface with zero thickness. In the context of the experiments of Collins & Jacobs (2002), the flow evolution on each side of the interface after shock passage can be considered incompressible (Brouillette, 2002). As a result, the vorticity equation can be reduced to the evolution of a vortex sheet governed by

$$\frac{d\gamma}{dt} = \underbrace{-2A\frac{d\boldsymbol{u}^{\mathrm{vs}}}{dt}\cdot\hat{\boldsymbol{T}}}_{\mathcal{T}_1} \underbrace{-\frac{A}{4}\frac{\partial\gamma^2}{\partial s}}_{\mathcal{T}_2} \underbrace{-\gamma\frac{\partial\boldsymbol{u}^{\mathrm{vs}}}{\partial s}\cdot\hat{\boldsymbol{T}}}_{\mathcal{T}_3}, \tag{4.1}$$

where the right-hand side of Eq. 4.1 consists of three terms: the first term ($\mathcal{T}_1$) represents the acceleration of the sheet in the tangential direction due to the self-induced motion of the sheet, the second term ($\mathcal{T}_2$) represents nonlinear advection of vorticity along the sheet, and the third term ($\mathcal{T}_3$) is related to the rate of change of the surface area in the direction of $\hat{\boldsymbol{T}}$. As evidenced by the Atwood number, the first two terms account for baroclinic vorticity production.

To initialize our vortex-sheet calculations, the morphology of the interface immediately after shock passage and the corresponding sheet-strength distribution along the interface

M_s \ A	0	0.2	0.4	**0.6053**	0.8
1.21	2	32	61	**88**	118
2				250	
3				368	
4				471	
5				573	

Table 4.1: Values of σ_1 [m/s] for different incident shock Mach numbers and Atwood numbers. The bold font corresponds to our baseline case from Collins & Jacobs (2002).

must be specified. In this work, the pre-shock perturbation amplitude is considered small compared to its wavelength, i.e., $ka_0 \ll 1$, such that the time the shock takes to traverse the interface is small compared to the post-shock evolution of the interface; it is thus reasonable to expect the interface morphology not to change. Furthermore, the incident shock travels from a light fluid to a heavy fluid, such that no phase inversion occurs. Therefore, the post-shock interface is assumed to be the same as the pre-shock interface. The sheet-strength distribution along the interface after shock passage is obtained from the model of Samtaney & Zabusky (1994):

$$\frac{d\Gamma}{ds} = \sigma_1 \sin\theta + \mathcal{O}(\sin^3\theta), \tag{4.2}$$

where θ is the local angle between the incident shock and the interface, and σ_1 is given by Eq. 2.45. Table 4.1 gives the values of σ_1 for the incident shock Mach numbers and Atwood numbers under consideration. The resulting sheet-strength distributions are shown in Fig. 4.2.

In addition to vortex sheet modeling, we conduct direct simulations of the multispecies Euler equations using a high-order accurate, discontinuous Galerkin method (Henry de Frahan *et al.* (2015*b*)). The scheme is fifth-order accurate in space and fourth-order in time. The code has been validated against Richtmyer-Meshkov experiments.

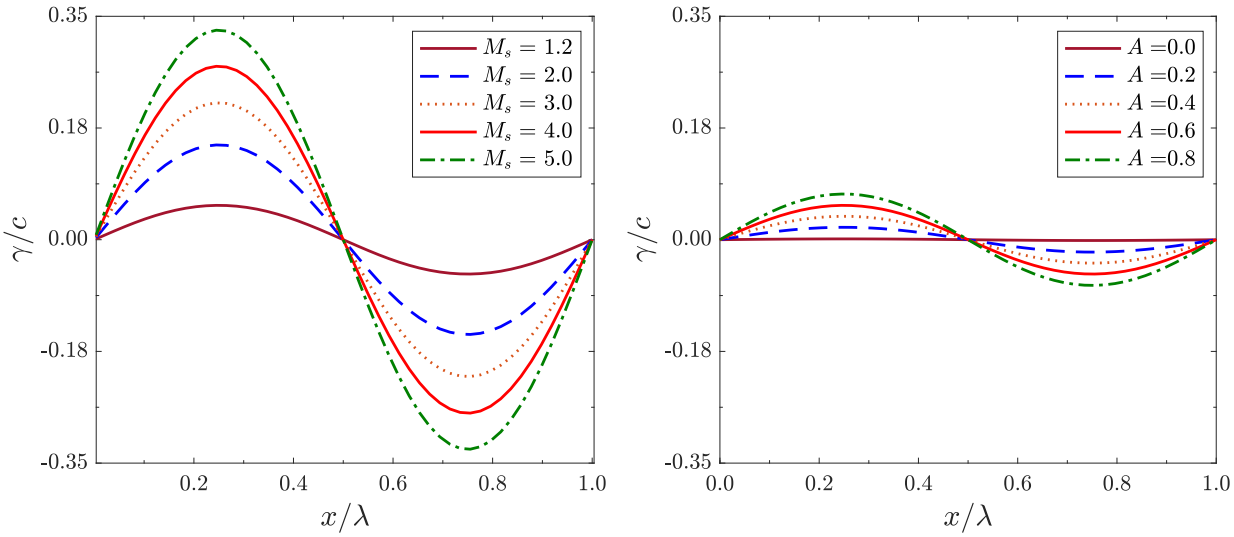

(a) Mach number dependence of the sheet strength.

(b) Atwood number dependence of the sheet strength.

Figure 4.2: Initial sheet-strength distribution along the interface for different shock Mach numbers with $A = 0.6053$ and Atwood numbers with incident shock Mach number $M_s = 1.21$. The red solid line corresponds to the baseline case.

4.3 Vorticity dynamics of the baseline case

We first describe the vorticity dynamics corresponding to the baseline case ($M_s = 1.21$ and $A = 0.6053$). Fig. 4.3 shows the time evolution of the interface and its corresponding sheet-strength distribution. Initially, the sheet strength is distributed sinusoidally along the interface, with positive values on the left of the spike (left half of domain) and negative values on the right of the spike (right half of domain). As the perturbation grows, the spike of heavy fluid penetrates the light fluid at a faster rate than the bubble of light fluid penetrates the heavy fluid. Given the positive Atwood number, the points located near the spike have a higher velocity magnitude than those located near the bubble. At $\tilde{t} \approx 11$, the combination of this higher velocity with the positive torque causes the perturbation height near the spike $y_s(x,t)$ to become multivalued. The time at which the interface becomes multivalued is referred to as the multivalue time t_m (Zabusky *et al.*, 2003; Peng *et al.*, 2003). The sheet strength profile steepens on the left and right of the spike. The arclength corresponding to the

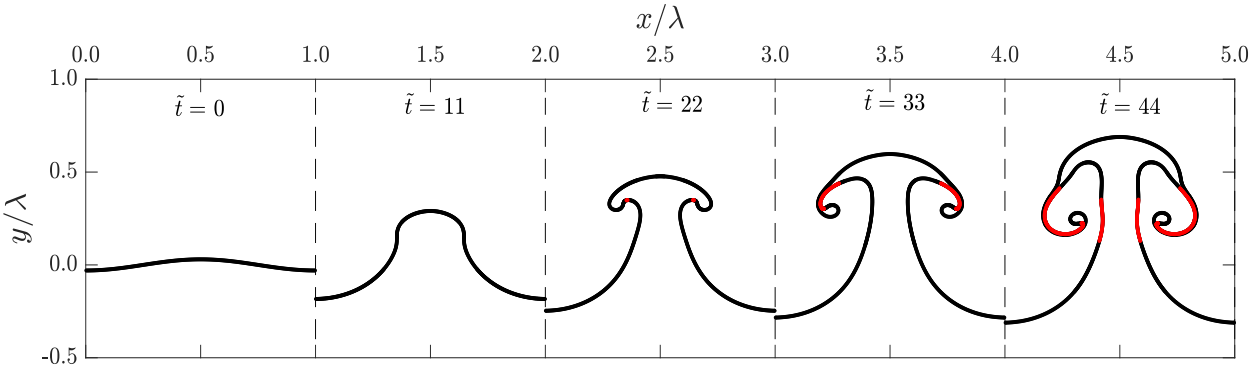

(a) Interface morphology

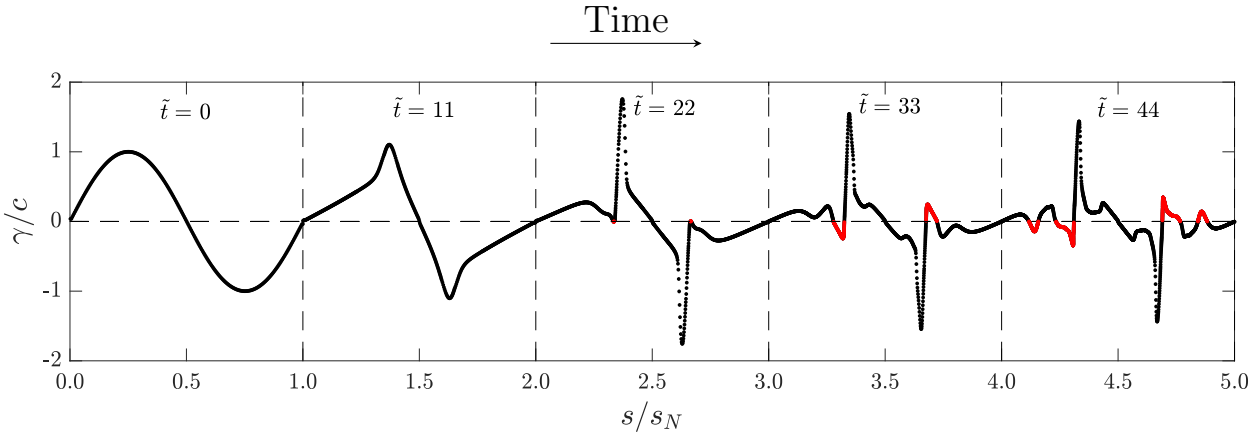

(b) Sheet-strength distribution

Figure 4.3: Time evolution of (a) the interface and (b) the corresponding sheet-strength distribution for the baseline case ($M_s = 1.21$ and $A = 0.6053$). The arclength is normalized by the sheet length. The interface and sheet strength colored in red show the development of opposite-sign vorticity.

maximum and minimum sheet strength is shifted toward the spike arclength ($s = 1.5s_N$) due to the advection of vorticity in the direction of the spike. By $\tilde{t} \approx 22$, part of the sheet strength in the left-half domain (initially positive) becomes negative, while part of the sheet strength in the right-half domain (initially negative) becomes positive, and is illustrated by red points in Fig. 4.3. We refer to the onset of this emergence of vorticity of the opposite sign as the onset time t_{on}. At that time, a counter-clockwise (respectively, clockwise) roll-up forms on the left-half (respectively, right-half) domain. After the onset time, this opposite-sign vorticity becomes more prominent, as shown by the increase (in magnitude) of negative (respectively, positive) sheet strength on the left-half (respectively, right-half) domain at $t \approx 33$. Each roll-up has now a filament-like structure, and opposite-sign vorticity spreads along the arms of the interface, from the inside of the roll-up toward the neck of the interface. Eventually, as the interface on each side of the spike continues to roll up, opposite-sign vorticity also appears along the neck of the interface, as seen at $t \approx 44$. This second instance of emergence of opposite-sign vorticity causes additional initially-positive (respectively, initially-negative) strength to become negative (respectively, positive).

To validate our vortex-sheet model, Fig. 4.4 compares the time evolution of the perturbation amplitude from the vortex-sheet model with the experiments of Collins & Jacobs (2002), the direct simulations, and the linear theory (Eq. 1.3). The results obtained with the current vortex-sheet model agrees well with the linear theory, and good agreement is achieved throughout the time range of the experiments.

To quantify the development of opposite-sign vorticity along the interface, we consider the amount of opposite-sign circulation generated after the onset time. Choosing the left-half of the interface to compute the circulation from the sheet strength (i.e., $\Gamma = \int \gamma ds$), the total circulation Γ can be decomposed as

$$\Gamma = \Gamma^+ + \Gamma^-, \tag{4.3}$$

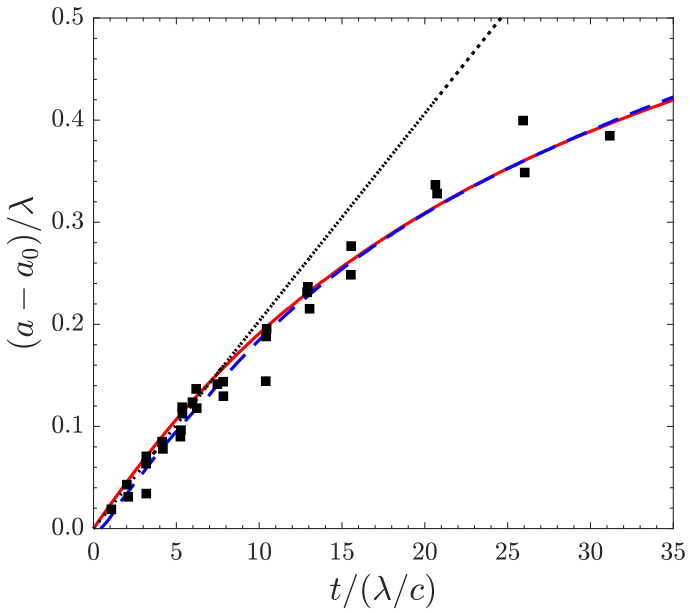

Figure 4.4: Time evolution of the perturbation amplitude for the experiments of Collins & Jacobs (2002) (■), the linear theory (·····), the direct simulations (- - -), and the vortex-sheet model (——).

where Γ^+ is the circulation of the original sign (positive in this case), and Γ^- is the circulation of the opposite sign. Fig. 4.5 shows the time evolution of the total circulation, the original-sign (positive) circulation, and the opposite-sign circulation. Since our vortex-sheet simulations are initialized immediately after the shock has deposited vorticity along the interface, the circulation is initially non-zero. During the linear phase of the perturbation growth, the sheet strength decreases, causing a slight decrease in the total circulation until $\tilde{t} \approx 6$. The total circulation then increases as the interface becomes multivalued and the roll-up forms. Before circulation of the opposite-sign develops, i.e., before the onset time, both the total circulation and the original-sign circulation coincide, while the opposite-sign circulation is zero. At the onset time, $\tilde{t} \approx 22$, the total circulation and original-sign circulation no longer coincide due to generation of opposite-sign vorticity. Opposite-sign circulation thus starts to increase (in magnitude), causing the total circulation to eventually decrease, at $\tilde{t} \approx 34$, due to negative contributions to the overall circulation.

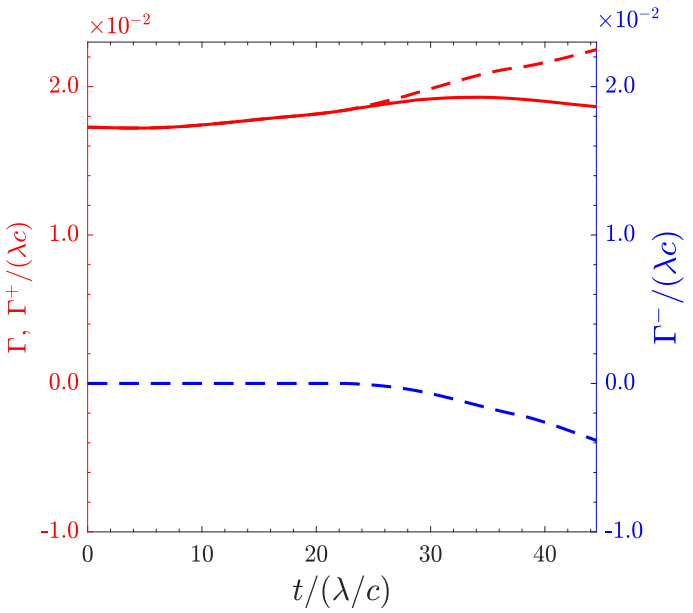

Figure 4.5: Time evolution of the total circulation Γ (—), circulation of the original sign Γ^+ (- - -), and circulation of the opposite sign Γ^- (- - -) over the left-half of the interface for the baseline case ($M_s = 1.21$ and A=0.6053).

4.4 Opposite-sign vorticity generation

In this section, we investigate the mechanisms leading to generation of opposite-sign vorticity. We start by considering the case $A = 0$, such that only the term $\mathcal{T}_3$ governs the time evolution of the sheet strength. To understand the effect of the two other terms, we then investigate the generation of opposite-sign vorticity for finite but small Atwood numbers. Because the multivalue time t_m is a characteristic time in the evolution of the interface, we choose to non-dimensionalize time with t_m in this section.

4.4.1 Vorticity dynamics for $A = 0$

4.4.1.1 General behavior

As shown in Sec. 4.6, opposite-sign vorticity does not develop when the Atwood number is zero. Nevertheless, we consider the zero-Atwood-number case (with $M_s = 1.21$) to understand the role of the term $\mathcal{T}_3$ in the evolution of the sheet strength. Term $\mathcal{T}_3$ accounts for

changes in the sheet strength due to the expansion and contraction of the interface. Fig. 4.6 shows the time evolution of the interface over half a wavelength, along with the corresponding sheet strength and $\mathcal{T}_3/\gamma$ distributions, and Fig. 4.7 shows the x- and y-velocity of the points along the interface. For visualization purposes, we substitute a Lagrangian parameter α for the arclength s, such that the sheet strength, $\mathcal{T}_3/\gamma$, and the x- and y-velocities are shown with respect to α. Based on the definition of $\mathcal{T}_3$, negative (positive) values represent an expansion (contraction) of the interface.

Initially, the sheet strength is positive due to the positive baroclinic vorticity generated on this side of the interface, leading to the counter-clockwise rotation of the interface observed at later times. The vortex core (VC) corresponds to the point of maximum sheet strength over the course of the simulation, and is represented by a red star. The x-velocity (respectively, y-velocity) is positive (respectively, negative) on the left of VC and negative (respectively, positive) on the right of VC, such that points on either side of VC move toward the vertical axis passing through VC. However, since the perturbation amplitude is initially small compared to its wavelength, the x-velocity is small compared to the y-velocity. As a result, the motion of the interface is initially almost entirely in the streamwise (vertical) direction, which causes the interface to expand, as illustrated by the negative value of $\mathcal{T}_3/\gamma$. Since $A = 0$, the x- and y-velocity is equal and opposite on either side of VC, such that the points trajectory on either side of VC is symmetric with respect to VC.

At $t = 0.5t_m$, the x-velocity increases (in magnitude) on either side of VC, and has larger values at points farther away from VC than near VC. As a result, the rate of change of the x-velocity along the interface, $\partial v_x/\partial\alpha$, increases (becomes more negative) at points near VC, causing $\mathcal{T}_3/\gamma$ to become positive. The interface near VC therefore starts to contract. Meanwhile, at points near the left and right extremity of the interface, $\partial v_x/\partial\alpha$ also increases but with the opposite sign (becomes more positive). The interface in that region therefore further expands, causing $\mathcal{T}_3/\gamma$ to become more negative. As a result, the sheet strength slightly increases at points near VC but slightly decreases at points farther away from VC.

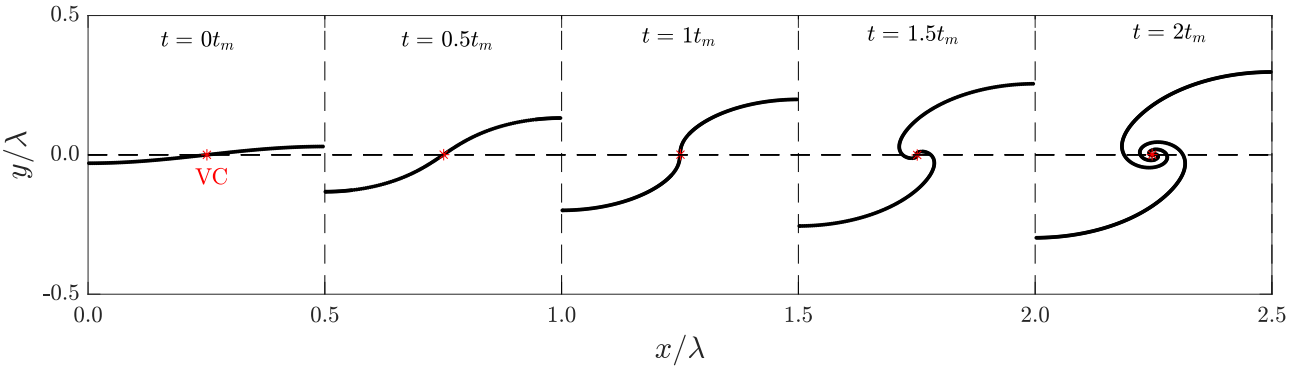

(a) Interface morphology.

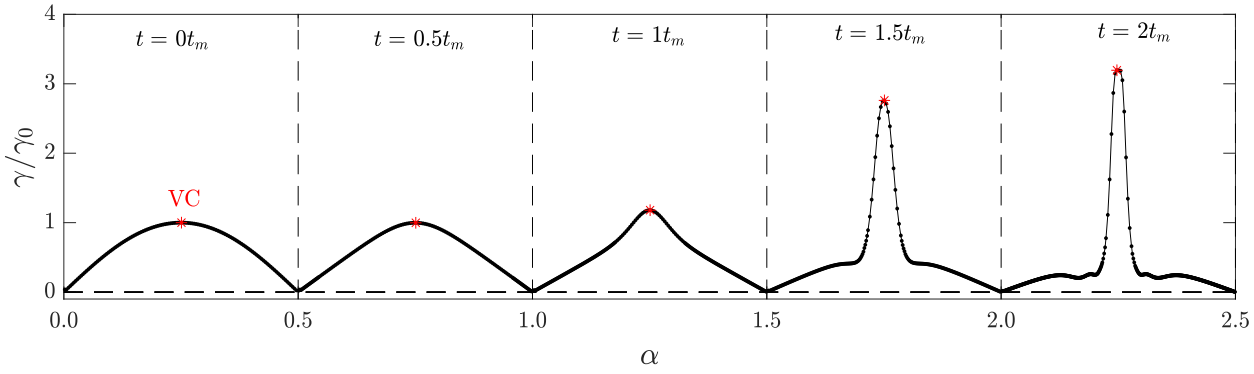

(b) Sheet-strength distribution.

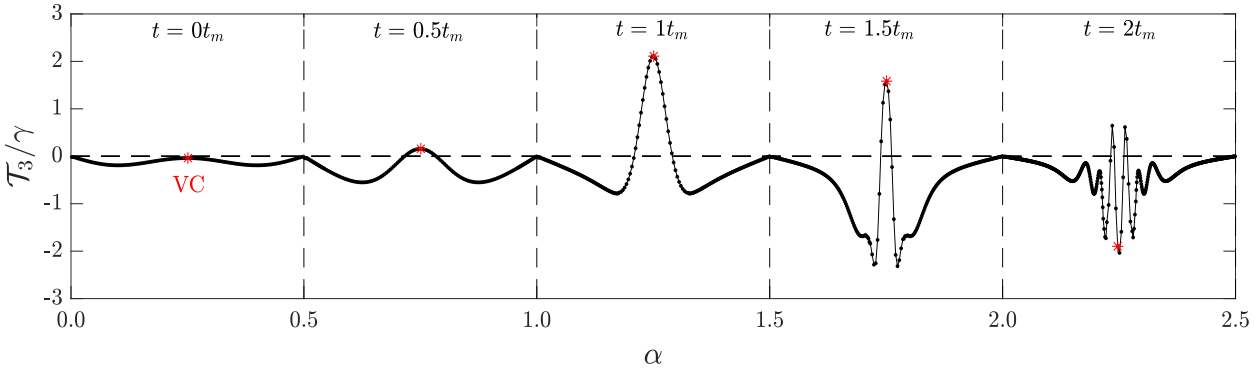

(c) $\mathcal{T}_3/\gamma$.

Figure 4.6: Time evolution of (a) the interface, (b) the corresponding sheet-strength distribution, and (c) the corresponding $\mathcal{T}_3/\gamma$ distribution for $A = 0$. In each time frame, quantities are plotted over one-half wavelength. The variable α is a Lagrangian parameter.

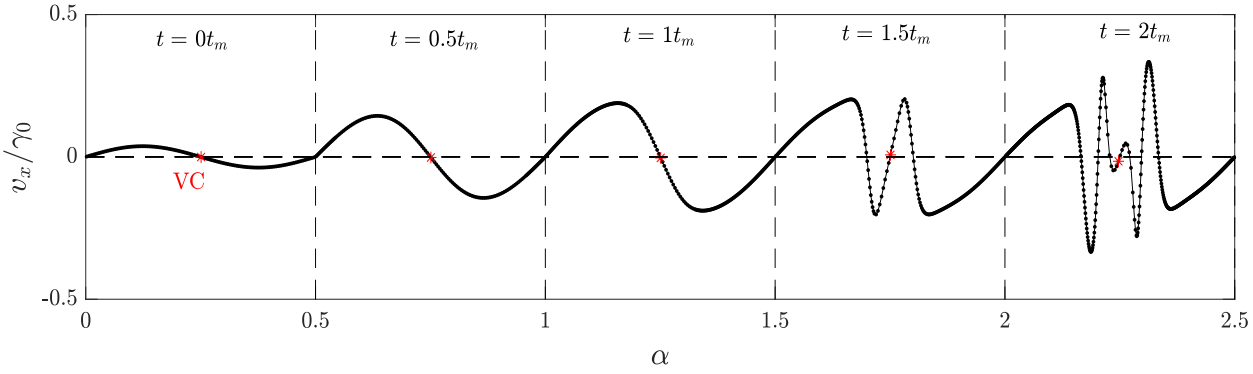

(a) x-velocity.

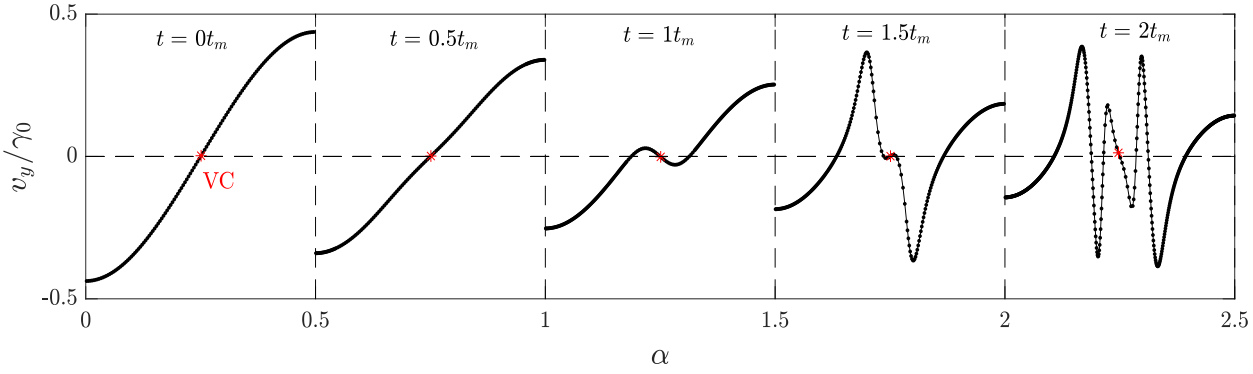

(b) y-velocity.

Figure 4.7: Time evolution of (a) the x-velocity, (b) the y-velocity for $A = 0$. In each time frame, quantities are plotted over one-half wavelength. The variable α is a Lagrangian parameter.

At the multivalue time ($t = t_m$), the initially-negative y-velocity at points near VC (on the left side) becomes positive, while the initially-positive y-velocity at points near VC (on the right side) becomes negative. This change in the sign of the y-velocity causes the rate of change of the y-velocity along the interface, $\partial v_y/\partial\alpha$, to become negative at these points. Therefore, both $\partial v_x/\partial\alpha$ and $\partial v_y/\partial\alpha$ are now negative, such that the positive part of $\mathcal{T}_3/\gamma$ rapidly increases. The interface therefore further contracts at these points, and the sheet strength increases.

After the multivalue time, the interface rolls over such that $\mathcal{T}_3/\gamma$ and the sheet strength further increase. By $t = 1.5t_m$, $\partial v_x/\partial\alpha$ is now positive at points near VC, such that $\mathcal{T}_3/\gamma$ decreases, but the sheet strength does not change significantly at these points. As the interface further rolls up, $\mathcal{T}_3/\gamma$ becomes negative at points near VC, and the sheet strength has reached a relatively constant value at these points, as seen at $t = 2t_m$.

4.4.1.2 Prediction of the multivalue time

The multivalue time is an important time in the evolution of the interface, as it is the time at which the roll-up becomes visible. To determine t_m, we evaluate the time it takes for a line between two points (A and B) on either side of the vortex core VC to become vertical, as illustrated in Fig. 4.8. Assuming that both of these points have a circular trajectory starting at a distance r from the point VC, and travel with the same constant speed v, their angular velocity $\Omega = v/r$ is constant. The time taken to reach the vertical axis from an initial angle β is thus

$$t_m = \frac{\ell}{v} = \frac{\frac{\pi}{2} - \beta}{\Omega}, \tag{4.4}$$

where $\ell = \int_{\theta=\beta}^{\theta=\frac{\pi}{2}} r d\theta$. The angle β depends on the perturbation amplitude a_0 as follows

$$\beta = \tan^{-1}\left(2\pi\frac{a_0}{\lambda}\right). \tag{4.5}$$

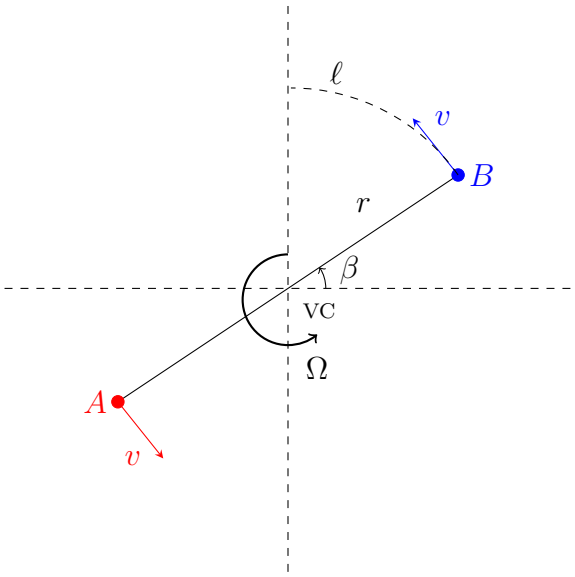

Figure 4.8: Schematic of two points rotating with constant angular velocity around the vortex core.

If the points A and B are close enough to each other they rotate about the point VC with angular velocity equal to half the local vorticity at VC,

$$\Omega_{\mathrm{VC}} = \frac{\omega_{\mathrm{VC}}}{2}. \tag{4.6}$$

Since the vorticity is related to the sheet strength by $\omega = \gamma\delta(n)$, where $\delta(n)$ is the Dirac delta function in the normal direction n, we can write the angular velocity in terms of the sheet strength as

$$\Omega_{\mathrm{VC}} = \frac{\gamma_{\mathrm{VC}}\delta(n)}{2}. \tag{4.7}$$

Using the analytic expression for the sheet strength from Samtaney & Zabusky (1994) for a shock passing over a sinusoidal perturbation, the sheet strength at the point VC is given by

$$\gamma_{\mathrm{VC}} = \frac{2\pi c}{M_s} \frac{a_0/\lambda}{\sqrt{1 + 4\pi^2 \left(a_0/\lambda\right)^2}} \left[\frac{1-A}{1+A} F_1 - F_2\right], \tag{4.8}$$

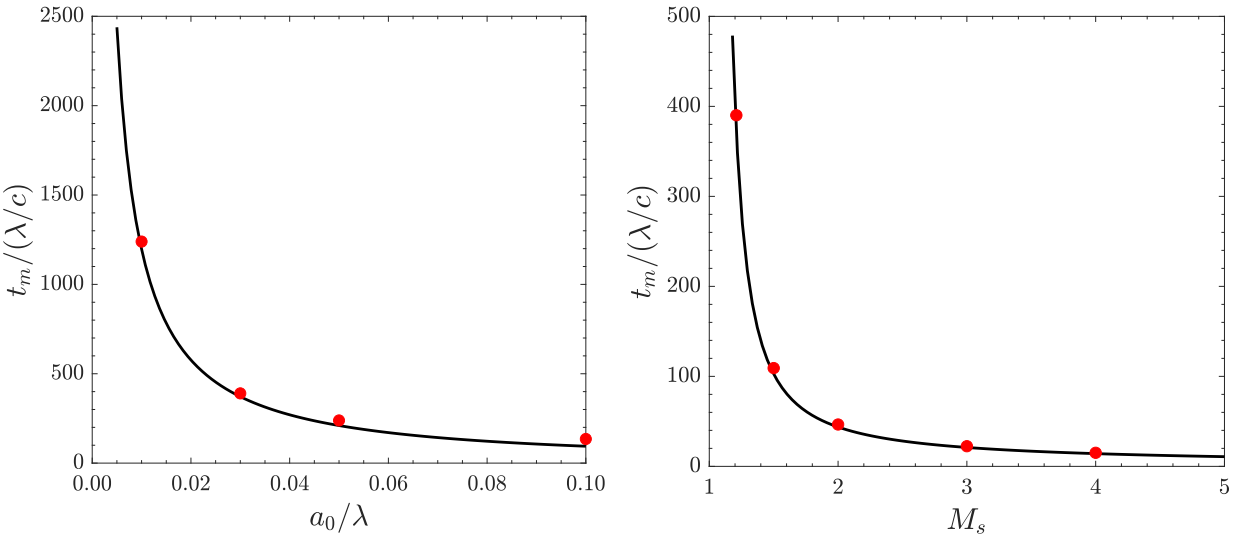

(a) t_m vs. initial amplitude

(b) t_m vs. shock Mach number

Figure 4.9: Dependence of the multivalue time on (a) the initial perturbation amplitude ($M_s = 1.21$), and (b) the shock Mach number ($a_0/\lambda = 0.03$). The solid black line is the prediction from Eq. 4.9, and the red circles are from vortex-sheet simulations.

where c is the sound speed in the + material, and F_1 and F_2 are given in Sec. 2.6. Substituting Eq. 4.8 with $A = 0$ into Eq. 4.4, the multivalue time is therefore given by

$$t_m = \frac{1}{2\pi c\delta(n)} \frac{M_s \left[\pi - 2\tan^{-1}\left(2\pi\frac{a_0}{\lambda}\right)\right] \sqrt{1 + 4\pi^2\left(\frac{a_0}{\lambda}\right)^2}}{\frac{a_0}{\lambda}(F_1 - F_2)}. \tag{4.9}$$

The value of the Dirac delta function $\delta(n)$ is chosen to be of the order of the wavelength, i.e., $\delta(n) = 1/\lambda$. Eq. 4.9 reveals that for $A = 0$ and a given ratio of specific heats and sound speed, the multivalue time only depends on the amplitude-to-wavelength ratio and the shock Mach number. To verify Eq. 4.9, Fig. 4.9 compares the multivalue time from Eq. 4.9 with values obtained from the vortex sheet simulations for different initial perturbation amplitudes and shock Mach numbers. The multivalue time decreases with the amplitude-to-wavelength ratio, which is consistent with the fact that the crests and troughs of the initial perturbation have a steeper slope for larger perturbation amplitudes. When increasing the shock Mach number, the multivalue time decreases as well, due to the larger initial interface velocity for stronger shocks. Our analysis of the multivalue time accurately describes the

dynamics given the good agreement between the results from Eq. 4.9 and the simulations.

4.4.1.3 Time epochs and regimes

To better understand the behavior of the sheet-strength evolution, it is useful to consider the time evolution of representative points along the interface: four in the region of the vortex core, and five far away from it. By symmetry, we only select points initially on the left arm of the interface; similar conclusions can be drawn for the point on the right arm of VC. Fig. 4.10 shows the time evolution of $\mathcal{T}_3/\gamma$ at these points (Fig. 4.10a), along with their corresponding sheet strength value (Fig. 4.10b). To determine segments along the interface that are expanding or contracting, the distance between adjacent points, d, relative to their initial value, d_0, is also shown (Fig. 4.10c). Fig. 4.10a reveals three critical times (at which the interface morphologies close to VC are shown), defining four epochs:

- Epoch 1: this epoch starts from $t = 0$ and extends to the multivalue time t_m. In this epoch, the term $\mathcal{T}_3/\gamma$ is initially negative for all points, thus corresponding to the expansion of the interface immediately after shock passage. After a short time, the interface in the vortex core region starts to contract, as evidenced by the fact that $\mathcal{T}_3/\gamma$ becomes positive for the four points in this region, and that the distance d decreases slightly. $\mathcal{T}_3/\gamma$ starts to increase exponentially, causing an exponential rise in the sheet strength at these points. For the other points away from the vortex core, $\mathcal{T}_3/\gamma$ is negative, causing a decrease in the sheet strength and expansion of the interface at those points.

- Epoch 2: this epoch ranges from t_1 to t_2, the latter being the time at which the slope of the interface at VC is horizontal for the first time. For points in the vortex core region, $\mathcal{T}_3/\gamma$ initially increases exponentially, reaches a maximum value indicating the greatest rate of interface contraction, and starts to decrease. The distance d therefore decreases rapidly, while the sheet strength increases exponentially. For the points

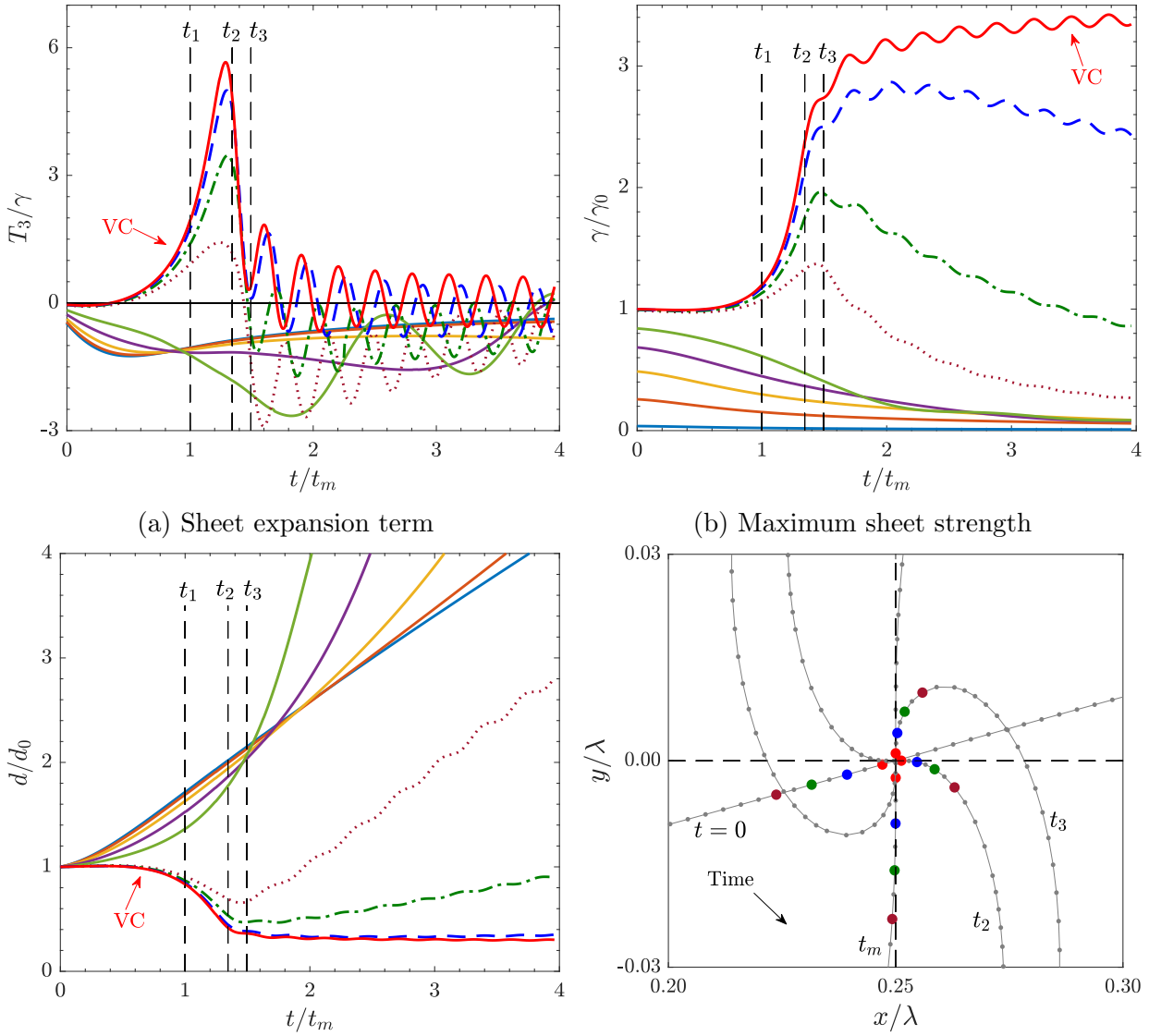

(a) Sheet expansion term

(b) Maximum sheet strength

(c) Distance between adjacent points

(d) Interface morphology

Figure 4.10: Time evolution at different points along the interface of (a) $\mathcal{T}_3/\gamma$, (b) the sheet strength, and (c) the relative distance between adjacent points. The points in the vortex core region are represented by a red solid line, blue dashed line, green dash-dotted line, and maroon dotted line. The other colored points represent points farther away from the vortex core. (d) Interface morphology at the three critical times, with the colored markers corresponding to the colors in (a), (b), and (c).

farther from VC, $\mathcal{T}_3/\gamma$ is still negative, causing a further decrease of the sheet strength and expansion of the interface, thus increasing the distance d.

- Epoch 3: this epoch is defined from t_2 to t_3, the latter being the time at which the interface in the vortex core region becomes multivalued a second time, i.e., when the slope of the interface at VC is infinite. A rotation of 180° has been achieved by the interface from time t_1. In this epoch, $\mathcal{T}_3/\gamma$ for the points in the vortex core region decreases rapidly, indicating a reduction of the rate of contraction of the interface in that region. The distance d and the sheet strength therefore do not change significantly. The term T_3/γ for points further away from the vortex core (maroon and green points) eventually becomes negative, indicating the expansion of the interface in that region.

- Epoch 4: this epoch starts after t_3. From this time onward, $\mathcal{T}_3/\gamma$ oscillates for points in the vortex core region. These oscillations are the result of the fact that after t_3 the points on either size of VC rotate about the vortex core. The interface slope becomes zero and infinite, and so on, thus repeating the epochs outlined previously. This process gives rise to an oscillation in the interface length of points close to VC.

4.4.1.4 Interfacial length oscillations near the vortex core

As described in Sec. 4.4.1.3, the vortex core region undergoes a series of expansions and contractions, leading to oscillations in the sheet strength. As illustrated in Fig. 4.10d, points A and B adopt an orbital trajectory starting approximately at the time when the line between A and B becomes vertical a second time. To better understand this oscillatory behavior, we examine $\mathcal{T}_3/\gamma$ and the angle of the line between A and B and the vertical axis θ in Fourier space in Fig. 4.11. There is a dominant frequency and a mode at $n = 0$ for each of the four points. For $\mathcal{T}_3/\gamma$, this $n = 0$ mode corresponds to a mean shift of the oscillatory profile, indicative of the fact that the oscillations are not centered about equal contraction vs. expansion time. A positive mean shift favors the contraction of the interface, while a

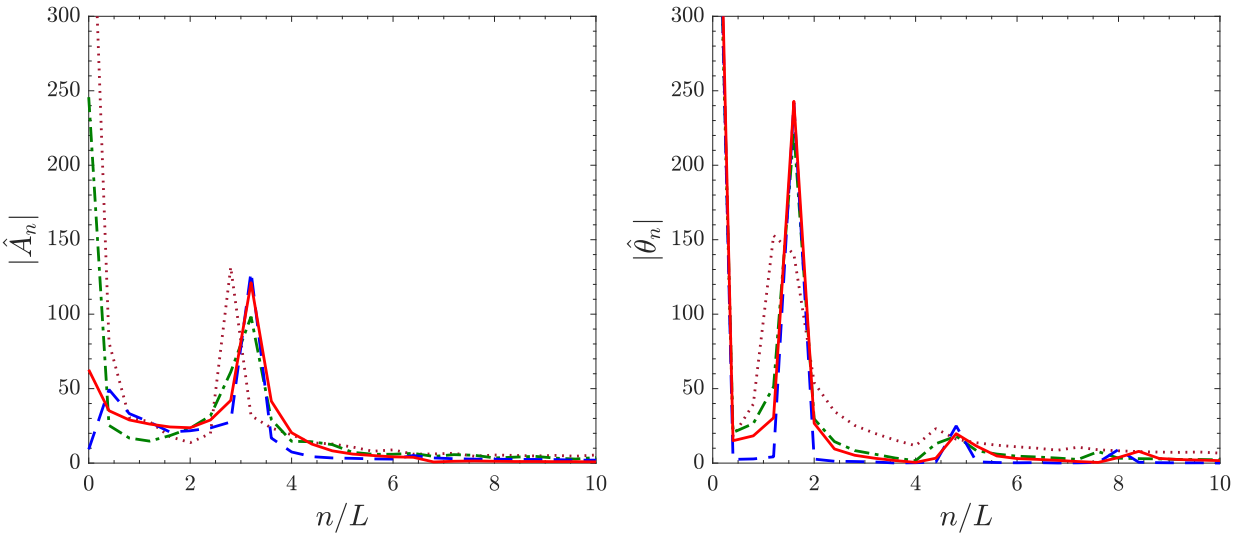

(a) $|\hat{A}_n|$ (b) $|\hat{\theta}_n|$

Figure 4.11: Frequency spectra of (a) the term $\mathcal{T}_3/\gamma$, and (b) the angle θ, for four different points located in the vortex core region. The colors and line styles are the same as in Fig. 4.10. The red curve corresponds to the vortex core.

negative mean shift favors its expansion. Only the point VC has a positive mean shift. For the angle θ, the $n = 0$ mode simply indicates that the angle is measured with respect to the vertical axis rather than the horizontal axis (see Fig. 4.10d). The dominant frequency of $\mathcal{T}_3/\gamma$ for points closest to the vortex core is $n/L \approx 3$, indicating that the interface in the vortex-core region undergoes approximately three cycles of contraction/expansion per t_m. Inspecting Fig. 4.11b reveals that the points near the vortex core orbit the point VC at a frequency $n/L \approx 1.5$, indicating that the contraction/expansion frequency is approximately two times the orbital frequency. The slight difference in frequency between points close to VC and points father away from VC comes from the fact that the latter do not orbit VC as often as points close to VC, hence the lower orbital frequency, resulting in fewer cycles of contractions/expansions.

The oscillatory behavior of the vortex core region may be analogous to the oscillations in the vortex core observed in the evolution of vortex pairs and vortex rings by Krasny & Nitsche (2002). The authors showed that the vortex-core oscillations are the result of the onset of chaos in vortex-sheet flows. Whether the oscillations observed in the present work

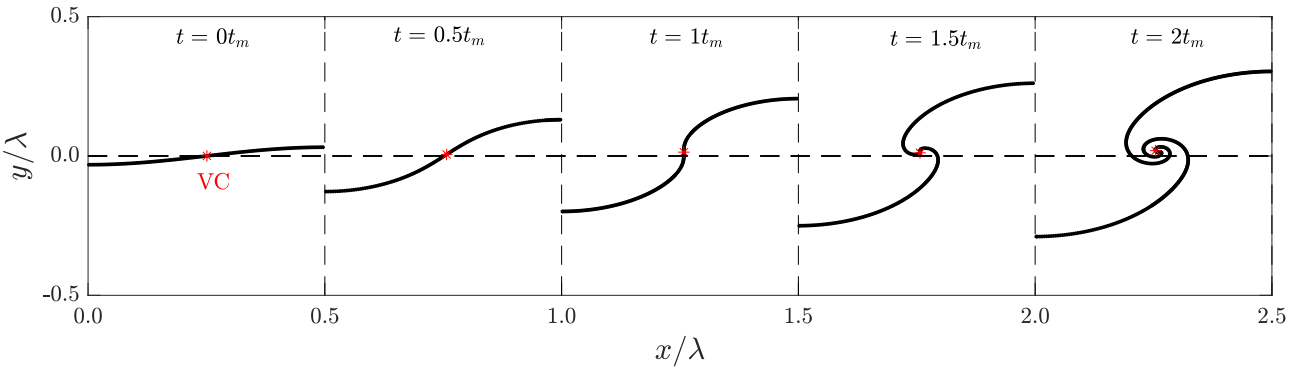

(a) Interface morphology.

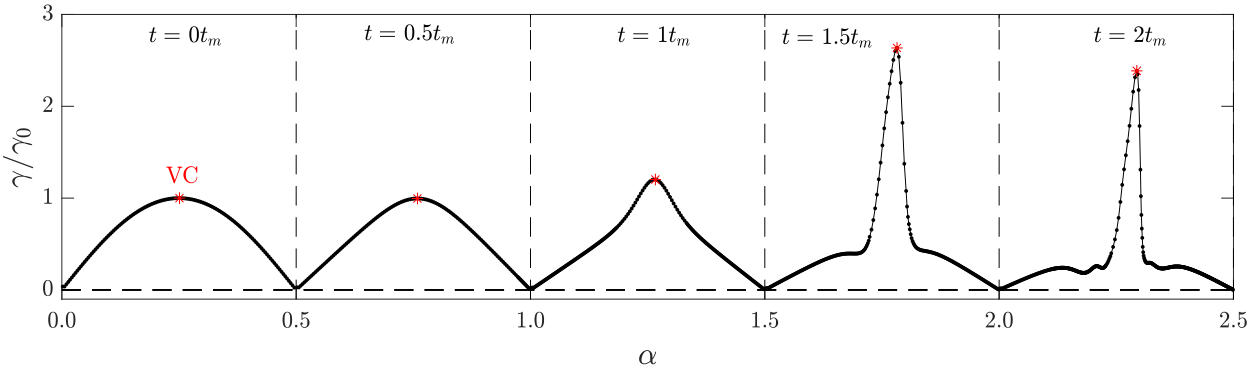

(b) Sheet-strength distribution.

Figure 4.12: Time evolution of (a) the interface, and (b) the corresponding sheet-strength distribution for $A = 0.05$ over half a wavelength. The variable α is a Lagrangian parameter.

are related to the chaotic phenomenon observed by Krasny & Nitsche (2002) is not clear, and will be the focus of a future investigation.

4.4.2 Vorticity dynamics for small Atwood number

We now turn our attention to the case of non-zero but small Atwood number. As a representative example, Fig. 4.12 shows the evolution of the interface and the sheet strength for $A = 0.05$ and Fig. 4.13 shows the evolution of the terms $\mathcal{T}_1$, $\mathcal{T}_2$, and $\mathcal{T}_3$ (Eq. 4.1). The heavy fluid is on the $-$ side and the light fluid is on the $+$ side (see Fig. 4.1).

Initially, the interface, the sheet-strength distribution, and $\mathcal{T}_3$ are the same as in the case $A = 0$ (Fig. 4.6). The terms $\mathcal{T}_1$ and $\mathcal{T}_2$ are now non-zero and distributed sinusoidally along the interface. For $A > 0$, $\mathcal{T}_1$, representing the local tangential acceleration of the points along

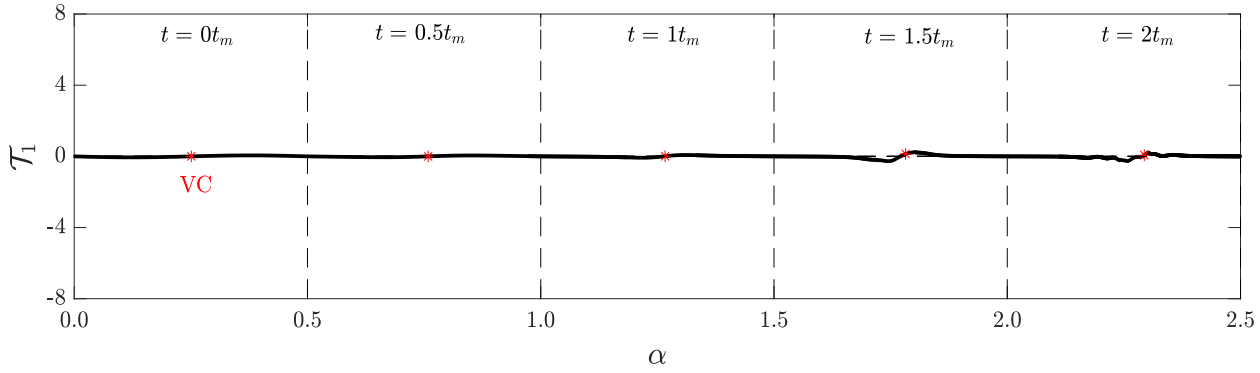

(a) $\mathcal{T}_1$

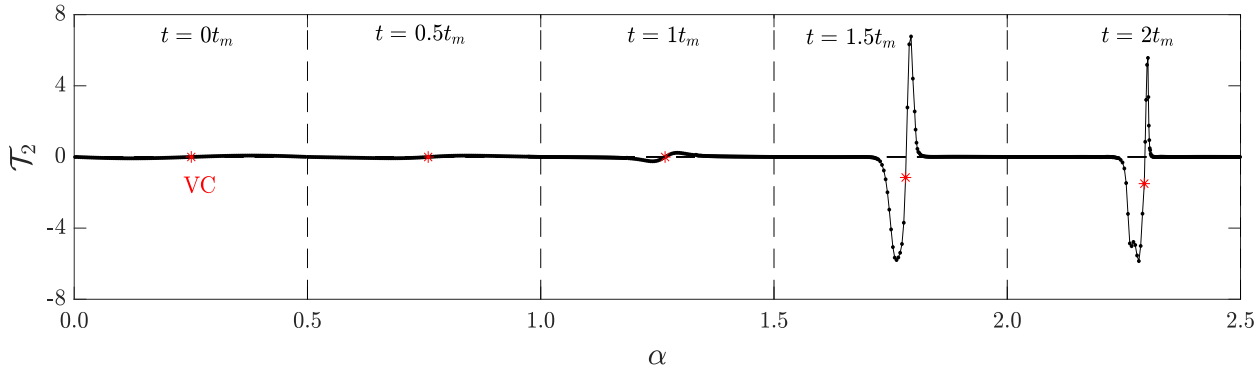

(b) $\mathcal{T}_2$

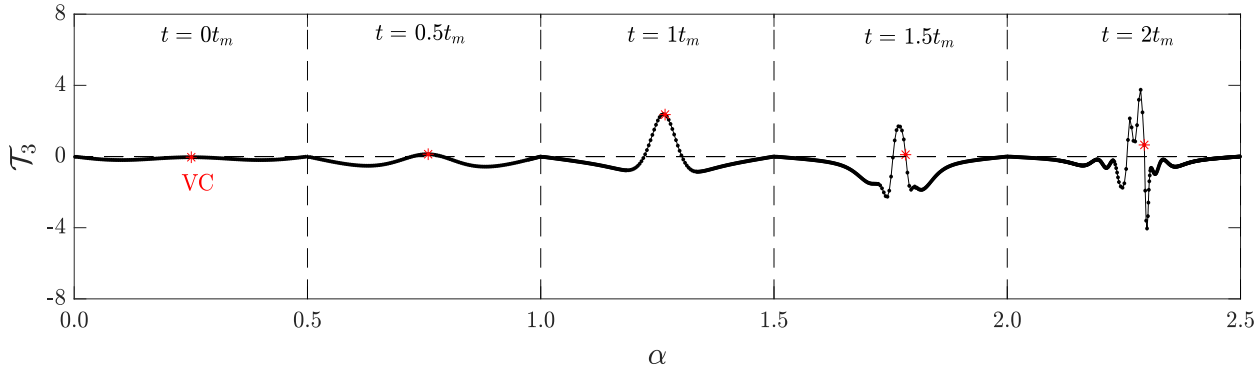

(c) $\mathcal{T}_3$

Figure 4.13: Time evolution of the three terms for $A = 0.05$: (a) $\mathcal{T}_1$, (b) $\mathcal{T}_2$, and (c) $\mathcal{T}_3$ over half a wavelength. The variable α is a Lagrangian parameter.

the interface, is negative on the left arm and positive on the right arm, due to the fact that the interface velocity is negative on the left arm, and positive on the right arm. Similarly, $\mathcal{T}_2$, representing the advection of the sheet strength, is negative on the left arm and positive on the right arm, indicating that the sheet strength on both arms is advected toward VC.

Until the multivalue time ($t = t_m$), the behavior of the interface, the sheet strength, and $\mathcal{T}_3$ are similar as in the $A = 0$ case, and $\mathcal{T}_1$ and $\mathcal{T}_2$ do not change significantly. At $t = t_m$, the profile of $\mathcal{T}_2$ slightly steepens near VC; its magnitude is of the order of that of $\mathcal{T}_1$, but is an order of magnitude smaller than $\mathcal{T}_3$. As in the $A = 0$ case, $\mathcal{T}_3$ forms a peak due to the contraction of the interface near VC, but is slightly asymmetric, i.e., $\mathcal{T}_3$ is no longer equally distributed on either side of VC. The sheet-strength profile is now slightly shifted to the right due to the non-zero term $\mathcal{T}_2$. As stated previously, this term is effectively a nonlinear advection term similar to that of an advection equation, which translates and steeps the initial profile.

At $t = 1.5t_m$, the profile of $\mathcal{T}_2$ steepens further near VC; its magnitude significantly increases and reaches values larger than $\mathcal{T}_3$. However, $\mathcal{T}_2$ is close to zero elsewhere, indicating that the sheet strength is advected primarily in the vortex-core region. The sheet-strength profile steepens and forms a peak at the vortex core, further shifting to the right. By $t = 2t_m$, the asymmetry between the left and right arms of the interface morphology is clearly visible. When compared to the $A = 0$ case, the vortex core (red star) has shifted above the $y = 0$ axis, due to the slightly higher momentum associated with the heavy fluid.

4.5 Dependence of opposite-sign vorticity on the shock Mach number

We now investigate the effect of the incident shock Mach number on the generation of opposite-sign vorticity. The Atwood number is kept constant and corresponds to the value given by our baseline, $A = 0.6053$.

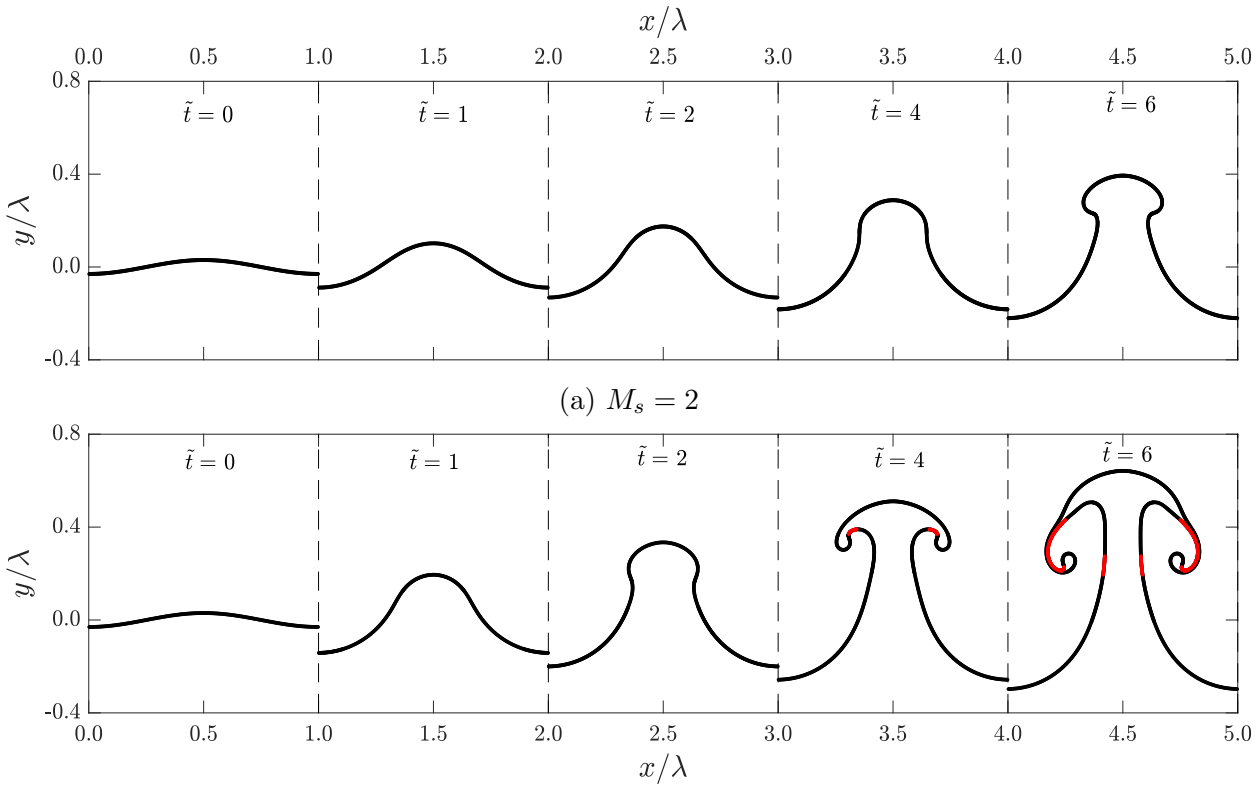

(a) $M_s = 2$

(b) $M_s = 5$

Figure 4.14: Time evolution of the perturbation for (a) $M_s = 2$, and (b) $M_s = 5$, with $A = 0.6053$. The red dots show the development of opposite-sign vorticity along the interface.

4.5.1 Multivalue and onset times

The effect of the incident shock Mach number inherently lies in the initial conditions, as the magnitude of the sheet-strength distribution along the interface, γ_0, increases with the shock Mach number, as shown in Fig. 4.2a. From the Biot-Savart law in Eq. 2.31, this increase in the sheet-strength magnitude results in a larger initial interface velocity. Therefore, we expect that, for a given Atwood number, the interface evolves faster for a higher shock Mach number, which in turn leads to opposite-sign vorticity to develop sooner. This observation is confirmed in Fig. 4.14, which shows the interface morphology for two different shock Mach number, $M_s = 2$ and $M_s = 5$. For $M_s = 2$, the perturbation growth is mainly in the linear phase and before its multivalue time ($\tilde{t} \approx 4$), after which the roll-up just started to form. Opposite-sign vorticity has not developed for the time range considered, $\tilde{t} \leq 6$. For

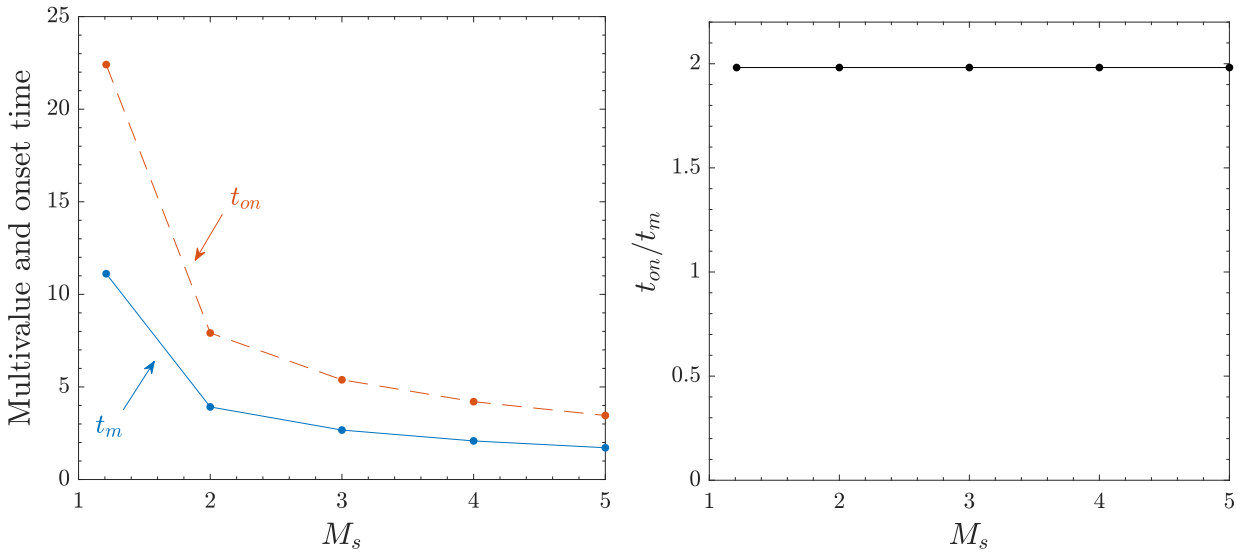

(a) t_m and t_{on} vs. M_s (b) t_{on}/t_m vs. M_s

Figure 4.15: Shock Mach number dependence of (a) the multivalue time $t_m/(\lambda/c)$ and onset time $t_{on}/(\lambda/c)$, and (b) the ratio t_{on}/t_m. The Atwood number is $A = 0.6053$.

$M_s = 5$, however, the linear phase and the first instance of a multivalued interface occurs sooner ($\tilde{t} < 2$), and the development of opposite-sign vorticity is now evident. Note that for $M_s = 1.21$, see Fig. 4.3, the interface did not become multivalued until $\tilde{t} = 11$, emphasizing the fact that the interface develops sooner for higher shock Mach numbers. This behavior is further demonstrated in Fig. 4.15, which shows the dependence of the multivalue time and the onset time with the shock Mach number. When increasing the shock Mach number, both the multivalue and onset times decrease, indicating that the interface becomes multivalued and develops opposite-sign vorticity sooner, further confirming the behavior seen in Fig. 4.14. The relationship between the onset time and the multivalue time is illustrated in Fig. 4.15b, which shows the ratio of the onset time to the multivalue time as a function of the shock Mach number. The ratio has a maximum variation of $\sim 0.1\%$ with respect to its arithmetic average value. Therefore, it can be considered constant with respect to the shock Mach number, such that $t_{on}/t_m = C$, where $C \approx 2$. The variation in the values of the ratio comes from the fact that the numerical output time step is not exactly the same for each case. This behavior is the result of a scaling in time of the interface with velocity, or shock

M_s \ A	0	0.2	0.4	**0.6053**	0.8
1.21	0.4	6	11	**16**	22
2				46	
3				68	
4				87	
5				106	

Table 4.2: Values of γ_0 [m/s] for different incident shock Mach numbers and Atwood numbers. The bold font corresponds to our baseline case from Collins & Jacobs (2002).

Mach number.

4.5.2 Time scaling with the shock Mach number

The Samtaney & Zabusky (1994) model (Eq. 3.2) indicates that the initial sheet-strength profile along the interface depends on the geometry of the perturbation alone, and not on the shock Mach number. Varying the latter only results in changing the initial magnitude of the sheet-strength profile, γ_0, as observed in Fig. 4.2a. As such, using γ_0 to non-dimensionalize the sheet-strength variable, results in collapsing all the curves in Fig. 4.2a onto a single one. Table 4.2 shows the value of γ_0 for the shock Mach numbers and the Atwood numbers under consideration. Since the shock Mach number only appears in the initial conditions and does not appear in the equations governing the kinematics or dynamics, this collapse of the initial sheet-strength profile indicates that the time evolution of the perturbation scales with the shock Mach number. Therefore, using γ_0 as characteristic velocity, instead of the sound speed c, to non-dimensionalize time as $t/(\lambda/\gamma_0)$, this scaling is demonstrated in Fig. 4.16, showing the interface morphology at two different times. At a given time, the interface morphology is the same regardless of the value of the shock Mach number. Therefore, the shock Mach number acts as a time scaling of the evolution of the interface, where the stronger the incident shock, the sooner the interface goes through the different phases of the growth: first the linear regime, then the interface becomes multivalued, rolls up, to eventually generate opposite-sign vorticity.

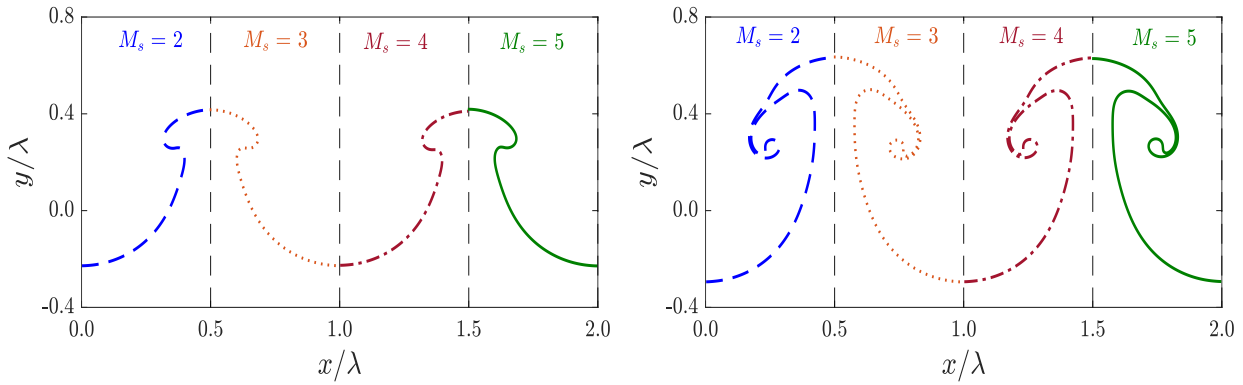

(a) $t/(\lambda/\gamma_0) = 1$ (b) $t/(\lambda/\gamma_0) = 2$

Figure 4.16: Interface morphology at (a) $t/(\lambda/\gamma_0) = 1$ and (b) $t/(\lambda/\gamma_0) = 2$ for different shock Mach numbers. The interface morphology is shown over half a wavelength for each shock Mach number and separated by a vertical dashed line. The Atwood number is $A = 0.6053$.

This time scaling of the interface behavior with the shock Mach number results in the multivalue time and onset time to be independent of the shock Mach number, as shown in Fig. 4.17. Therefore, both the multivalue and onset times can be written as

$$t_m = C_m \frac{\lambda}{\gamma_0} \quad , \quad t_{on} = C_{on} \frac{\lambda}{\gamma_0}, \tag{4.10}$$

where $C_m(A)$ and $C_{on}(A)$ are two different functions that only depend on the Atwood number. The dependence of the initial sheet-strength magnitude, γ_0, on the shock Mach number can be obtained from the scaling laws derived by Samtaney & Zabusky (1994), who showed that the circulation per unit length of the interface scales as

$$\gamma = \frac{2c}{\kappa + 1} \sin\alpha \left(1 + M_s^{-1} + 2M_s^{-2}\right) (M_s - 1) \left(1 - \sqrt{\frac{1-A}{1+A}}\right). \tag{4.11}$$

The value of γ_0 is located where the angle between the incident shock and the interface is maximum, i.e., at $x = \lambda/4$, which gives $\tan\alpha_{\max} = ka_0$. Therefore, using Eq. 4.11 the

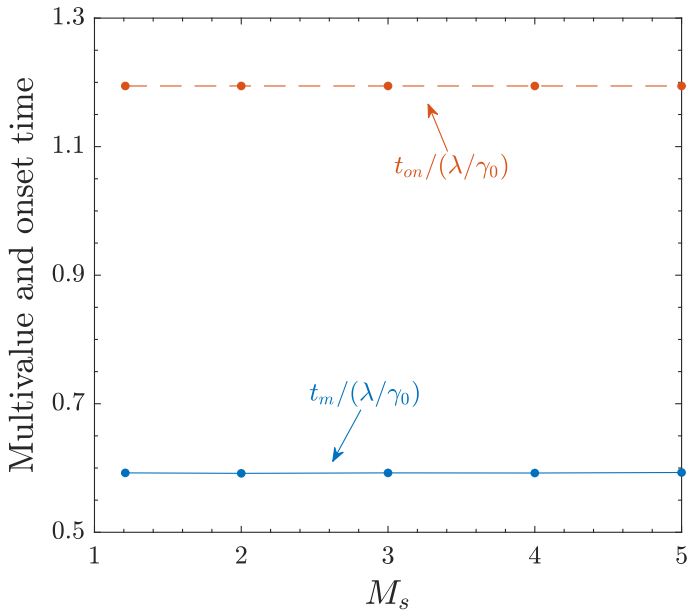

Figure 4.17: Dependence of the scaled multivalue time $t_m/(\lambda/\gamma_0)$ and onset time $t_{on}/(\lambda/\gamma_0)$ on the shock Mach number with $A = 0.6053$.

multivalue and onset times can be written as

$$
\begin{aligned}
t_m &= \frac{\kappa+1}{2c}\cdot\frac{\lambda}{\sin\alpha_{\max}}\cdot\frac{1}{(1+M_s^{-1}+2M_s^{-2})\,(M_s-1)}\cdot\frac{C_m(A)}{1-\sqrt{\frac{1-A}{1+A}}} \\
t_{on} &= \frac{\kappa+1}{2c}\cdot\frac{\lambda}{\sin\alpha_{\max}}\cdot\frac{1}{(1+M_s^{-1}+2M_s^{-2})\,(M_s-1)}\cdot\frac{C_{on}(A)}{1-\sqrt{\frac{1-A}{1+A}}}.
\end{aligned}
\tag{4.12}
$$

The right-hand side of Eq. 4.12 indicates that the multivalue and onset times depend on the products of four factors: the first related to the fluids material properties, the second related to the geometry of the initial perturbation, the third related to the strength of the incident shock Mach number, and the fourth one related to the density mismatch across the interface.

4.5.3 Opposite-sign circulation

The fact that the onset time is smaller for higher shock Mach number results in opposite-sign vorticity to develop over a longer period of time, thus leading to a larger amount of opposite-sign circulation at a given time. Fig. 4.18 shows the time evolution of opposite-sign

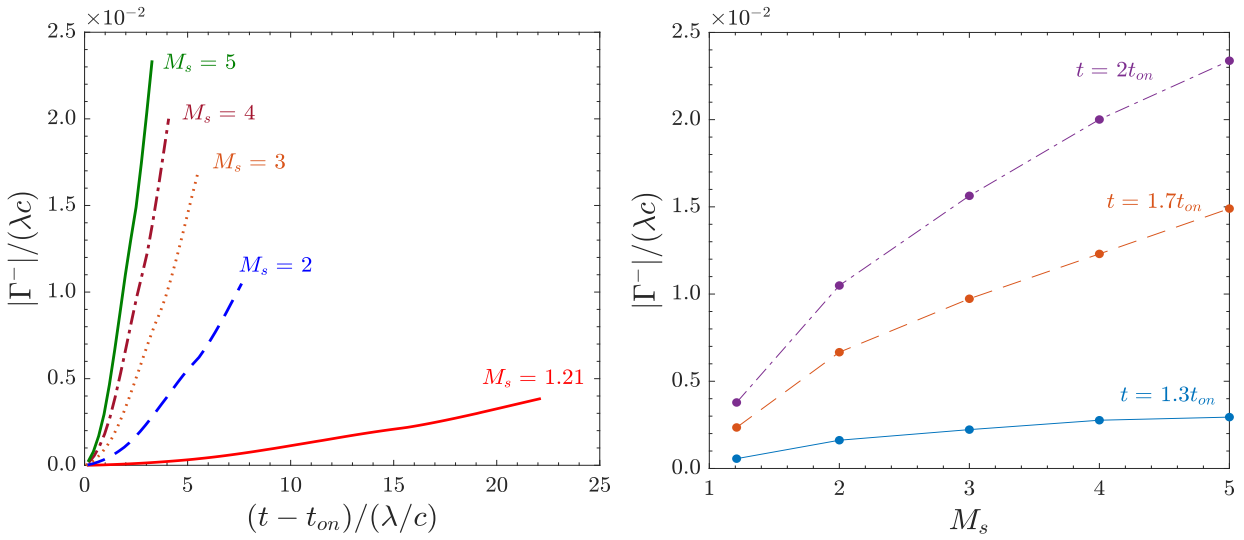

(a) Opposite-sign circulation vs. time

(b) Opposite-sign circulation vs. M_s

Figure 4.18: (a) Time evolution of opposite-sign circulation shifted by the onset time for different shock Mach numbers, and (b) dependence of opposite-sign circulation with the shock Mach number at different times past the onset time. The Atwood number is $A = 0.6053$.

vorticity for different shock Mach numbers. The time origin in Fig. 4.18a is shifted by the onset time, which has a different value for each shock Mach number. The time evolution of opposite-sign circulation for all the shock Mach numbers considered follows a similar trend as for the baseline case, i.e., monotonically increasing (in magnitude). Fig. 4.18b shows the dependence of opposite-sign circulation with the shock Mach number at different given times past the onset time. Opposite-sign circulation increases monotonically with the shock Mach number, at a rate increasing with increasing Mach number. For large Mach numbers, the rate of increase of opposite-sign circulation is relatively constant. This behavior is consistent with the linear scaling with respect to the shock Mach number of the initial circulation for large shock Mach numbers found in Samtaney & Zabusky (1994), thus suggesting that any vorticity generated after the primary vorticity (from the shock-interface interaction) follows a similar behavior. This observation is consistent with the fact that both primary (initial) and secondary (late-time) vorticity originate from a baroclinic mechanism. Fig. 4.19 shows the results of Fig. 4.18a but scaled with the initial sheet strength γ_0. Since the interface behavior scales in time with the shock Mach number, all the curves collapse onto a single

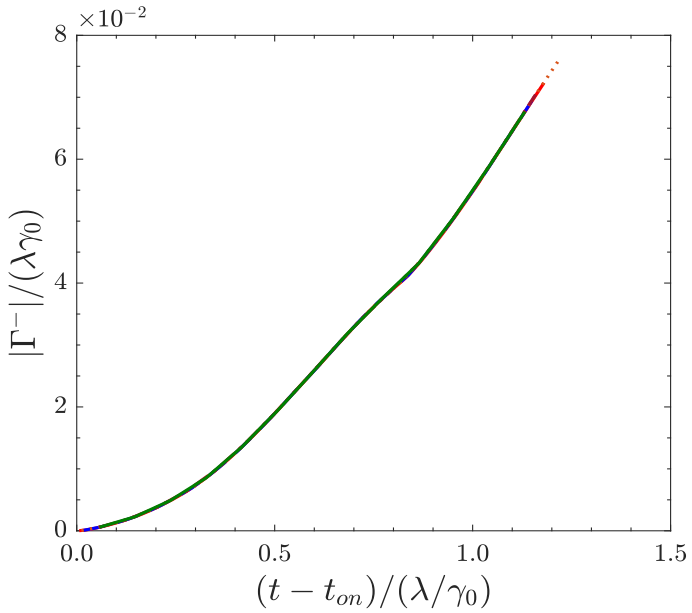

Figure 4.19: Time evolution of the scaled opposite-sign circulation shifted by the onset time for different shock Mach numbers with $A = 0.6053$.

one, demonstrating the fact that the amount of opposite-sign circulation is independent of the shock Mach number.

4.6 Dependence of opposite-sign vorticity on the Atwood number

We now investigate the effect of the Atwood number on the generation of opposite-sign vorticity. The shock Mach number is kept constant and corresponds to the value given by our baseline, $M_s = 1.21$. To simplify the determination of the initial conditions, we focus on a light-to-heavy configuration ($A > 0$); the heavy-to-light configuration ($A < 0$) is currently under investigation. Like with the shock Mach number, the initial sheet strength depends on the Atwood number (see Fig. 4.2b); a larger value of the Atwood number results in a larger magnitude of the initial sheet strength, leading to a higher initial interface velocity, which would result in opposite-sign vorticity to develop sooner. However, unlike the shock Mach number, the Atwood number explicitly appears in the vortex-sheet dynamics equation

(Eq. 4.1), such that different Atwood numbers give rise to different dynamics and therefore interface morphologies that are no longer similar. Fig. 4.20 shows the interface morphology for three different Atwood numbers, $A = 0.4$, $A = 0.6053$, and $A = 0.8$. When increasing the Atwood number, the distance (in the x-direction) between points located on the left-half domain and points on the right-half domain decreases, forming a narrower mushroom neck, as illustrated at $\tilde{t} = 11$ for example. Furthermore, the perturbation height increases when increasing the Atwood number due to the relatively higher momentum of the heavy fluid. The interface morphology is also different when increasing the Atwood number, both in terms of the spike shape and the roll-up. For $A = 0.4$ and $A = 0.6053$, the spike has a rounded shape (e.g., at $\tilde{t} = 33$), whereas the spike is not as well-rounded for $A = 0.8$. The roll-up in the $A = 0.6053$ case has a filament-like structure, while the roll-up is less elongated for $A = 0.4$ and $A = 0.8$. In the latter case, part of the roll-up near the neck is nearly horizontal.

As opposed to the shock Mach number, the perturbation evolution shown Fig. 4.20 does not suggest a time scaling of the interface behavior with the Atwood number, as different Atwood numbers lead to different interface morphologies. We therefore do not expect opposite-sign vorticity to increase monotonically with the Atwood number. To demonstrate this behavior, Fig. 4.21 shows the dependence of the multivalue time and onset time on the Atwood number. For visualization purposes, the $y-$axis is in logarithmic scale. The multivalue time decreases monotonically with increasing Atwood number, indicating that the interface becomes multivalued sooner for increasing Atwood numbers. The onset time, however, does not decrease monotonically with the Atwood number, but has a minimum value at $A \approx 0.6$. For $A = 0$, no value of the onset time is shown, due to the fact the onset time is infinite, i.e., opposite-sign vorticity never develops. Fig. 4.22 shows the dependence of opposite-sign circulation with the Atwood number. As with the shock Mach number, the amount of opposite-sign circulation increases monotonically with time for all values of the Atwood number considered. However, Fig. 4.22b shows that as the Atwood

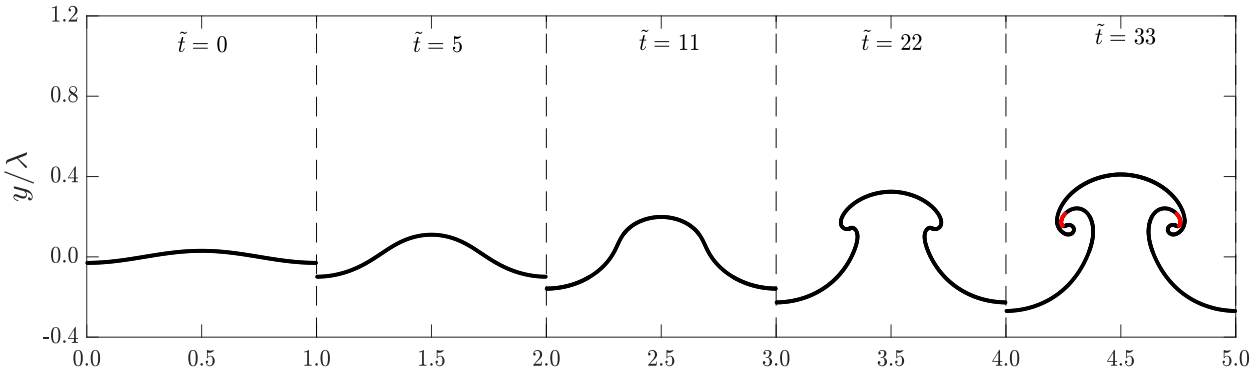

(a) $A = 0.4$.

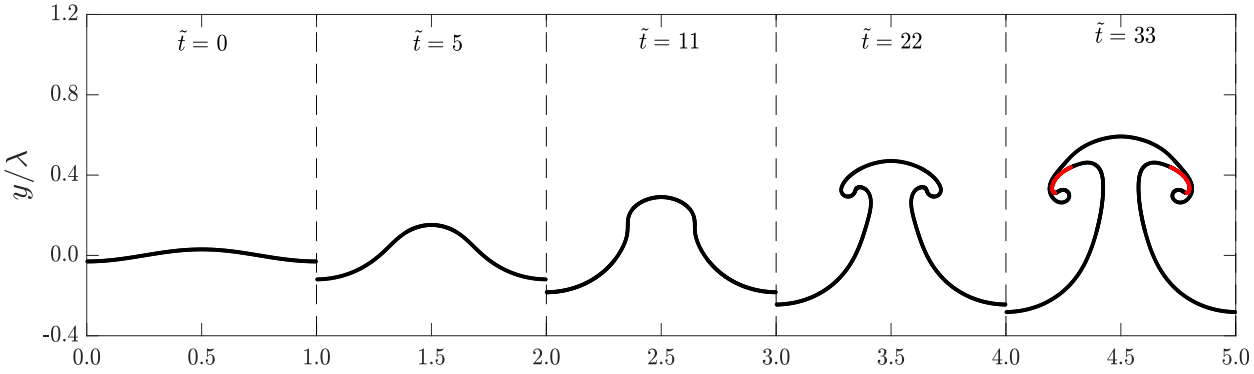

(b) $A = 0.6053$.

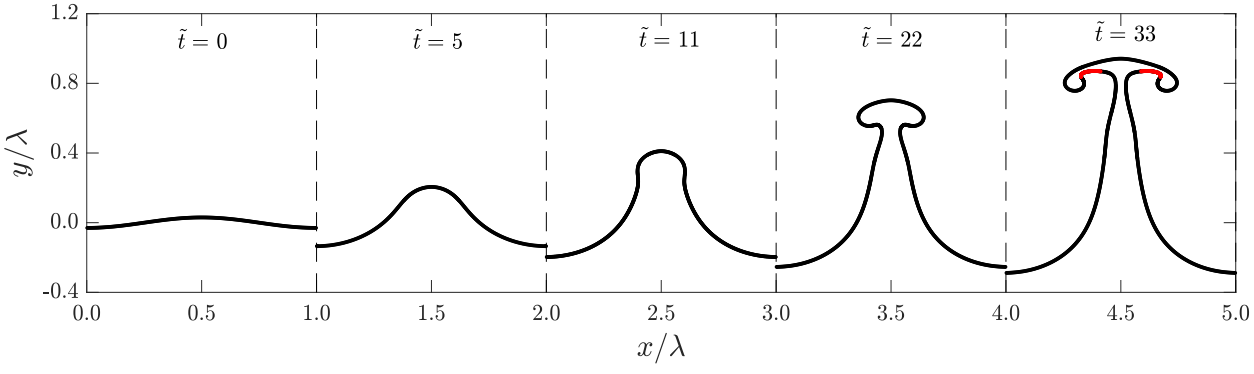

(c) $A = 0.8$.

Figure 4.20: Time evolution of the perturbation for (a) $A = 0.4$, (b) $A = 0.6053$, and (c) $A = 0.8$ with $M_s = 1.21$. The red dots show the development of opposite-sign vorticity along the interface.

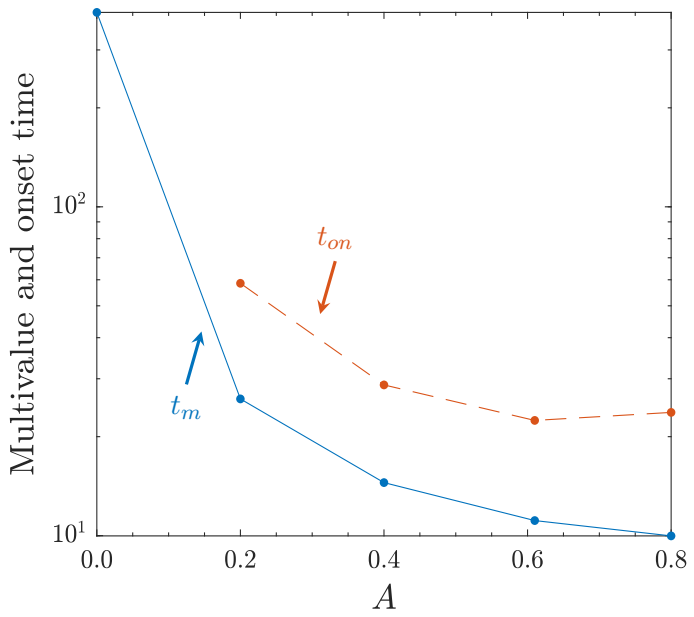

Figure 4.21: Atwood number dependence of the multivalue time $t_m/(\lambda/c)$ and onset time $t_{on}/(\lambda/c)$ in logarithmic scale for the $y-$axis. The shock Mach number is $M_s = 1.21$.

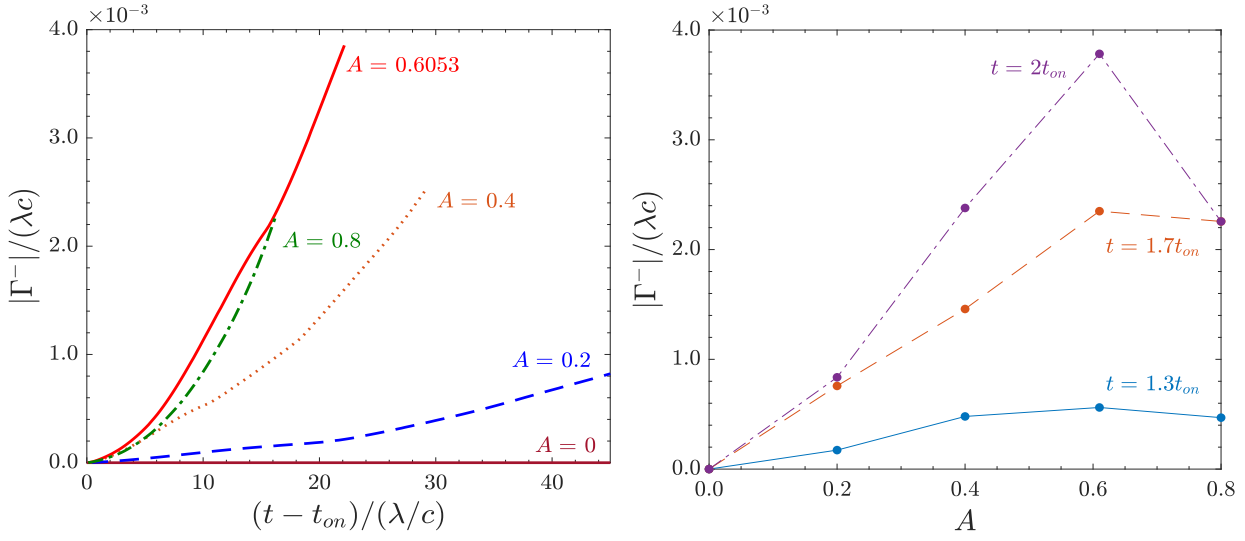

(a) Opposite-sign circulation vs. time

(b) Opposite-sign circulation vs. A

Figure 4.22: (a) Time evolution of opposite-sign circulation shifted by the onset time for different Atwood numbers, and (b) dependence of opposite-sign circulation with the Atwood number at different times past the onset time. The shock Mach number is $M_s = 1.21$.

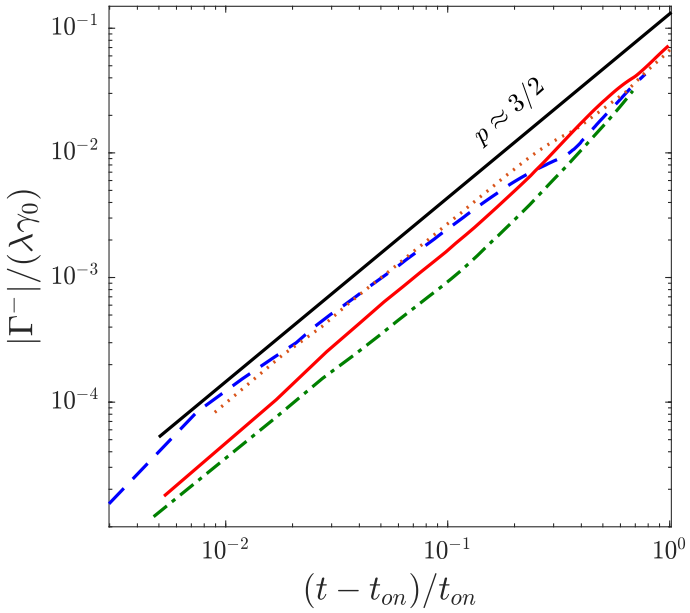

Figure 4.23: Time evolution of the scaled opposite-sign circulation shifted by the onset time for different Atwood numbers in log-log scale: $A = 0.2$ (- - -), $A = 0.4$ (·····), $A = 0.6053$ (——), and $A = 0.8$ (-·-·). The solid black line is obtained from a linear regression.

number increases, opposite-sign circulation increases and then decreases, with a maximum at $A \approx 0.6$, showing the non-monotonic behavior of opposite-sign circulation with the Atwood number. The fact that the maximum is for $A \approx 0.6$ is due to the fact that the onset time is minimum for that Atwood number, thus leading to opposite-sign vorticity to develop over a longer period of time. For $A = 0$, there is no opposite-sign circulation, confirming our previous observation that opposite-sign vorticity never develops for $A = 0$. Fig. 4.23 shows the results of Fig. 4.22a but scaled with the initial sheet strength γ_0 and in log-log scale. For convenience, time is scaled with the onset time t_{on}. Opposite-sign circulation shows a power-law behavior:

$$\frac{|\Gamma^-|}{\lambda\gamma_0} = e^b \left(\frac{t}{t_{on}} - 1 \right)^p, \tag{4.13}$$

where b is a function only of the Atwood number. Applying a least-squares fit to the data

reveals that $p \approx 3/2$. For $t/t_{on} \gg 1$,

$$\frac{|\Gamma^-|}{\lambda\gamma_0} \propto \left(\frac{t}{t_{on}}\right)^p, \tag{4.14}$$

and from Eq. 4.10, opposite-sign circulation evolves as

$$|\Gamma^-| \propto \gamma_0^{p+1} t^p. \tag{4.15}$$

4.7 Dependence of opposite-sign vorticity on both the shock Mach number and the Atwood number

In Secs. 4.5 and 4.6, we investigated the dependence of opposite-sign vorticity on the shock Mach number (respectively, Atwood number) when the Atwood number (respectively, shock Mach number) is held constant. Fig. 4.24 shows the dependence of the multivalue time and onset time on the shock Mach number and the Atwood number in the full parameter space. The largest values of the multivalue time lie in the region of low-Atwood and low-Mach numbers, $A \lesssim 0.2$ and $M_s \lesssim 2$. Since the onset time takes place after the multivalue time, the onset of opposite-sign vorticity is delayed in that region of the parameter space, as demonstrated by the large values of the onset time. As observed in Sec. 4.6, opposite-sign vorticity does not develop for $A = 0$, such that for low Atwood numbers ($A \lesssim 0.1$), the onset time is large for all values of the shock Mach number. In contrast, regions of high-Atwood and high-Mach numbers, $A \gtrsim 0.6$ and $M_s \gtrsim 4$, correspond to cases where opposite-sign vorticity develops sooner, as evidenced by the small values of the multivalue and onset times. To relate these findings to practice, the experiments of Collins & Jacobs (2002), represented by a white dot, lie in the region of high-Atwood number ($A = 0.6053$), but low-Mach number ($M_s = 1.21$), indicating that opposite-sign vorticity develops relatively late compared to the same experiments performed at a higher shock Mach number. This

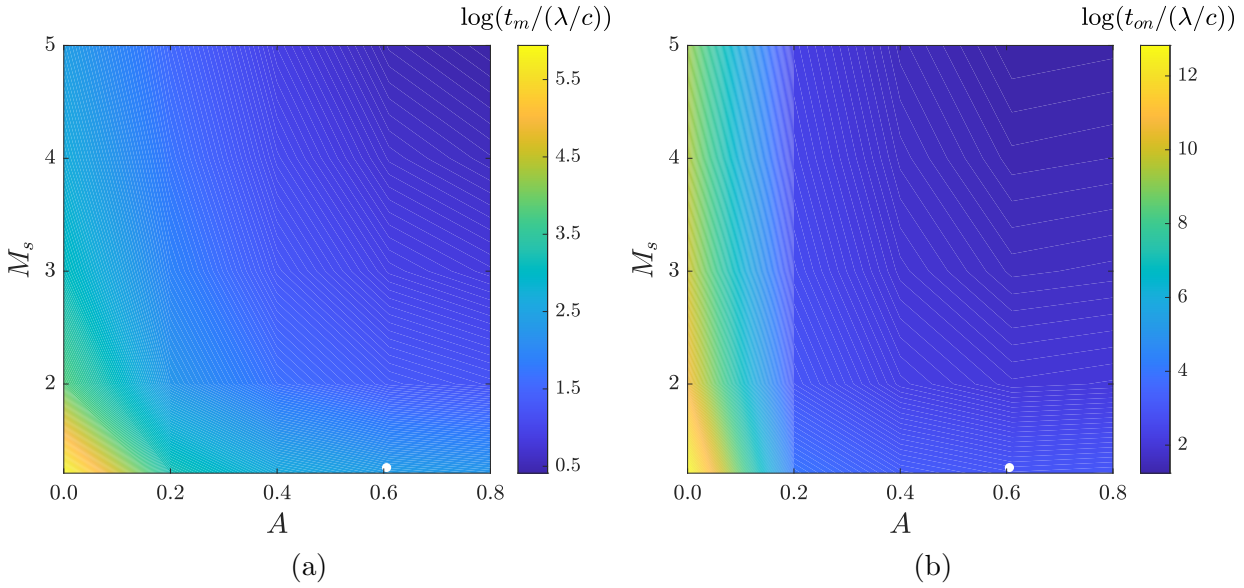

Figure 4.24: Logarithmic value of (a) the multivalue time $t_m/(\lambda/c)$ and (b) the onset time $t_{on}/(\lambda/c)$ in the parameter space (A, M_S). The white dot corresponds to the experiments of Collins & Jacobs (2002) (baseline case).

observation is confirmed in Fig. 4.25, which shows the dependence of opposite-sign vorticity on the shock Mach number and Atwood number in the parameter space at three different times past the onset time. The experiments of Collins & Jacobs (2002) lie in the region where the amount of opposite-sign circulation is small compared to the amount produced at higher Mach numbers. As observed in Secs. 4.5 and 4.6, the amount of opposite-sign vorticity increases with time, as shown by the different color bar scales. The region of maximum opposite-sign vorticity decreases over time.

4.8 Conclusion

In this chapter, we use a vortex-sheet model to investigate the development of opposite-sign vorticity in the single-mode Richtmyer–Meshkov instability. The vortex-sheet model allows us to isolate the different contributions of vorticity production in the evolution of the interface: a term accounting for the local acceleration of the interface, a term accounting for the advection of vorticity along the interface, and a term accounting for the expansion and

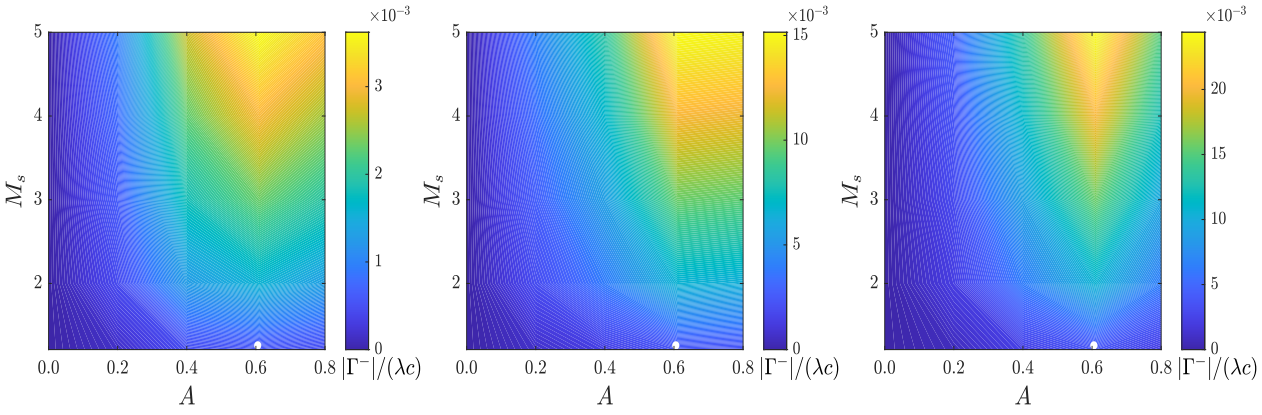

Figure 4.25: Value of opposite-sign circulation in the parameter space (A, M_s) at (a) $t = 1.3t_{on}$, (b) at $t = 1.7t_{on}$, and (c) at $t = 2t_{on}$. The white dot corresponds to the experiments of Collins & Jacobs (2002) (baseline case).

contraction of the interface.

In the case of no density mismatch at the interface ($A = 0$), opposite-sign vorticity never develops, due to the fact that there is no baroclinic mechanism in the evolution of the vorticity dynamics. In this case, changes in the vorticity distribution along the interface originate only from the expansion and contraction of the interface. We observe that the vortex core undergoes a series of expansions and contractions with frequency $3t_m$, where t_m is the multivalue time, which corresponds to approximately twice the orbital frequency of the points along the interface. By using geometric arguments, we derive an analytical expression for the multivalue time, which agrees well with our vortex-sheet simulations.

When considering positive and negative vorticity between a bubble and a spike for non-zero Atwood numbers, part of the initially-positive vorticity eventually becomes negative, suggesting that opposite-sign (negative) vorticity is generated only is A is not zero. By contrast with the zero-Atwood number case, the evolution of the vorticity distribution for small Atwood numbers is additionally affected by the local tangential acceleration of the interface and nonlinear vorticity advection along the interface. For a short period after the multivalue time, the latter is dominant over the former, suggesting that opposite-sign vorticity is generated by the nonlinear vorticity advection along the interface.

Finally, when varying the incident shock Mach number and the Atwood number, the emergence of opposite-sign vorticity is delayed for low-Atwood numbers ($A \lesssim 0.2$) and low-Mach numbers ($M_s \lesssim 0.2$); the amount of opposite-sign circulation is the lowest for these Mach and Atwood numbers. In contrast, the amount of opposite-sign circulation is the largest for $A \gtrsim 0.6$ and $M_s \gtrsim 4$. When only varying the shock Mach number but keeping the Atwood number fixed, the interface behavior scales in time with respect to the shock Mach number, such that the latter simply acts as a time scaling in the evolution of the interface. This behavior results in opposite-sign vorticity to develop at the same time for all shock Mach numbers, and to behave according to a power law in time.

CHAPTER 5

Concluding Remarks and Future Directions

This chapter summarizes the work presented in the current thesis, with key findings and contributions to the field, along with suggestions for future directions.

5.1 Summary and conclusions

The objective of this work is to develop a vorticity-based framework to explain the role of vorticity dynamics in the evolution of hydrodynamic instabilities driven by baroclinic vorticity, relevant to many applications, e.g., in high-energy-density (HED) systems (inertial confinement fusion, supernova explosion), cavitation, lung hemorrhage, and supersonic aircrafts. To accomplish this objective, we used a vortex-sheet model appropriately initialized under conditions relevant to these applications, which allowed us to

- Investigate the late-time vorticity dynamics of perturbations subjected to an oblique shock to understand the relative importance between Kelvin–Helmholtz (KH) and Richtmyer–Meshkov (RM) instabilities in HED experiments. Using complementary direct simulations, the vortex-sheet initial conditions were carefully determined to match the conditions of the experiments. The subsequent evolution of the perturbation is dictated by the changes in the sheet-strength distribution along the interface. At early times, the perturbation growth is dominated by the impulsive acceleration of the shock (RM), as evidenced by our proposed scaling accounting for the normal and tangential

components of the shock. At later times, the perturbation growth is modulated by the positive and negative sheet strength generated by the shear. By extending the vortex-sheet model to time-dependent field accelerations, we were able to account for the interface decompression and RT-acceleration occurring due to experimental laser turn-off, and obtained reasonable agreements with the experiments.

- Study the role of opposite-sign vorticity generation in the late-time evolution of the single-mode Richtmyer–Meshkov instability. By isolating the vorticity dynamics, we showed that for zero Atwood number, the vorticity distribution between a bubble and a spike maintains its sign forever, with the interface near the vortex core undergoing expansions and contractions, thus giving rise to oscillations in the corresponding sheet strength. These oscillations have a frequency corresponding to approximately half the orbital frequency of the points along the interface. By using geometric arguments, we derived an analytical expression for the multivalue time, i.e., the time at which the slope of the interface first becomes vertical, which agrees well with our vortex-sheet simulations. In the case of small Atwood numbers, the evolution of the vorticity distribution is additionally affected by the local tangential acceleration and nonlinear vorticity advection along the interface. After a time proportional to the multivalue time, these two additional mechanisms lead to the generation of opposite-sign vorticity between the bubble and spike. When varying the strength of the incident shock (measured by the shock Mach number M_s) and the density ratio (measured by the Atwood number A), the emergence of opposite-sign vorticity is delayed for low-Atwood numbers ($A \lesssim 0.2$) and low-Mach numbers ($M_s \lesssim 0.2$); the corresponding amount of opposite-sign circulation is the lowest for these Mach and Atwood numbers. In contrast, the amount of opposite-sign circulation is the largest for $A \gtrsim 0.6$ and $M_s \gtrsim 4$. When only varying the shock Mach number but keeping the Atwood number fixed, the interface behavior scales in time with respect to the shock Mach number, such that the latter simply acts as a time scaling in the evolution of the interface. This behavior

results in opposite-sign vorticity to develop at the same time (scaled with the initial sheet strength) for all shock Mach numbers, and to behave according to a power law in time.

In Appendix C, we further provide insights into the vorticity deposition on finite-size perturbations, relevant to the study of reshock for the RM instability. We extended current vorticity-deposition models to arbitrary perturbation amplitude, by extracting the interface morphology and vorticity distribution from direct simulations of the Euler equations. In a light-to-heavy configuration, increasing the amplitude of the initial perturbation results in a narrower vorticity distribution compared to that of a small initial perturbation. In a heavy-to light configuration, the interface morphology after shock passage is significantly distorted due to a phase inversion; kinks appear in the the vorticity distribution close to the bubble.

5.2 Recommendations for future research directions

The research presented in this work can be extended in several directions, which we suggest here.

5.2.1 Improvements of the numerics

The presence of the non-linear, Burgers-like term in the governing equation of the sheet strength (Eq. 2.32) requires the use of conservative numerical schemes to avoid spurious oscillations. As of now, we employ the first-order Godunov method to discretize this term. A second-order accurate method, such as Monotonic Upstream-centered Scheme for Conservation Laws (MUSCL), could be readily implemented into the current code. Higher-order accurate methods, such as Weighted Essentially Non-Oscillatory (WENO), can also be considered. Using high-order schemes for non-linear advection would enable the sharp peaks in the sheet-strength profile to not be smoothed by the use of first-order schemes. Further-

more, the approximation of the Biot-Savart integral (Eq. 2.31) with the mid-point rule can be improved by using a higher-order accurate method, such as a Gaussian quadrature. This improvement would be useful in three dimensions if triangular mesh elements are used.

5.2.2 Extensions of the vortex-sheet model

The current vortex-sheet model simulates the evolution of interfacial perturbations in incompressible and inviscid fluids, with no surface tension, i.e., continuity of pressure at the interface. Although we have considered gas/gas interfaces, where the effect of surface tension may be neglected, this assumption may not be justifiable for other type of interfaces, e.g., gas/liquid interfaces. It is straightforward to incorporate a surface-tension term in Eq. 2.32, by evaluating the pressure jump across the interface with the local curvature. Furthermore, the current model relies on the assumption that the vorticity is infinite at the sheet. This assumption can be relaxed by considering a small but finite-thickness layer in which vorticity is allowed to diffuse. Such a scenario would provide a more realistic description of roll-up formation at late times. The vortex sheet becomes a vortex layer, whose evolution can be determined by the method of asymptotic matching, where the flow inside the layer is matched to the flow outside the layer (Moore, 1978). Another study that considered the evolution of vortex layers is by Pozrikidis & Higdon (1985), who considered initial perturbations on the boundaries of a shear layer to simulate the evolution of the Kelvin-Helmholtz instability. Furthermore, in the context of HED physics, where electric and magnetic fields affect the behavior of the pure hydrodynamics, the vortex-sheet model can be further extended to include additional vorticity production from external body forces, e.g., a magnetic field.

The current code capabilities can be extended to three-dimensional vortex sheets (Pozrikidis, 2000; Stock *et al.*, 2008). The main difference in terms of the governing equations lies in the additional vortex-stretching term, as seen in Eq. 2.26. Another important difference from the two-dimensional case is the fact that the sheet strength is a two-component vector, which lies in the plane tangential to the sheet.

5.2.3 Transient initial conditions

As illustrated in this thesis, the determination of the vortex-sheet initial conditions for RM-type problems can be challenging if the perturbation evolves during its interaction with the incident shock. In Appendix C, we discovered that, after the shock has traversed the interface, the morphology of the interface can be convoluted, especially when a phase inversion occurs. In such cases, even our extraction algorithm, introduced in the same appendix, is limited by the resolution of the direct simulations. An alternative could be to develop a technique in which the vortex sheet evolves as the shock is still traversing the initial perturbation. Doing so would avoid the need to determine the interface morphology and the corresponding sheet-strength distribution immediately after shock passage.

5.2.4 Arbitrary geometries and pressure waves

The results presented in the present research were obtained for single-mode initial perturbations in an RM environment. However, in practical applications such as inertial confinement fusion, target imperfections typically contain more than one mode, even a full spectrum of modes, which interact with each other in the non-linear regime of perturbation growth. Therefore, the current vortex-sheet model may be extended to simulate such cases. Here again, the initial conditions are the limitation. However, a first step would be to apply the model of Samtaney & Zabusky (1994) by determining the local angle between the initial perturbation and the incident shock. Next, using my extraction algorithm, the vorticity distribution would be obtained from a given initial mode spectrum.

The case of multimode perturbations provides further motivation to consider the evolution of vortex sheets with arbitrary shapes. A step further would be to consider the vorticity distribution originating from arbitrary pressure waves, e.g., rarefactions, acoustic waves, etc., interacting with interfaces. This extension of the vortex-sheet model would allow the study of general pressure-wave-interface interaction problems, e.g., the role of vorticity dynamics

in cavitation bubble collapse induced by acoustic waves (Shpuntova *et al.*, 2021).

5.2.5 Parallelization and high-performance computing

In order to be able to capture the intricate roll-up morphology of the vortex core at late times, sufficient spatial resolution is required, which can be achieved with a point-insertion procedure. However, since the number of points increases over time, the run-time of the simulations can be significantly long, especially in three dimensions. This aspect provides motivation for extending the code capabilities to run simulations in parallel with multiple CPUs/GPUs on supercomputers.

Appendices

Appendix A

Derivation of the Sheet-Strength Governing Equation

A.1 The three-dimensional case

A.1.1 Kinematics only

Using Eq. 2.23, we have, for the + side

$$\begin{aligned}
\frac{\partial \boldsymbol{u}^{+}}{\partial t} + \left(\boldsymbol{u}^{+} \cdot \nabla\right) \boldsymbol{u}^{+} &= 0 \\
\frac{\partial \boldsymbol{u}^{\mathrm{vs}}}{\partial t} - \frac{1}{2}\frac{\partial \boldsymbol{\Delta u}}{\partial t} + \left(\boldsymbol{u}^{+} \cdot \nabla\right) \boldsymbol{u}^{\mathrm{vs}} - \frac{1}{2}\left(\boldsymbol{u}^{+} \cdot \nabla\right) \Delta \boldsymbol{u} &= 0 \\
\frac{\partial \boldsymbol{u}^{\mathrm{vs}}}{\partial t} - \frac{1}{2}\frac{\partial \boldsymbol{\Delta u}}{\partial t} + \left(\boldsymbol{u}^{\mathrm{vs}} \cdot \nabla\right) \boldsymbol{u}^{\mathrm{vs}} - \frac{1}{2}\left(\Delta \boldsymbol{u} \cdot \nabla\right) \boldsymbol{u}^{\mathrm{vs}} - \frac{1}{2}\left(\boldsymbol{u}^{\mathrm{vs}} \cdot \nabla\right) \Delta \boldsymbol{u} + \frac{1}{4}\left(\Delta \boldsymbol{u} \cdot \nabla\right) \Delta \boldsymbol{u} &= 0.
\end{aligned} \tag{A.1}$$

Defining the total derivative with respect to the vortex-sheet velocity

$$\frac{D(\cdot)}{Dt} = \frac{\partial(\cdot)}{\partial t} + \left(\boldsymbol{u}^{\mathrm{vs}} \cdot \nabla\right)(\cdot), \tag{A.2}$$

we have

$$\frac{D\boldsymbol{u}^{\mathrm{vs}}}{Dt} - \frac{1}{2}\frac{D\Delta \boldsymbol{u}}{Dt} - \frac{1}{2}\left(\Delta \boldsymbol{u} \cdot \nabla\right) \boldsymbol{u}^{\mathrm{vs}} + \frac{1}{4}\left(\Delta \boldsymbol{u} \cdot \nabla\right) \Delta \boldsymbol{u} = 0. \tag{A.3}$$

Doing the same operations on the other side (side $-$) we obtain

$$\frac{D\boldsymbol{u}^{\text{vs}}}{Dt} + \frac{1}{2}\frac{D\Delta\boldsymbol{u}}{Dt} + \frac{1}{2}\left(\Delta\boldsymbol{u}\cdot\nabla\right)\boldsymbol{u}^{\text{vs}} + \frac{1}{4}\left(\Delta\boldsymbol{u}\cdot\nabla\right)\Delta\boldsymbol{u} = 0. \tag{A.4}$$

Taking the difference between Eqs. A.3 and A.4 leads to

$$\frac{D\Delta\boldsymbol{u}}{Dt} = -\left(\Delta\boldsymbol{u}\cdot\nabla\right)\boldsymbol{u}^{\text{vs}}. \tag{A.5}$$

To relate this expression to the sheet strength $\boldsymbol{\zeta}$, we take the cross product of $\hat{\boldsymbol{N}}$ with Eq. A.5

$$\hat{\boldsymbol{N}}\times\frac{D\Delta\boldsymbol{u}}{Dt} = -\hat{\boldsymbol{N}}\times\left[\left(\Delta\boldsymbol{u}\cdot\nabla\right)\boldsymbol{u}^{\text{vs}}\right]. \tag{A.6}$$

Following Stock (2006), it can be shown that

$$\hat{\boldsymbol{N}}\times\frac{D\Delta\boldsymbol{u}}{Dt} = \frac{D\boldsymbol{\zeta}}{Dt} + \hat{\boldsymbol{N}}\left(\boldsymbol{\zeta}\cdot\frac{D\hat{\boldsymbol{N}}}{Dt}\right), \tag{A.7}$$

such that

$$\frac{D\boldsymbol{\zeta}}{Dt} = -\hat{\boldsymbol{N}}\left(\boldsymbol{\zeta}\cdot\frac{D\hat{\boldsymbol{N}}}{Dt}\right) - \hat{\boldsymbol{N}}\times\left[\left(\Delta\boldsymbol{u}\cdot\nabla\right)\boldsymbol{u}^{vs}\right]. \tag{A.8}$$

Further simplifications lead to Eq. 2.25.

A.1.2 Addition of baroclinic terms

The Euler equations on the $+$ side are now (from Eq. A.3)

$$\rho^{+}\frac{D\boldsymbol{u}^{\text{vs}}}{Dt} - \frac{1}{2}\rho^{+}\frac{D\Delta\boldsymbol{u}}{Dt} - \frac{1}{2}\rho^{+}\left(\Delta\boldsymbol{u}\cdot\nabla\right)\boldsymbol{u}^{\text{vs}} + \frac{1}{4}\rho^{+}\left(\Delta\boldsymbol{u}\cdot\nabla\right)\Delta\boldsymbol{u} = \rho^{+}\boldsymbol{g} - \nabla p^{+}. \tag{A.9}$$

On the other side, they are

$$\rho^{-}\frac{D\boldsymbol{u}^{\mathrm{vs}}}{Dt}+\frac{1}{2}\rho^{-}\frac{D\Delta\boldsymbol{u}}{Dt}+\frac{1}{2}\rho^{-}\left(\Delta\boldsymbol{u}\cdot\nabla\right)\boldsymbol{u}^{\mathrm{vs}}+\frac{1}{4}\rho^{-}\left(\Delta\boldsymbol{u}\cdot\nabla\right)\Delta\boldsymbol{u}=\rho^{-}\boldsymbol{g}-\nabla p^{-}. \tag{A.10}$$

Taking the difference between these two equations leads to

$$\begin{aligned}\left(\rho^{+}-\rho^{-}\right)\frac{D\boldsymbol{u}^{\mathrm{vs}}}{Dt}-\frac{1}{2}\left(\rho^{+}+\rho^{-}\right)\frac{D\Delta\boldsymbol{u}}{Dt}-\frac{1}{2}\left(\rho^{+}+\rho^{-}\right)\left(\Delta\boldsymbol{u}\cdot\nabla\right)\boldsymbol{u}^{\mathrm{vs}}+\\ \frac{1}{4}\left(\rho^{+}-\rho^{-}\right)\left(\Delta\boldsymbol{u}\cdot\nabla\right)\Delta\boldsymbol{u}=\left(\rho^{+}-\rho^{-}\right)\boldsymbol{g}-\nabla\left(p^{+}-p^{-}\right).\end{aligned} \tag{A.11}$$

The Atwood number being $A=(\rho^{-}-\rho^{+})/(\rho^{+}+\rho^{-})$, we have

$$\frac{D\Delta\boldsymbol{u}}{Dt}=-\left(\Delta\boldsymbol{u}\cdot\nabla\right)\boldsymbol{u}^{\mathrm{vs}}-2A\left(\frac{D\boldsymbol{u}^{\mathrm{vs}}}{Dt}+\frac{1}{4}\left(\Delta\boldsymbol{u}\cdot\nabla\right)\Delta\boldsymbol{u}-\boldsymbol{g}\right)+\frac{2}{\rho^{+}+\rho^{-}}\nabla\left(p^{+}-p^{-}\right). \tag{A.12}$$

If we define the average fluid acceleration on each side of the sheet, $\bar{\boldsymbol{a}}$, as

$$\bar{\boldsymbol{a}}\equiv\frac{1}{2}\left(\left.\frac{D\boldsymbol{u}^{+}}{Dt}\right|_{\mathrm{fluid}}+\left.\frac{D\boldsymbol{u}^{-}}{Dt}\right|_{\mathrm{fluid}}\right), \tag{A.13}$$

where $\left.\frac{D\cdot}{Dt}\right|_{\mathrm{fluid}}$ is the total derivative with respect to the fluid velocity (not the sheet velocity), i.e.,

$$\left.\frac{D(\cdot)}{Dt}\right|_{\mathrm{fluid}}=\frac{\partial(\cdot)}{\partial t}+(\boldsymbol{u}^{\pm}\cdot\nabla)(\cdot), \tag{A.14}$$

then we can show, using Eq. 2.23, that

$$\bar{\boldsymbol{a}}=\frac{D\boldsymbol{u}^{\mathrm{vs}}}{Dt}+\frac{1}{4}\left(\Delta\boldsymbol{u}\cdot\nabla\right)\Delta\boldsymbol{u}. \tag{A.15}$$

Therefore, Eq. A.12 can be written as

$$\frac{D\Delta\boldsymbol{u}}{Dt} = -\left(\Delta\boldsymbol{u}\cdot\nabla\right)\boldsymbol{u}^{\mathrm{vs}} - 2A\left(\bar{\boldsymbol{a}}-\boldsymbol{g}\right) + \frac{2}{\rho^{+}+\rho^{-}}\nabla\left(p^{+}-p^{-}\right). \tag{A.16}$$

As before, we relate that equation to the sheet strength by taking its cross product with the normal vector

$$\hat{\boldsymbol{N}}\times\frac{D\Delta\boldsymbol{u}}{Dt} = -\hat{\boldsymbol{N}}\times\left[\left(\Delta\boldsymbol{u}\cdot\nabla\right)\boldsymbol{u}^{\mathrm{vs}}\right] - 2A\;\hat{\boldsymbol{N}}\times\left(\bar{\boldsymbol{a}}-\boldsymbol{g}\right) + \frac{2}{\rho^{+}+\rho^{-}}\;\hat{\boldsymbol{N}}\times\nabla\left(p^{+}-p^{-}\right). \tag{A.17}$$

We already simplified the left-hand-side and the first term on the right-hand-side (Eqs. A.6 and 2.25), which leads to Eq. 2.26.

A.2 The two-dimensional case

We start from the equation governing the jump in velocity, Eq. A.12. In two dimensions, the velocity jump is $\Delta\boldsymbol{u} = \gamma\hat{\boldsymbol{T}}$, such that, when substituted in Eq. A.12, we have

$$\frac{D(\gamma\hat{\boldsymbol{T}})}{Dt} = -\left(\gamma\hat{\boldsymbol{T}}\cdot\nabla\right)\boldsymbol{u}^{\mathrm{vs}} - 2A\left(\frac{D\boldsymbol{u}^{\mathrm{vs}}}{Dt} + \frac{1}{4}\left(\gamma\hat{\boldsymbol{T}}\cdot\nabla\right)\gamma\hat{\boldsymbol{T}} - \boldsymbol{g}\right) + \frac{2}{\rho^{+}+\rho^{-}}\nabla\left(p^{+}-p^{-}\right). \tag{A.18}$$

Since we want an evolution equation for γ only, we project onto the tangential direction. Evaluating each term separately, the left-hand side can be written as

$$\frac{D(\gamma\hat{\boldsymbol{T}})}{Dt}\cdot\hat{\boldsymbol{T}} = \left(\frac{D\gamma}{Dt}\hat{\boldsymbol{T}} + \gamma\frac{D\hat{\boldsymbol{T}}}{Dt}\right)\cdot\hat{\boldsymbol{T}} = \frac{D\gamma}{Dt} + \hat{\boldsymbol{T}}\cdot\gamma\frac{D\hat{\boldsymbol{T}}}{Dt} \tag{A.19}$$

The rate of change of the tangential vector can be given by

$$\frac{D\hat{\boldsymbol{T}}}{Dt} = (\hat{\boldsymbol{T}}\cdot\nabla\boldsymbol{u})\cdot(\boldsymbol{I}-\hat{\boldsymbol{T}}\otimes\hat{\boldsymbol{T}}), \tag{A.20}$$

where $\nabla \boldsymbol{u}$ is the velocity gradient tensor, and $\boldsymbol{I}$ the identity matrix. The operator $(\boldsymbol{I}-\hat{\boldsymbol{T}}\otimes\hat{\boldsymbol{T}})$ removes the tangential component of a multiplying vector, hence $D\hat{\boldsymbol{T}}/Dt$ lies in a plane normal to the tangential direction. Therefore, when projecting onto the tangential direction, we have

$$\hat{\boldsymbol{T}} \cdot \frac{D\hat{\boldsymbol{T}}}{Dt} = 0. \tag{A.21}$$

The first term on the right-hand side can be written as

$$\hat{\boldsymbol{T}} \cdot \left(\gamma\hat{\boldsymbol{T}} \cdot \nabla\right) \boldsymbol{u}^{\text{vs}} = \hat{\boldsymbol{T}} \cdot \gamma(\hat{\boldsymbol{T}} \cdot \nabla)\boldsymbol{u}^{\text{vs}} = \hat{\boldsymbol{T}} \cdot \gamma\frac{\partial \boldsymbol{u}^{\text{vs}}}{\partial s}, \tag{A.22}$$

where $(\hat{\boldsymbol{T}} \cdot \nabla)(\cdot) = \dfrac{\partial(\cdot)}{\partial s}$ is the directional derivative in the direction of the tangential vector. The third term on the right-hand side can be written as

$$\hat{\boldsymbol{T}} \cdot \left(\gamma\hat{\boldsymbol{T}} \cdot \nabla\right) \gamma\hat{\boldsymbol{T}} = \hat{\boldsymbol{T}} \cdot \gamma \left(\hat{\boldsymbol{T}} \cdot \nabla\right) \gamma\hat{\boldsymbol{T}} = \hat{\boldsymbol{T}} \cdot \gamma\frac{\partial(\gamma\hat{\boldsymbol{T}})}{\partial s} = \hat{\boldsymbol{T}} \cdot \gamma \left(\frac{\partial\gamma}{\partial s}\hat{\boldsymbol{T}} + \gamma\frac{\partial\hat{\boldsymbol{T}}}{\partial s}\right) = \gamma\frac{\partial\gamma}{\partial s}, \tag{A.23}$$

where we have used the fact that $\hat{\boldsymbol{T}} \cdot \dfrac{\partial\hat{\boldsymbol{T}}}{\partial s} = 0$. Substituting everything back into Eq. A.18 and rearranging, we obtain

$$\frac{D\gamma}{Dt} = -\gamma\frac{\partial \boldsymbol{u}^{\text{vs}}}{\partial s} \cdot \hat{\boldsymbol{T}} - 2A \left(\frac{D\boldsymbol{u}^{\text{vs}}}{Dt} \cdot \hat{\boldsymbol{T}} + \frac{1}{4}\gamma\frac{\partial\gamma}{\partial s} - \boldsymbol{g} \cdot \hat{\boldsymbol{T}}\right) + \frac{2}{\rho^+ + \rho^-}\nabla\left(p^+ - p^-\right) \cdot \hat{\boldsymbol{T}}. \tag{A.24}$$

If there is a jump in pressure across the vortex sheet, e.g., due to surface tension, the pressure difference, $\Delta p \equiv p^+ - p^-$, can be written as

$$\Delta p = \sigma\kappa, \tag{A.25}$$

where σ is the surface tension (assumed constant), and κ the interface curvature. In that case, the surface tension term in Eq. A.24 can be re-written as

$$\nabla(\Delta p)\cdot\hat{\boldsymbol{T}} = (\hat{\boldsymbol{T}}\cdot\nabla)\Delta p = \frac{\partial \Delta p}{\partial s} = \sigma\frac{\partial \kappa}{\partial s}. \tag{A.26}$$

Therefore, a non-dimensional form of Eq. 2.29 is given by

$$\frac{D\tilde{\gamma}}{D\tilde{t}} = -\tilde{\gamma}\frac{\partial \tilde{\boldsymbol{u}}^{\mathrm{vs}}}{\partial \tilde{s}}\cdot\hat{\boldsymbol{T}} - 2A\left(\bar{\tilde{\boldsymbol{a}}} - \frac{1}{\mathrm{Fr}^2}\tilde{\boldsymbol{g}}\right)\cdot\hat{\boldsymbol{T}} + \frac{2}{\mathrm{We}}\frac{\partial \tilde{\kappa}}{\partial \tilde{s}}, \tag{A.27}$$

where the Weber number is defined as

$$\mathrm{We} = \frac{(\rho^+ + \rho^-)V^2 L}{\sigma}, \tag{A.28}$$

and represents the importance of inertia relative to surface tension.

Appendix B

Single-mode Richtmyer-Meshkov instability

We compare our vortex-sheet model against the RM experiments of Di Stefano *et al.* (2019), along with the corresponding two-dimensional xRAGE simulations with a laser model (Marozas *et al.*, 2018; Haines *et al.*, 2016). The experimental conditions of Di Stefano *et al.* (2019) are the same as those considered in the current work, with an initial tilt angle $\theta = 0°$. Since the laser-turn-off conditions are the same, early RM growth is followed by RT growth once the rarefaction reaches the interface.

Fig. B.1 compares the time evolution of the perturbation amplitude obtained with the vortex-sheet model (with and without laser-induced deceleration and decompression) to the experiments and the xRAGE simulations. Both vortex-sheet solutions give similar results until $t \approx 5$ ns, at which point the rarefaction produced by laser turn-off reaches the interface. When not accounting for this deceleration, the vortex-sheet solution predicts a saturation of the growth, contrary to the experiments and the simulations. When accounting for the laser-induced deceleration and interface decompression, reasonable agreement with the late-time behavior predicted by the xRAGE simulations is achieved. The overprediction of the vortex-sheet solution accounting for laser-induced effects (red curve) may come from a slight overprediction of the total circulation at the time at which the shock leaves the interface. The total circulation may be affected by additional vorticity along the transmitted shock, thus slightly overpredicting the initial growth rate.

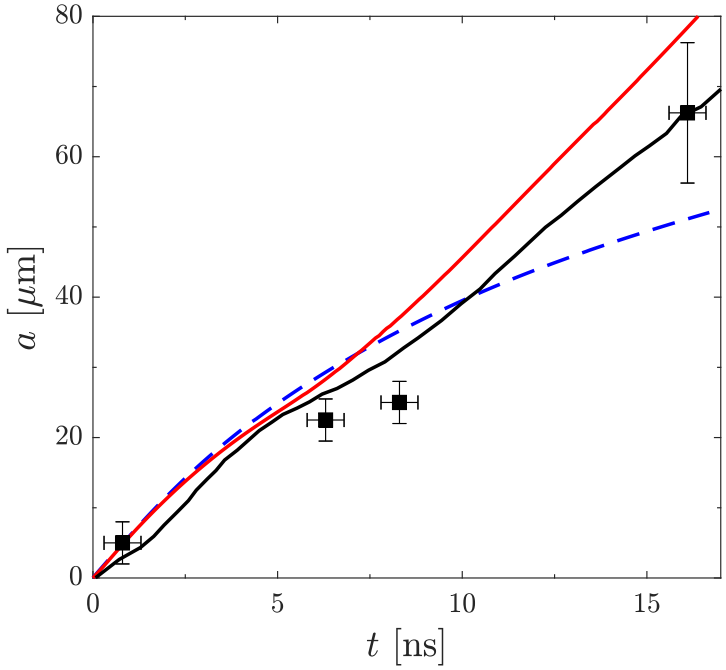

Figure B.1: Time evolution of the perturbation amplitude obtained from the vortex sheet, without laser-induced deceleration or decompression due to laser turn-off (- - -), with both deceleration and decompression (—), the experiments (■), and xRAGE simulations (Di Stefano *et al.*, 2019) (—).

Appendix C

Vorticity Dynamics of Finite-Amplitude Perturbation in the Richtmyer-Meshkov Instability

C.1 Introduction

Perturbations on an interface separating two materials of different densities grow under the influence of an impacting shock wave, due to the baroclinic vorticity generated along the interface. Such an interaction is known as the Richtmyer–Meshkov instability (Richtmyer (1960); Meshkov (1969)), and occurs both in nature and in engineering applications, such as supernovae collapse (Kane *et al.* (1997)) and inertial confinement fusion (Betti & Hurricane (2016)).

The Richtmyer–Meshkov instability (RM) can be described as consisting of four main stages (Zabusky (1999)): a first vorticity-deposition stage where baroclinic vorticity is generated along the interface by the shock passage, an early stage where the growth is linear in time, an intermediate stage where the growth saturates due to nonlinearities, and a late stage where the flow may become turbulent. In this work we focus on the first three stages. In the early stage, baroclinic vorticity is deposited along the interface due to the misalignment between the pressure gradient across the shock, and the density gradient across the interface (Brouillette (2002)). After the shock passage, the resulting vortex sheet along the interface dictates the flow behavior in the linear and non-linear regimes. Previous studies have shown that in the non-linear regime additional vorticity may further be generated. For

example, studies of RM experiments performed in shock tubes have observed a phenomenon called "reshock", where shocks reflected from the tube boundaries interact a second time with the interface (Balasubramanian *et al.* (2012); Latini *et al.* (2007*b*); McFarland *et al.* (2014)). In high-energy-density experiments, where finite-pulse lasers are used to produce shocks, rarefactions originating from laser turn-off also interact with the interface well after the primary shock has traversed the initial interface (Di Stefano *et al.* (2019); Rasmus *et al.* (2019)).

The evolution of the vorticity dynamics can be difficult to measure and understand from direct simulations or laboratory experiments. Thus, models directly representing the vorticity evolution can provide insights into these flows. Given an initial distribution of vorticity, its evolution is readily determined by solving the vorticity equation, e.g., using a point vortex model (Jacobs & Sheeley (1996)) or a vortex-sheet model (Matsuoka *et al.* (2003); Matsuoka & Nishihara (2006*c*)). Therefore, the performance of these models relies on a correct determination of the vorticity-deposition stage.

In the case of a small initial perturbation relative to its wavelength, the initial vorticity distribution may be determined by using a velocity potential ansatz, as previously suggested by Jacobs & Sheeley (1996) and Sohn (2004). A more sophisticated approach was developed by Samtaney & Zabusky (1994) (SZ), who considered shock-polar analysis to determine the initial distribution of the circulation per unit length of a perturbed interface. They showed that the circulation per unit length depends on the material properties, the shock strength, the pressure ratios across the waves originating from shock refraction, and the geometry of the interface. If the perturbation amplitude is sufficiently small, changes in the interface geometry due to the shock passage are negligible. However, for a finite-size amplitude perturbation, none of these models can describe the vorticity distribution immediately after the shock passage.

The goal of this work is to understand the role of vorticity dynamics in the evolution of finite-size perturbations subjected to a shock wave. We first present the governing equations

of the vortex sheet model followed by a description of the SZ model and a novel technique in the initialization of vortex sheets. Next, we validate our current technique in the case of small amplitude perturbation against the SZ model. After that, we apply our technique to finite-amplitude perturbations in light/heavy and heavy/light configurations. Finally, we show results of the interface evolution for two cases of finite amplitude perturbations.

C.2 Vortex sheet initialization for the Richtmyer–Meshkov instability

The initial conditions of the vortex-sheet model require the initial location of the interface $\boldsymbol{x} = (x, y)$ and the distribution of the sheet strength γ immediately after the shock has finished traversing the interface. In the case of infinitesimal perturbation amplitudes, the model of Samtaney & Zabusky (1994) can be used to determine the sheet-strength distribution, and was presented in Chapter 2. However, this model breaks down when the size of the perturbation is finite.

Our goal is to initialize the vortex sheet model by prescribing the vortex-sheet strength, $\gamma = (\boldsymbol{u}^- - \boldsymbol{u}^+) \cdot \hat{\boldsymbol{T}}$, along the appropriate interface morphology at the time when the shock ends its interaction with the interface, for arbitrary shock strength and perturbation amplitude. To do so, we conduct direct simulations of the Euler equations until that time, and extract the interface morphology and vorticity distribution from those datasets. The interface morphology is constructed by identifying the jump in tangential velocity, while the sheet strength is determined based on this jump according to the definition of the sheet strength. The algorithm we use to initialize the vortex sheet model is illustrated in Fig. C.1. Again, the purpose is to identify the initial interface morphology and the corresponding sheet strength.

As a first estimate, we identify the interface location from the volume fraction field $v_f(x, y)$. The interface location (x_i, y_i) is obtained by interpolating the position where $v_f =$

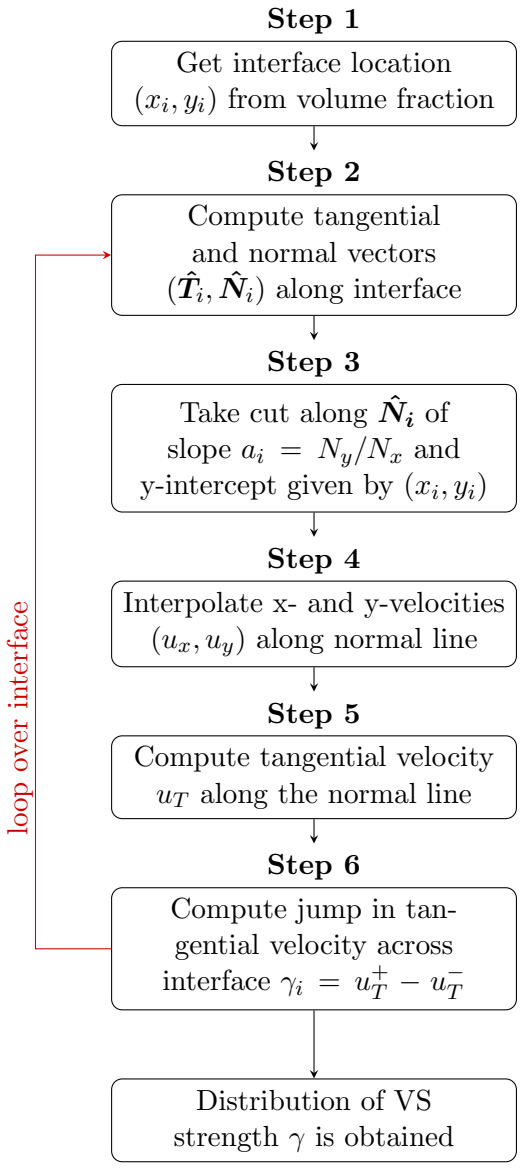

Figure C.1: Flowchart of the extraction algorithm for the location of the interface and sheet-strength distribution after shock passage

0.5.

Next, the tangential and normal vectors $\hat{\boldsymbol{T}}_i$ and $\hat{\boldsymbol{N}}_i$ are computed at any point along the interface. The tangential vector is defined as

$$\hat{\boldsymbol{T}}_i = \frac{\dot{\boldsymbol{r}}_i}{|\dot{\boldsymbol{r}}_i|} = \left(\frac{d\boldsymbol{r}}{ds}\right)_i, \tag{C.1}$$

where $\boldsymbol{r}_i$ is a parametrization of the interface with respect to a parameter α_i such that $\boldsymbol{r}_i = (x(\alpha_i), y(\alpha_i))$ and the dot notation refers to the derivative with respect to α, $\dot{\boldsymbol{r}} = d\boldsymbol{r}/d\alpha$. The normal vector is defined as

$$\hat{\boldsymbol{N}}_i = \frac{1}{\kappa_i}\frac{d\hat{\boldsymbol{T}}_i}{ds}, \tag{C.2}$$

where κ_i is the curvature of the interface at point i given by

$$\kappa_i = \left|\frac{d\hat{\boldsymbol{T}}_i}{ds}\right|. \tag{C.3}$$

In the following step, the velocity vector is interpolated along the interface. For this purpose, we take a cut (referred to as the normal line) in the direction defined by the normal vector $\hat{\boldsymbol{N}}_i$ along the interface. The normal line has a slope $a_i = (N_y/N_x)_i$ and the y-intercept is given by the point (x_i, y_i).

We then interpolate the x- and y-components of the velocity $(u_x, u_y)_j$ along the normal line from the velocity field. Note that the index j refers to the normal line, not the interface.

Then, the tangential velocity $(u_T)_j$ component is computed along the normal line. From the values (u_x, u_y) in the coordinate system (x, y), the value of $(u_T)_j$ is obtained by coordinate transformation as

$$(u_T)_j = (u_x)_j \cos\theta + (u_y)_j \sin\theta, \tag{C.4}$$

where θ is the angle between the unit vectors $\hat{\boldsymbol{x}}$ and $\hat{\boldsymbol{T}}$.

Next, the jump in the tangential velocity u_T across the interface is computed. As an example, Fig. C.2 shows the tangential velocity u_T as a function of the normal direction.

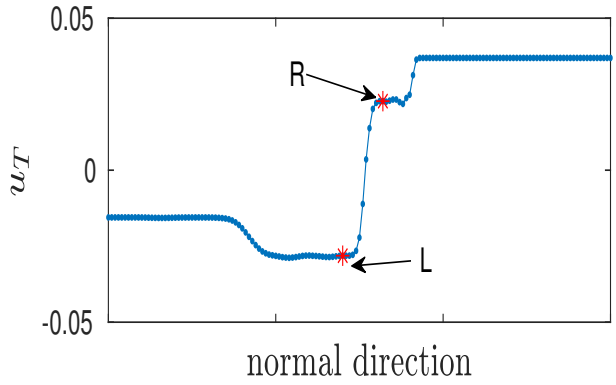

Figure C.2: Tangential velocity as a function of the normal direction at the point (x_i, y_i).

The jump is taken as the difference between the two values designated by the red stars R and L. These values correspond to the right and left of the vorticity peak, respectively (see bottom of figure C.3). This choice comes from the observation that the vorticity field after shock passage is concentrated in a thin layer around the interface (see top of figure C.3). From this definition of the jump, a value of the VS strength at the point (x_i, y_i) is obtained $\gamma_i = u_T^+ - u_T^-$.

These steps are repeated to obtain a more accurate interface location and strength distribution.

To verify our algorithm, we consider the experiments of Collins & Jacobs (2002), who investigated single-mode Richtmyer-Meshkov instability at an interface between air ($\rho_{air} = 1.351\text{kg/m}^3$, $\kappa_{air} = 1.276$) and SF6 ($\rho_{SF6} = 5.494\text{kg/m}^3$, $\kappa_{SF6} = 1.093$) for an incident shock of Mach number $M_s = 1.21$ in air. For a small initial perturbation ($a_0/\lambda = 0.03$), Fig. C.4 shows the sheet-strength distribution along the interface based on the SZ model and our initialization algorithm. The results compare well except at the extrema of γ_0, which are the locations along the interface where the slope of the interface is maximum, with a discrepancy of approximately 6%. At these points, the normal line to the interface is the most misaligned with respect to the mesh, which introduces numerical errors when interpolating the x- and y-velocities along the normal line. Moreover, the SZ model does not take into account the change in morphology of the interface from the passage of the shock, which is another source

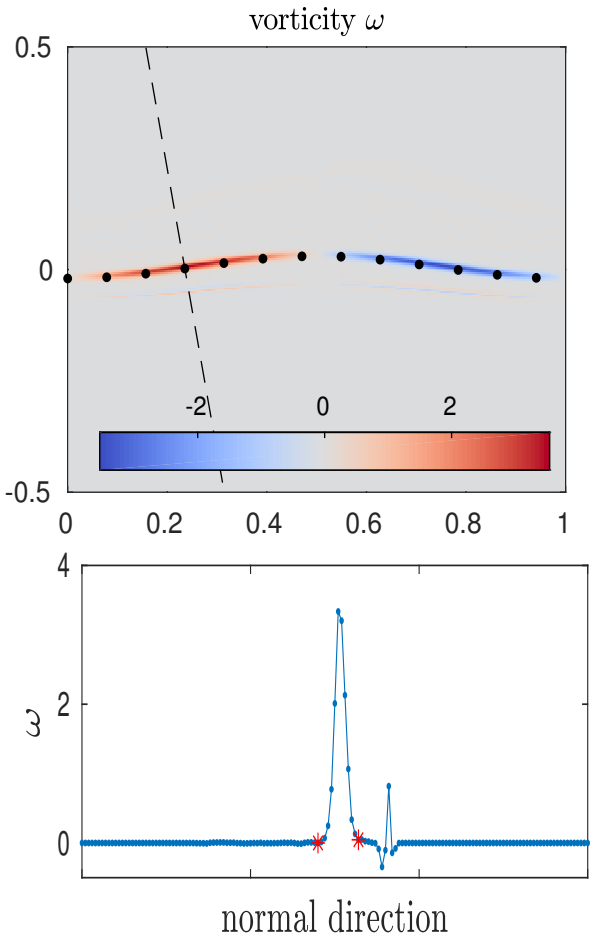

Figure C.3: Top: vorticity fields with normal line (dashed line) at a point (x_i, y_i) on the interface. Bottom: vorticity plotted along the normal line. The two red stars correspond to the width of the peak.

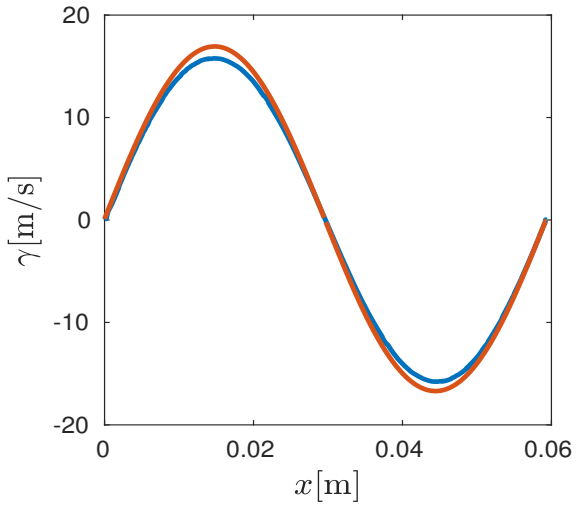

Figure C.4: Sheet-strength distribution along the interface from the SZ model (—) and the extraction algorithm (—).

of discrepancy between the two methods. Fig. C.5 compares the subsequent growth of the perturbation amplitude as a function of time for vortex sheet computations initialized using the SZ model and the current algorithm, as well as the experiments of Collins & Jacobs (2002), and the direct simulations. Overall, the agreement between the different approaches and the data is good, as the early linear growth is well represented, as is later-time saturation.

C.3 Finite-amplitude single-mode Richtmyer-Meshkov instability

In the case of a finite-amplitude initial perturbation, the interaction time between the incoming shock and the interface is not small compared to the evolution of the perturbation. As a consequence, the deposition of vorticity cannot be assumed to occur instantaneously, such that the change in the morphology of the interface while the shock is traversing it cannot be neglected. Furthermore, as the perturbation amplitude is increased, a complex system of waves emerges from shock refraction at the interface (Mach stems, irregular refractions, etc), which the SZ model cannot represent. In this section, we investigate the

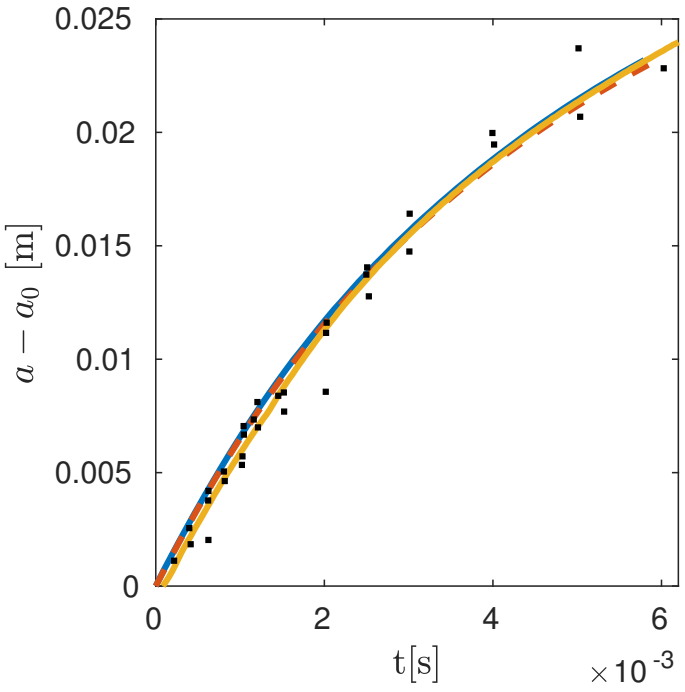

Figure C.5: Amplitude vs. time from the experiments of Collins & Jacobs (2002) (■), the direct simulations (—), the vortex sheet using the SZ model (- - -), and the vortex sheet using the algorithm (—)

vorticity-deposition phase and the subsequent vorticity evolution for four finite-amplitude perturbations: $a_0/\lambda = 0.05,\ 0.1,\ 0.2,\ 0.3$. We consider both light-to-heavy and heavy-to-light configuration; in the latter, phase inversion occurs.

C.3.1 Light-to-heavy configuration

Fig. C.6 shows the evolution of the perturbation during the passage of the shock across the interface for $a_0/\lambda = 0.05,\ 0.1,\ 0.2,\ 0.3$, obtained from direct simulations. The effect of the finite time over which the shock interacts with the interface is evident as a_0/λ is increased. Since the incoming shock travels from a light fluid to a heavy fluid, both transmitted and reflected waves are shocks as well. Due to the acoustic impedance mismatch at the interface, the transmitted shock travels more slowly than the incoming shock, such that vorticity is first deposited by the incoming shock and then deposited by the transmitted shock. As a_0/λ is increased, the shock refraction becomes more complex, such that secondary transmitted

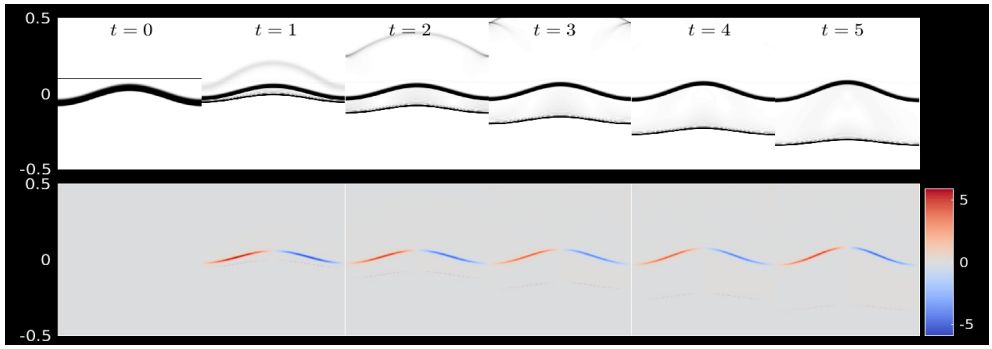

(a) $a_0/\lambda = 0.05$

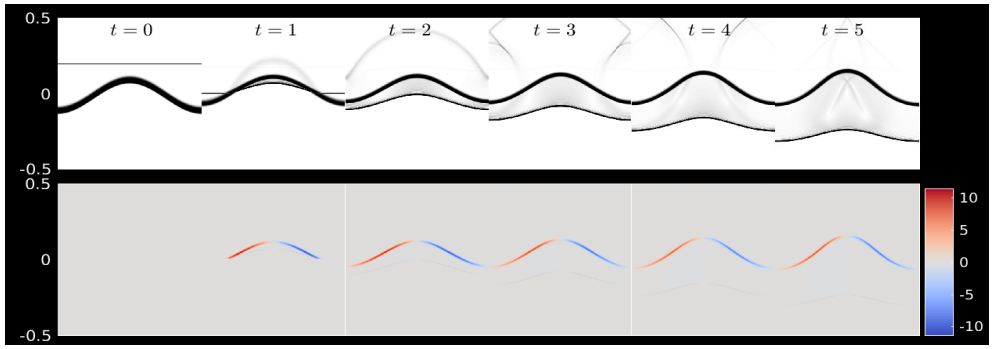

(b) $a_0/\lambda = 0.1$

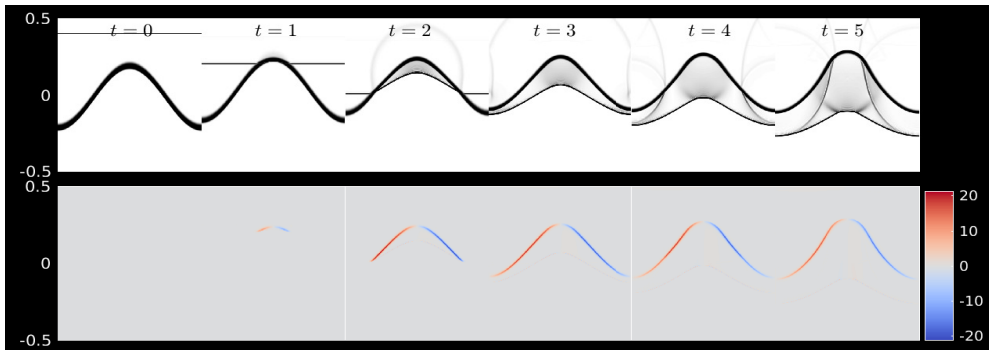

(c) $a_0/\lambda = 0.2$

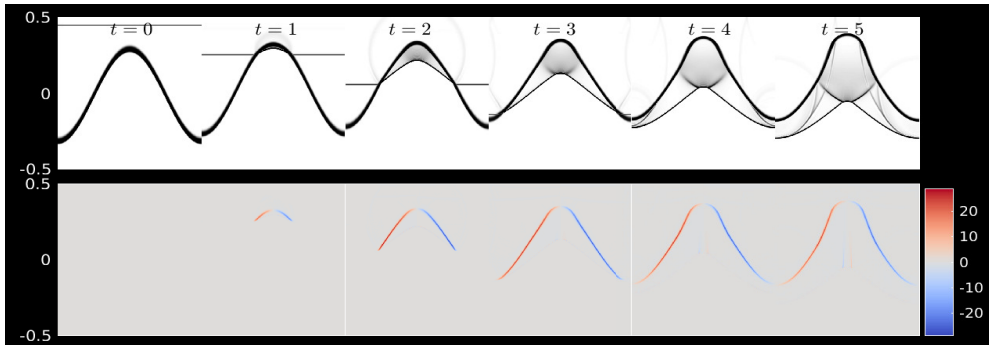

(d) $a_0/\lambda = 0.3$

Figure C.6: Evolution of the perturbation during the interaction with the incoming shock for a light/heavy configuration: (a) $a_0/\lambda = 0.05$, (b) $a_0/\lambda = 0.1$, (c) $a_0/\lambda = 0.2$, (d) $a_0/\lambda = 0.3$. Numerical Schlieren (top) and vorticity contours (bottom).

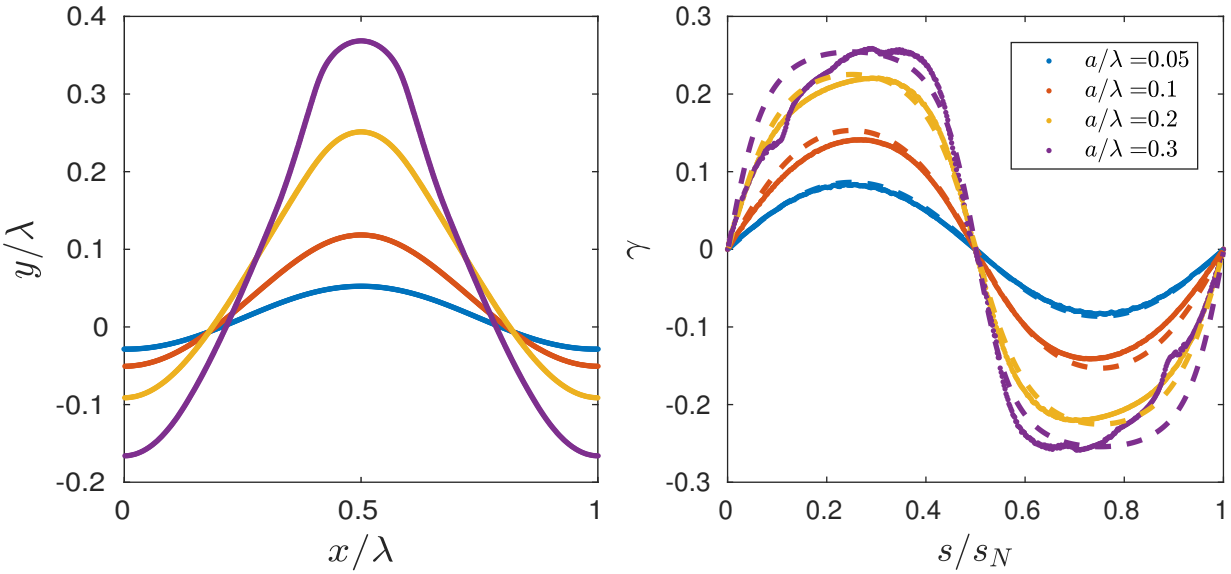

(a) Interface morphology

(b) Sheet-strength distribution

Figure C.7: (a) Interface morphology, and (b) sheet-strength distribution vs. arclength, immediately after shock passage for the light/heavy configuration for $a_0/\lambda = 0.05$ ($t = 1$), $a_0/\lambda = 0.1$ ($t = 2$), $a_0/\lambda = 0.2$ ($t = 3$), and $a_0/\lambda = 0.3$ ($t = 4$). Dashed lines: SZ model.

shocks also appear, depositing more vorticity, as shown for $a_0/\lambda = 0.2$ and $a_0/\lambda = 0.3$.

Fig. C.7a shows the interface morphology immediately after the passage of the incoming shock for the different initial amplitudes. We ignore the vorticity deposited by the secondary transmitted shocks after the incoming shock has traversed the interface, such that the time at which vorticity is extracted is $t = 1,\ 2,\ 3,\ 4$, for $a_0/\lambda = 0.05,\ 0.1,\ 0.2,\ 0.3$, respectively. As a_0/λ is increased the interface morphology loses its sinusoidal shape and the sheet-strength distribution departs from the dependence on the local angle between the interface and the incoming shock predicted by the SZ model, as illustrated in Fig. C.7b. For small initial amplitudes, the sheet-strength magnitude is similar in both the SZ model and the present calculations, but their profile differs as a_0/λ is increased; the profile is narrower in the present calculations. This discrepancy is due to the fact that the Taylor expansion of the circulation per unit length in the SZ model becomes invalid as a_0/λ is increased. As a result, the total circulation deposited along the interface from the SZ model is overpredicted, as shown in Fig. C.8. The circulation along half of the interface is computed immediately after shock passage

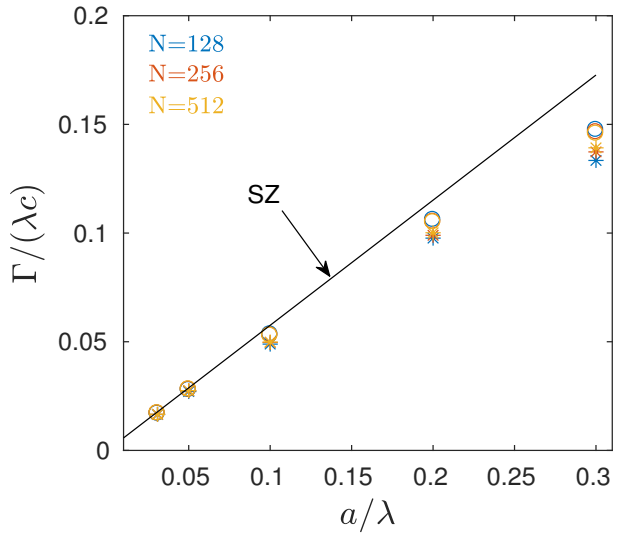

Figure C.8: Circulation along half of the interface immediately after shock passage for the light/heavy configuration for the direct simulations (○), the SZ model (—), and our algorithm (*).

from the current approach and compared to the SZ model for different initial amplitudes and grid resolutions, and that obtained from the direct simulations is also included. Both the SZ model and the present algorithm show good agreement with the direct simulations for small amplitude ($a/\lambda \lesssim 0.05$). For higher amplitudes, the proposed approach yields closer values to the direct simulations than the SZ model; the latter differs by $\sim 18\%$ while the former by $\sim 4\%$ (for $a/\lambda = 0.3$). One of the factor influencing the success of the algorithm is the mesh resolution of the direct simulations. In Fig. C.8, three different resolutions are considered for the direct simulations, which shows the convergence of the current approach to a single value of circulation as $N \to \infty$. Note that although the total circulation in the direct simulations is corrected by removing the vorticity production from transmitted and reflected waves, the discrepancy is still significant. This discrepancy comes from interpolation errors in the current algorithm.

C.3.2 Heavy-to-light configuration

When the incident shock travels from a heavy fluid to a light fluid, the initial perturbation undergoes a phase inversion, which significantly affects the process of vorticity deposition

along the interface. Fig. C.9 shows the evolution of the perturbation when the incoming shock traverses the interface for $a_0/\lambda = 0.05,\ 0.1,\ 0.2,\ 0.3$. Compared to the light-to-heavy case, the sign of the baroclinic vorticity is opposite, such that clockwise (counterclockwise) vorticity is generated along the left (respectively, right) half of the perturbation, causing the phase inversion. As a result, a spike of heavy fluid is entrained and falls into the light fluid during the interaction, which causes the interface to be significantly distorted after the passage of the incoming shock, as shown in Fig. C.10a. At this stage in the perturbation growth, the vorticity distribution is not sinusoidal like in the light-to-heavy case0, as shown in Fig. C.10b. As in the light-to-heavy case, we ignore vorticity contributions from transmitted/reflected wave patterns occurring after the passage of the incoming shock, such that vorticity is extracted at $t = 1,\ 2,\ 3,\ 3$ for $a_0/\lambda = 0.05,\ 0.1,\ 0,2,\ 0.3$, respectively. In the heavy-to-light case, the reflected wave is a rarefaction, though the transmitted wave is still a shock that now travels faster than the incoming shock. As a result, vorticity is first generated by the transmitted shock and then by the incoming shock and reflected waves. The Schlieren images of Fig. C.9 show a region of strong density gradient at the location where the incoming shock and reflected waves intersect at the interface, which results in a kink in the vorticity distribution close to the bubble, as shown in figure C.10b. Contrary to the light-to-heavy case, both the sheet-strength magnitude and its profile differ from the SZ model, as shown in Fig. C.11.

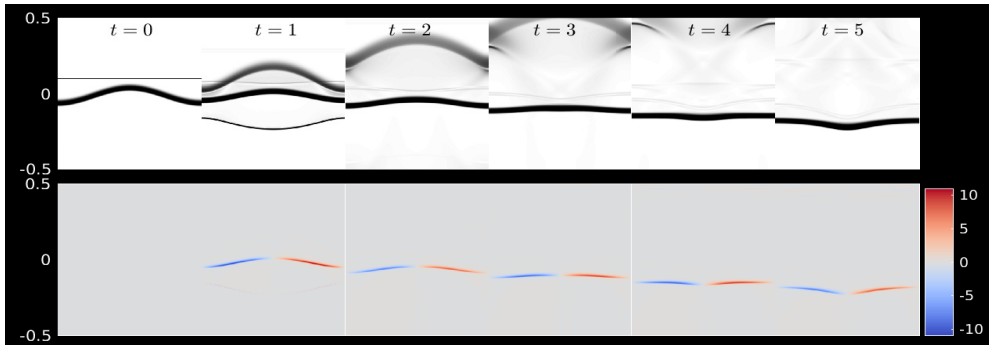

(a)

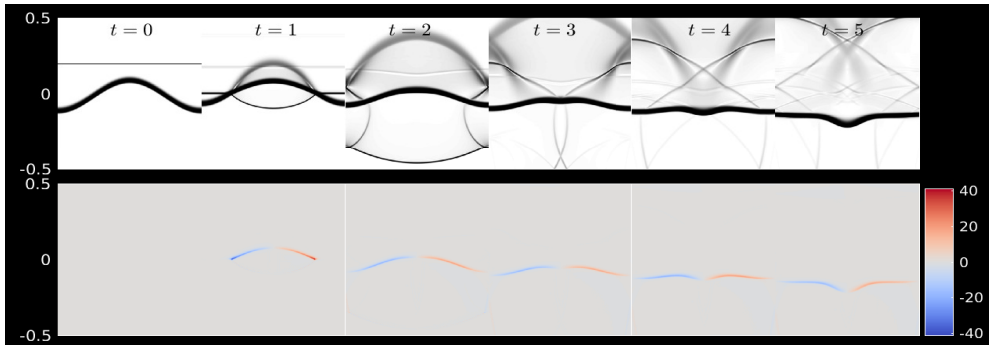

(b)

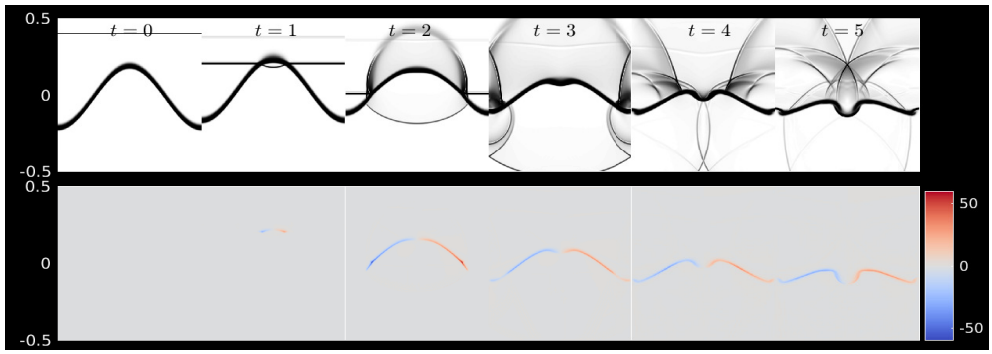

(c)

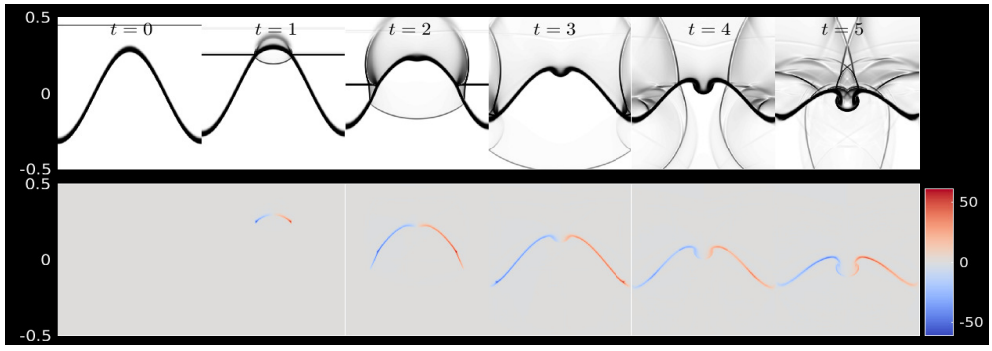

(d)

Figure C.9: Evolution of the perturbation during the interaction with the incoming shock for a heavy/light configuration: (a) $a_0/\lambda = 0.05$, (b) $a_0/\lambda = 0.1$, (c) $a_0/\lambda = 0.2$, (d) $a_0/\lambda = 0.3$. Numerical Schlieren (top) and vorticity contours (bottom).

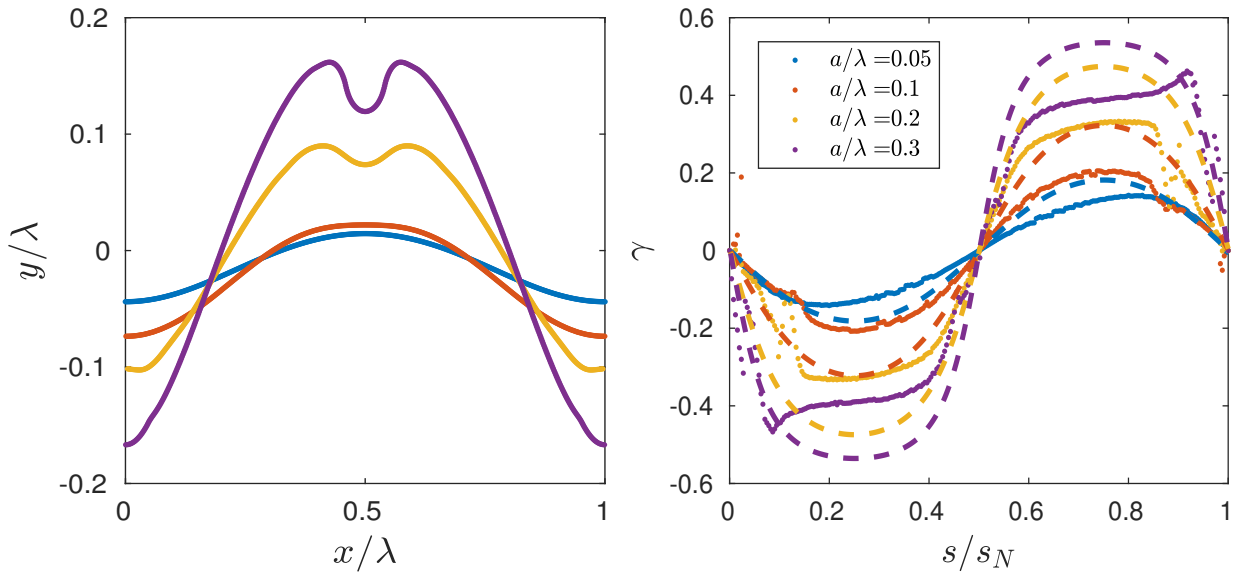

(a) Interface morphology (b) Sheet-strength distribution

Figure C.10: (a) Interface morphology, and (b) sheet-strength distribution vs. arclength, immediately after shock passage for the heavy/light configuration for $a_0/\lambda = 0.05$ ($t = 1$), $a_0/\lambda = 0.1$ ($t = 2$), $a_0/\lambda = 0.2$ ($t = 3$), and $a_0/\lambda = 0.3$ ($t = 4$). Dashed lines: SZ model.

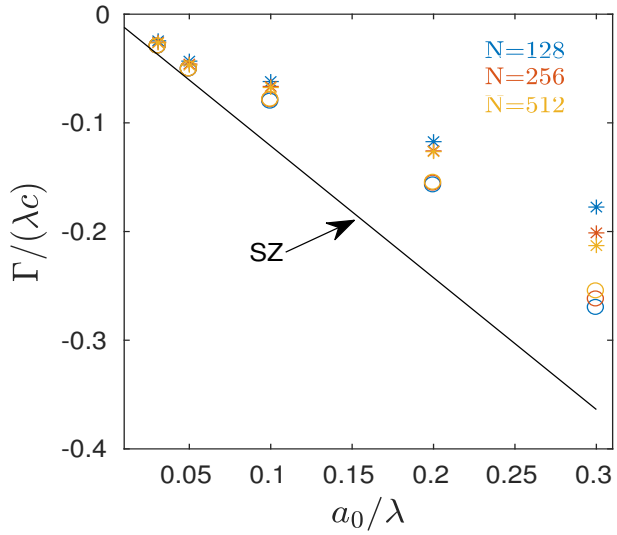

Figure C.11: Circulation along half of the interface immediately after shock passage for a heavy/light configuration for the direct simulations (○), the SZ model (—), and our algorithm (*).

BIBLIOGRAPHY

Abarzhi, S.I., Bhowmick, A.K., Naveh, A., Pandian, A., Swisher, N.C., Stellingwerf, R.F. & Arnett, W.D. 2018 Supernova, nuclear synthesis, fluid instabilities, and interfacial mixing. *Proc. Natl. Acad. Sci.* p. 201714502.

Aglitskiy, Y, Metzler, N, Karasik, M, Serlin, V, Velikovich, AL, Obenschain, SP, Mostovych, AN, Schmitt, AJ, Weaver, J, Gardner, JH & others 2006 Perturbation evolution started by Richtmyer-Meshkov instability in planar laser targets. *Phys. Plasmas* **13** (8), 080703.

Aglitskiy, Y, Velikovich, AL, Karasik, M, Metzler, N, Zalesak, ST, Schmitt, AJ, Phillips, L, Gardner, JH, Serlin, V, Weaver, JL & others 2010 Basic hydrodynamics of Richtmyer-Meshkov-type growth and oscillations in the inertial confinement fusion-relevant conditions. *Philos. Trans. R. Soc. A.* **368** (1916), 1739–1768.

Aleshin, AN, Gamalii, EG, Zaitsev, SG, Lazareva, EV & Lebo, IG. 1988 A study of the nonlinear and transition stages of the evolution of the Richtmyer-Meshkov instability. *Sov. Tech. Phys. Lett.* **14**, 1063–1067.

Alon, U, Hecht, J, Ofer, D & Shvarts, D. 1995 Power laws and similarity of Rayleigh-Taylor and Richtmyer-Meshkov mixing fronts at all density ratios. *Phys. Rev. Lett.* **74** (4), 534.

Andronov, VA, Bakhrakh, SM, Meshkov, EE, Mokhov, VN, Nikiforov, VV, Pevnitskii, AV & Tolshmyakov, AI. 1976 Turbulent mixing at contact surface accelerated by shock waves. *Sov. Phys. JETP* **44** (2), 424–427.

Baker, GR. 1980 A test of the method of Fink & Soh for following vortex-sheet motion. *J. Fluid Mech.* **100** (1), 209–220.

Baker, G, Caflisch, RE & Siegel, M. 1993 Singularity formation during Rayleigh–Taylor instability. *J. Fluid Mech.* **252**, 51–78.

Baker, GR, Meiron, DI & Orszag, SA. 1980 Vortex simulations of the Rayleigh–Taylor instability. *Phys. Fluids* **23** (8), 1485–1490.

Baker, GR, Meiron, DI & Orszag, SA. 1982 Generalized vortex methods for free-surface flow problems. *J. Fluid Mech.* **123**, 477–501.

Balasubramanian, S, Orlicz, GC, Prestridge, KP & Balakumar, BJ. 2012 Experimental study of initial condition dependence on Richtmyer-Meshkov instability in the presence of reshock. *Phys. Fluids* **24** (3), 034103.

Batchelor, GK. 2000 *An introduction to fluid dynamics*. Cambridge University Press.

Benjamin, RF. 1988 Experimental observations of shock stability and shock-induced turbulence. *Tech. Rep.*. Los Alamos National Lab., NM (USA).

Benjamin, RF & Fritz, JN. 1987 Shock loading a rippled interface between liquids of different densities. *Phys. Fluids* **30** (2), 331–336.

Betti, R & Hurricane, OA. 2016 Inertial-confinement fusion with lasers. *Nat. Phys.* **12** (5), 435–448.

Boehly, TR, Brown, DL, Craxton, RS, Keck, RL, Knauer, JP, Kelly, JH, Kessler, TJ, Kumpan, SA, Loucks, SJ, Letzring, SA & others. 1997 Initial performance results of the OMEGA laser system. *Opt. Commun.* **133** (1-6), 495–506.

Bonazza, R. & Sturtevant, B. 1996 X-ray measurements of growth rates at a gas interface accelerated by shock waves. *Phys. Fluids* **8** (9), 2496–2512.

Brouillette, M. 2002 The Richtmyer-Meshkov instability. *Annu. Rev. Fluid Mech.* **34** (1), 445–468.

Brouillette, M. & Sturtevant, B. 1993 Experiments on the Richtmyer–Meshkov instability: Small-scale perturbations on a plane interface. *Phys. Fluids* **5** (4), 916–930.

Brouillette, M & Sturtevant, B. 1994 Experiments on the Richtmyer–Meshkov instability: single-scale perturbations on a continuous interface. *J. Fluid Mech.* **263**, 271–292.

Brueckner, KA & Jorna, S. 1974 Laser-driven fusion. *Rev. Mod. Phys.* **46** (2), 325.

Campbell, EM & Hogan, WJ. 1999 The National Ignition Facility-applications for inertial fusion energy and high-energy-density science. *Plasma Phys. Control. Fusion* **41** (12B), B39.

Castilla, R, Redondo, JM, Youngs, DL, Linden, PF & Dalziel, SB. 1993 Mixing front growth in RT and RM instabilities. In *Proceedings of the 4th International Workshop on the Physics of Compressible Turbulent Mixing*, pp. 11–22.

Chandrasekhar, S. 2013 *Hydrodynamic and hydromagnetic stability*. Courier Corporation.

Charru, F. 2011 *Hydrodynamic instabilities*, , vol. 37. Cambridge University Press.

Chorin, AJ & Bernard, PS. 1973 Discretization of a vortex sheet, with an example of roll-up. *J. Comput. Phys.* **13** (3), 423–429.

Cohen, RH, Dannevik, WP, Dimits, AM, Eliason, DE, Mirin, AA, Zhou, Y, Porter, DH & Woodward, PR 2002 Three-dimensional simulation of a Richtmyer–Meshkov instability with a two-scale initial perturbation. *Phys. Fluids* **14** (10), 3692–3709.

Collins, BD & Jacobs, JW. 2002 Plif flow visualization and measurements of the Richtmyer-Meshkov instability of an air/sf6 interface. *J. Fluid Mech.* **464**, 113.

Cottet, GH, Koumoutsakos, PD & others. 2000 *Vortex methods: theory and practice*. Cambridge University Press.

Di Stefano, CA, Malamud, G, Kuranz, CC, Klein, SR & Drake, RP. 2015*a* Measurement of Richtmyer–Meshkov mode coupling under steady shock conditions and at high energy density. *High Energy Density Phys.* **17**, 263–269.

Di Stefano, CA, Malamud, G, Kuranz, CC, Klein, SR, Stoeckl, C & Drake, RP. 2015*b* Richtmyer-Meshkov evolution under steady shock conditions in the high-energy-density regime. *Appl. Phys. Lett.* **106** (11), 114103.

Di Stefano, CA, Rasmus, AM, Doss, FW, Flippo, KA, Hager, JD, Kline, JL & Bradley, PA. 2017 Multimode instability evolution driven by strong, high-energy-density shocks in a rarefaction-reflected geometry. *Phys. Plasmas* **24** (5), 052101.

Di Stefano, C. A., Doss, F W, Rasmus, A. M., Flippo, K. A. & Haines, B. M. 2019 The modeling of delayed-onset Rayleigh-Taylor and transition to mixing in laser-driven HED experiments. *Phys. Plasmas.* **26** (5), 052708.

Dimonte, G, Frerking, CE, Schneider, M & Remington, B. 1996 Richtmyer–Meshkov instability with strong radiatively driven shocks. *Phys. Plasmas* **3** (2), 614–630.

Dimonte, G & Ramaprabhu, P 2010 Simulations and model of the nonlinear Richtmyer–Meshkov instability. *Phys. Fluids* **22** (1), 014104.

Dimonte, G & Remington, B. 1993 Richtmyer-Meshkov experiments on the Nova laser at high compression. *Phys. Rev. Lett.* **70** (12), 1806.

Doss, FW, Flippo, KA, Merritt, EC, DeVolder, BG, Di Stefano, CA, Huntington, CM, Kline, JL, Kot, L, Nagel, SR, Rasmus, AM & others. 2020 Three-dimensional signatures of self-similarity in a high-energy-density plasma shear-driven mixing layer. *Phys. Plasmas.* **27** (3), 032701.

Doss, FW, Kline, JL, Flippo, KA, Perry, TS, DeVolder, BG, Tregillis, I, Loomis, EN, Merritt, EC, Murphy, TJ, Welser-Sherrill, L & others. 2015 The shock/shear platform for planar radiation-hydrodynamics experiments on the National Ignition Facility. *Phys. Plasmas* **22** (5), 056303.

Doss, FW, Loomis, EN, Welser-Sherrill, L, Fincke, JR, Flippo, KA & Keiter, PA. 2013 Instability, mixing, and transition to turbulence in a laser-driven counterflowing shear experiment. *Phys. Plasmas* **20** (1), 012707.

Drake, RP. 2010 High-energy-density physics. *Phys. Today* **63** (6), 28.

Drake, RP. 2018 *High-energy-density physics: foundation of inertial fusion and experimental astrophysics*. Springer.

Drazin, PG & Reid, WH. 2004 *Hydrodynamic stability*. Cambridge University Press.

Feng, H, Kaganovskiy, L & Krasny, R. 2009 Azimuthal instability of a vortex ring computed by a vortex sheet panel method. *Fluid Dyn. Res.* **41** (5), 051405.

Flippo, KA, Doss, FW, Merritt, EC, DeVolder, BG, Di Stefano, CA, Bradley, PA, Capelli, D, Cardenas, T, Desjardins, TR, Fierro, F & others. 2018 Late-time mixing and turbulent behavior in high-energy-density shear experiments at high Atwood numbers. *Phys. Plasmas.* **25** (5), 056315.

Henry de Frahan, MTH, Movahed, P & Johnsen, E. 2015*a* Numerical simulations of a shock interacting with successive interfaces using the Discontinuous Galerkin method: the multilayered Richtmyer–Meshkov and Rayleigh–Taylor instabilities. *Shock Waves* **25** (4), 329–345.

Henry de Frahan, MT, Varadan, S & Johnsen, E. 2015*b* A new limiting procedure for discontinuous Galerkin methods applied to compressible multiphase flows with shocks and interfaces. *J. Comput. Phys.* **280**, 489–509.

Gittings, M, Weaver, R, Clover, M, Betlach, T, Byrne, N, Coker, R, Dendy, E, Hueckstaedt, R, New, K, Oakes, WR & others. 2008 The RAGE radiation-hydrodynamic code. *Comput. Sci. Discov.* **1** (1), 015005.

Glendinning, S Gail, Bolstad, J, Braun, DG, Edwards, MJ, Hsing, WW, Lasinski, BF, Louis, H, Miles, A, Moreno, J, Peyser, TA & others 2003 Effect of shock proximity on Richtmyer-Meshkov growth. *Phys. Plasmas* **10** (5), 1931–1936.

Goncharov, VN. 2002 Analytical model of nonlinear, single-mode, classical Rayleigh-Taylor instability at arbitrary Atwood numbers. *Phys. Rev. Lett.* **88** (13), 134502.

Gupta, S, Zhang, S & Zabusky, NJ 2003 Shock interaction with a heavy gas cylinder: Emergence of vortex bilayers and vortex-accelerated baroclinic circulation generation. *Laser Part. Beams* **21** (3), 443.

Haines, BM, Grim, GP, Fincke, JR, Shah, RC, Forrest, CJ, Silverstein, K, Marshall, FJ, Boswell, M, Fowler, MM, Gore, RA & others 2016 Detailed high-resolution three-dimensional simulations of OMEGA separated reactants inertial confinement fusion experiments. *Phys. Plasmas* **23** (7), 072709.

Haines, BM, Vold, EL, Molvig, K, Aldrich, C & Rauenzahn, R. 2014 The effects of plasma diffusion and viscosity on turbulent instability growth. *Phys. Plasmas.* **21** (9), 092306.

Harding, EC, Hansen, JF, Hurricane, OA, Drake, RP, Robey, HF, Kuranz, CC, Remington, BA, Bono, MJ, Grosskopf, MJ & Gillespie, RS. 2009 Observation of a Kelvin-Helmholtz instability in a high-energy-density plasma on the omega laser. *Phys. Rev. Lett.* **103** (4), 045005.

Hawley, JF & Zabusky, NJ. 1989 Vortex paradigm for shock-accelerated density-stratified interfaces. *Phys. Rev. Lett.* **63** (12), 1241.

Hecht, J, Alon, U & Shvarts, D. 1994 Potential flow models of Rayleigh–Taylor and Richtmyer–Meshkov bubble fronts. *Phys. Fluids* **6** (12), 4019–4030.

Helmholtz, H. 1868 Xliii. on discontinuous movements of fluids. *Philos. Mag* **36** (244), 337–346, arXiv: https://doi.org/10.1080/14786446808640073.

Henderson, LF. 1989 On the refraction of shock waves. *J. Fluid Mech.* **198**, 365–386.

Hicks, DG, Meezan, NB, Dewald, EL, Mackinnon, AJ, Olson, RE, Callahan, DA, Döppner, T, Benedetti, LR, Bradley, DK, Celliers, PM & others. 2012 Implosion dynamics measurements at the National Ignition Facility. *Phys. Plasmas* **19** (12), 122702.

Higdon, JJL & Pozrikidis, C. 1985 The self-induced motion of vortex sheets. *J. Fluid Mech.* **150**, 203–231.

Hill, DJ, Pantano, C & Pullin, DI 2006 Large-eddy simulation and multiscale modelling of a Richtmyer–Meshkov instability with reshock. *J. Fluid Mech.* **557**, 29–61.

Holmes, RL, Dimonte, G, Fryxell, B, Gittings, ML, Grove, JW, Schneider, M, Sharp, DH, Velikovich, AL, Weaver, RP & Zhang, Q. 1999 Richtmyer–Meshkov instability growth: experiment, simulation and theory. *J. Fluid Mech.* **389**, 55–79.

Hurricane, OA. 2008 Design for a high energy density Kelvin–Helmholtz experiment. *High Energy Density Phys.* **4** (3-4), 97–102.

Jacobs, J.W. 1993 The dynamics of shock accelerated light and heavy gas cylinders. *Phys. Fluids* **5** (9), 2239–2247.

Jacobs, JW & Catton, I. 1988*a* Three-dimensional Rayleigh-Taylor instability part 1. weakly nonlinear theory. *J. Fluid Mech.* **187**, 329–352.

Jacobs, JW & Catton, I. 1988*b* Three-dimensional Rayleigh-Taylor instability part 2. experiment. *J. Fluid Mech.* **187**, 353–371.

Jacobs, JW & Krivets, VV. 2005 Experiments on the late-time development of single-mode Richtmyer–Meshkov instability. *Phys. Fluids* **17** (3), 034105.

Jacobs, JW & Sheeley, JM. 1996 Experimental study of incompressible Richtmyer–Meshkov instability. *Phys. Fluids* **8** (2), 405–415.

Johnson, JR, Wing, S & Delamere, PA. 2014 Kelvin-Helmholtz instability in planetary magnetospheres. *Space Sci. Rev.* **184** (1-4), 1–31.

Jones, MA & Jacobs, JW. 1997 A membraneless experiment for the study of Richtmyer–Meshkov instability of a shock-accelerated gas interface. *Phys. Fluids* **9** (10), 3078–3085.

Kane, J., Arnett, D., Remington, B.A., Glendinning, S.G., Castor, J., Wallace, R., Rubenchik, A. & Fryxell, B.A. 1997 Supernova-relevant hydrodynamic instability experiments on the Nova laser. *Astrophys. J.* **478** (2), L75.

Kerr, RM. 1988 Simulation of Rayleigh-Taylor flows using vortex blobs. *J. Comput. Phys.* **76** (1), 48–84.

Krasny, R. 1986*a* Desingularization of periodic vortex sheet roll-up. *J. Comput. Phys.* **65** (2), 292–313.

Krasny, R. 1986*b* A study of singularity formation in a vortex sheet by the point-vortex approximation. *J. Fluid Mech.* **167**, 65–93.

Krasny, R. 1987 Computation of vortex sheet roll-up in the Trefftz plane. *J. Fluid Mech.* **184**, 123–155.

Krasny, R & Nitsche, M. 2002 The onset of chaos in vortex sheet flow. *J. Fluid Mech.* **454**, 47.

Kuranz, CC, Drake, RP, Harding, EC, Grosskopf, MJ, Robey, HF, Remington, BA, Edwards, MJ, Miles, AR, Perry, TS, Blue, BE & others 2009 Two-dimensional blast-wave-driven Rayleigh-Taylor instability: experiment and simulation. *Astrophys. J.* **696** (1), 749.

Kuranz, CC, Drake, R Paul, Leibrandt, DR, Harding, EC, Robey, HF, Miles, AR, Blue, BE, Hansen, JF, Louis, H, Bono, M & others. 2005 Progress toward the study of laboratory scale, astrophysically relevant, turbulent plasmas. *Astrophys. Space Sci.* **298** (1-2), 9–16.

Kuranz, CC, Park, H-S, Huntington, CM, Miles, AR, Remington, BA, Plewa, T, Trantham, MR, Robey, HF, Shvarts, D, Shimony, A & others. 2018 How high energy fluxes may affect Rayleigh–Taylor instability growth in young supernova remnants. *Nat. Commun* **9** (1), 1–6.

Kuranz, CC, Park, H-S, Remington, BA, Drake, RP, Miles, AR, Robey, HF, Kilkenny, JD, Keane, CJ, Kalantar, DH, Huntington, CM & others. 2011 Astrophysically relevant radiation hydrodynamics experiment at the National Ignition Facility. *Astrophys. Space Sci.* **336** (1), 207–211.

Landau, Lev D. 1944 On the problem of turbulence. *Dokl. Akad. Nauk USSR* **44**, 311–14.

Latini, M, Schilling, O & Don, WS. 2007*a* Effects of WENO flux reconstruction order and spatial resolution on reshocked two-dimensional Richtmyer–Meshkov instability. *J. Comput. Phys.* **221** (2), 805–836.

Latini, M, Schilling, O & Don, WS. 2007*b* High-resolution simulations and modeling of reshocked single-mode Richtmyer-Meshkov instability: Comparison to experimental data and to amplitude growth model predictions. *Phys. Fluids* **19** (2), 024104.

Layzer, D. 1955 On the instability of superposed fluids in a gravitational field. *Astrophys. J. Lett.* **122**, 1.

Lee, D-K, Peng, G & Zabusky, NJ. 2006 Circulation rate of change: A vortex approach for understanding accelerated inhomogeneous flows through intermediate times. *Phys. Fluids* **18** (9), 097102.

Leinov, E, Malamud, G, Elbaz, Y, Levin, LA, Ben-Dor, G, Shvarts, D & Sadot, O 2009 Experimental and numerical investigation of the Richtmyer-Meshkov instability under re-shock conditions. *J. Fluid Mech.* **626**, 449.

LeVeque, R.J. 1992 Numerical methods for conservation laws. *Birkhäuser Basel* .

Levinson, N. 1965 Simplified treatment of integrals of Cauchy type, the Hilbert problem and singular integral equations. appendix: Poincaré-Bertrand formula. *Siam Review* **7** (4), 474–502.

Lindl, J. 1995 Development of the indirect-drive approach to inertial confinement fusion and the target physics basis for ignition and gain. *Phys. Plasmas* **2** (11), 3933–4024.

Lindl, JD, McCrory, RL & Campbell, EM. 1992 Progress toward ignition and burn propagation in inertial confinement fusion. *Phys. Today* **45** (9), 32.

Lombardini, M, Hill, DJ, Pullin, DI & Meiron, DI 2011 Atwood ratio dependence of Richtmyer-Meshkov flows under reshock conditions using large-eddy simulations. *J. Fluid Mech.* **670**, 439–480.

Long, CC, Krivets, VV, Greenough, JA & Jacobs, JW. 2009 Shock tube experiments and numerical simulation of the single-mode, three-dimensional Richtmyer–Meshkov instability. *Phys. Fluids* **21** (11), 114104.

Majda, Andrew J. & Bertozzi, Andrea L. 2001 *Vorticity and Incompressible Flow*. Cambridge University Press.

Malamud, G, Di Stefano, CA, Elbaz, Y, Huntington, CM, Kuranz, CC, Keiter, PA & Drake, RP. 2013*a* A design of a two-dimensional, multimode RM experiment on OMEGA-EP. *High Energ. Dens. Phys.* **9** (1), 122–131.

Malamud, G, Shimony, A, Wan, WC, Di Stefano, CA, Elbaz, Y, Kuranz, CC, Keiter, PA, Drake, RP & Shvarts, D. 2013*b* A design of a two-dimensional, supersonic KH experiment on OMEGA-EP. *High Energ. Dens. Phys.* **9** (4), 672–686.

Marozas, JA, Hohenberger, M, Rosenberg, MJ, Turnbull, D, Collins, TJB, Radha, PB, McKenty, PW, Zuegel, JD, Marshall, FJ, Regan, SP & others 2018 Wavelength-detuning cross-beam energy transfer mitigation scheme for direct drive:

Modeling and evidence from national ignition facility implosions. *Phys. Plasmas* **25** (5), 056314.

Masters, A, Achilleos, N, Bertucci, Cesar, Dougherty, MK, Kanani, SJ, Arridge, CS, McAndrews, HJ & Coates, AJ. 2009 Surface waves on Saturn's dawn flank magnetopause driven by the Kelvin–Helmholtz instability. *Planet. Space Sci.* **57** (14-15), 1769–1778.

Masters, A, Achilleos, N, Kivelson, MG, Sergis, N, Dougherty, MK, Thomsen, MF, Arridge, CS, Krimigis, SM, McAndrews, HJ, Kanani, SJ & others. 2010 Cassini observations of a Kelvin-Helmholtz vortex in Saturn's outer magnetosphere. *J. Geophys. Res. Space Phys.* **115** (A7).

Matsuoka, C & Nishihara, K. 2006*a* Analytical and numerical study on a vortex sheet in incompressible Richtmyer-Meshkov instability in cylindrical geometry. *Phys. Rev. E.* **74** (6), 066303.

Matsuoka, C & Nishihara, K. 2006*b* Fully nonlinear evolution of a cylindrical vortex sheet in incompressible Richtmyer–Meshkov instability. *Phys. Rev. E.* **73** (5), 055304.

Matsuoka, C & Nishihara, K. 2006*c* Vortex core dynamics and singularity formations in incompressible Richtmyer-Meshkov instability. *Phys. Rev. E.* **73** (2), 026304.

Matsuoka, C & Nishihara, K. 2020 Nonlinear interaction between bulk point vortices and an unstable interface with nonuniform velocity shear such as Richtmyer–Meshkov instability. *Phys. Plasmas* **27** (5), 052305.

Matsuoka, C, Nishihara, K & Fukuda, Y. 2003 Nonlinear evolution of an interface in the Richtmyer-Meshkov instability. *Phys. Rev. E.* **67** (3), 036301.

McCrory, RL, Meyerhofer, DD, Betti, R, Craxton, RS, Delettrez, JA, Edgell, DH, Glebov, V Yu, Goncharov, VN, Harding, DR, Jacobs-Perkins, DW & others 2008 Progress in direct-drive inertial confinement fusion. *Phys. Plasmas* **15** (5), 055503.

McFarland, J, Reilly, D, Creel, S, McDonald, C, Finn, T & Ranjan, D. 2014 Experimental investigation of the inclined interface Richtmyer–Meshkov instability before and after reshock. *Exp Fluids.* **55** (1), 1640.

Meezan, NB, MacKinnon, AJ, Hicks, DG, Dewald, EL, Tommasini, R, Le Pape, S, Döppner, T, Ma, T, Farley, DR, Kalantar, DH & others 2013 X-ray driven implosions at ignition relevant velocities on the National Ignition Facility. *Phys. Plasmas* **20** (5), 056311.

Meiron, DI, Baker, GR & Orszag, SA. 1982*a* Analytic structure of vortex sheet dynamics. part 1. Kelvin–Helmholtz instability. *J. Fluid Mech.* **114**, 283–298.

Meiron, Daniel I, Baker, Gregory R & Orszag, Steven A 1982*b* Analytic structure of vortex sheet dynamics. Part 1. Kelvin–Helmholtz instability. *Journal of Fluid Mechanics* **114**, 283–298.

Meshkov, EE. 1969 Instability of the interface of two gases accelerated by a shock wave. *Fluid Dyn.* **4** (5), 101–104.

Mikaelian, KO. 1994 Oblique shocks and the combined Rayleigh–Taylor, Kelvin–Helmholtz, and Richtmyer–Meshkov instabilities. *Phys. Fluids.* **6** (6), 1943–1945.

Moore, DW. 1978 The equation of motion of a vortex layer of small thickness. *Studies in Applied Mathematics* **58** (2), 119–140.

Moore, DW. 1979 The spontaneous appearance of a singularity in the shape of an evolving vortex sheet. *Proc. Math. Phys. Eng. Sci.* **365** (1720), 105–119.

Moore, DW. 1985 Numerical and analytical aspects of Helmholtz instability. In *Theor. App. Mech. Lett.*, pp. 263–274. Elsevier.

Morgan, RV, Aure, R, Stockero, JD, Greenough, JA, Cabot, W, Likhachev, OA & Jacobs, JW. 2012 On the late-time growth of the two-dimensional Richtmyer–Meshkov instability in shock tube experiments. *J. Fluid Mech.* **712**, 354–383.

Moses, EI. 2008 Ignition on the national ignition facility. In *J. Phys. Conf. Ser.*, , vol. 112, p. 012003. IOP Publishing.

Movahed, P & Johnsen, E. 2013 A solution-adaptive method for efficient compressible multifluid simulations, with application to the Richtmyer–Meshkov instability. *J. Comput. Phys.* **239**, 166–186.

Nagel, SR, Raman, KS, Huntington, CM, MacLaren, SA, Wang, P, Barrios, M A, Baumann, T, Bender, JD, Benedetti, LR, Doane, DM & others. 2017 A platform for studying the Rayleigh–Taylor and Richtmyer–Meshkov instabilities in a planar geometry at high energy density at the National Ignition Facility. *Phys. Plasmas* **24** (7), 072704.

Niederhaus, CE & Jacobs, JW. 2003 Experimental study of the Richtmyer–Meshkov instability of incompressible fluids. *J. Fluid Mech.* **485**, 243–277.

Nora, R, Theobald, W, Betti, R, Marshall, FJ, Michel, DT, Seka, W, Yaakobi, B, Lafon, M, Stoeckl, C, Delettrez, J & others. 2015 Gigabar spherical shock generation on the OMEGA laser. *Phys. Rev. Lett.* **114** (4), 045001.

Obenschain, SP, Bodner, SE, Colombant, D, Gerber, K, Lehmberg, RH, McLean, EA, Mostovych, AN, Pronko, MS, Pawley, CJ, Schmitt, AJ & others. 1996 The Nike KrF laser facility: Performance and initial target experiments. *Phys. Plasmas* **3** (5), 2098–2107.

Oron, D, Arazi, L, Kartoon, D, Rikanati, A, Alon, U & Shvarts, D. 2001 Dimensionality dependence of the Rayleigh–Taylor and Richtmyer–Meshkov instability late-time scaling laws. *Phys. Plasmas* **8** (6), 2883–2889.

Patterson, B & Johnsen, E. 2018 Growth of liquid-gas interfacial perturbations driven by acoustic waves. *Phys. Rev. Fluids* **3** (7), 074002.

Pellone, S., Di Stefano, C.A., Rasmus, A.M., Kuranz, C.C. & Johnsen, E. 2021 Vortex-sheet modeling of hydrodynamic instabilities produced by an oblique shock interacting with a perturbed interface in the HED regime. *Phys. Plasmas (accepted)* .

Pellone, S. & Johnsen, E. 2021 Vorticity dynamics of the late-time Richtmyer-Meshkov instability. *Phys. Rev. Fluids (in preparation)* .

Peng, G., Zabusky, N.J. & Zhang, S. 2003 Vortex-accelerated secondary baroclinic vorticity deposition and late-intermediate time dynamics of a two-dimensional Richtmyer–Meshkov interface. *Phys. Fluids.* **15** (12), 3730–3744.

Picone, JM & Boris, JP. 1988 Vorticity generation by shock propagation through bubbles in a gas. *J. Fluid Mech.* **189**, 23–51.

Pozrikidis, C. 2000 Theoretical and computational aspects of the self-induced motion of three-dimensional vortex sheets. *J. Fluid Mech.* **425**, 335–366.

Pozrikidis, C. 2011 *Introduction to theoretical and computational fluid dynamics*. Oxford university press.

Pozrikidis, C & Higdon, JJL 1985 Nonlinear Kelvin-Helmholtz instability of a finite vortex layer. *J. Fluid Mech.* **157**, 225–263.

Ramaprabhu, P, Dimonte, G, Woodward, P, Fryer, C, Rockefeller, G, Muthuraman, K, Lin, P-H & Jayaraj, J 2012 The late-time dynamics of the single-mode Rayleigh-Taylor instability. *Phys. Fluids* **24** (7), 074107.

Ramaprabhu, P, Dimonte, G, Young, YN, Calder, AC & Fryxell, B 2006 Limits of the potential flow approach to the single-mode Rayleigh-Taylor problem. *Phys. Rev. E* **74** (6), 066308.

Rasmus, AM, Di Stefano, CA, Flippo, KA, Doss, FW, Kawaguchi, CF, Kline, JL, Merritt, EC, Desjardins, TR, Cardenas, T, Schmidt, DW & others. 2019 Shock-driven hydrodynamic instability of a sinusoidally perturbed, high-Atwood number, oblique interface. *Phys. Plasmas* **26** (6), 062103.

Rasmus, AM, Di Stefano, CA, Flippo, KA, Doss, FW, Kline, JL, Hager, JD, Merritt, EC, Desjardins, TR, Wan, WC, Cardenas, T & others. 2018 Shock-driven discrete vortex evolution on a high-Atwood number oblique interface. *Phys. Plasmas.* **25** (3), 032119.

Rayleigh, L. 1900 Scientific papers vol 2. *Cambridge Univ. Press* pp. 441–7.

Remington, BA 2005 High energy density laboratory astrophysics. *Plasma Phys. Control. Fusion.* **47** (5A), A191.

Remington, BA, Kane, J, Drake, RP, Glendinning, SG, Estabrook, K, London, R, Castor, J, Wallace, RJ, Arnett, D, Liang, E & others. 1997 Supernova hydrodynamics experiments on the Nova laser. *Phys. Plasmas* **4** (5), 1994–2003.

Remington, Bruce A, Park, Hye-Sook, Casey, Daniel T, Cavallo, Robert M, Clark, Daniel S, Huntington, Channing M, Kuranz, Carolyn C, Miles, Aaron R, Nagel, Sabrina R, Raman, Kumar S & others 2019 Rayleigh–Taylor instabilities in high-energy density settings on the National Ignition Facility. *Proc. Natl. Acad. Sci.* **116** (37), 18233–18238.

Reynolds, O. 1883 Xxix. an experimental investigation of the circumstances which determine whether the motion of water shall be direct or sinuous, and of the law of resistance in parallel channels. *Philos. Trans. Royal Soc.* (174), 935–982.

Richtmyer, RD. 1960 Taylor instability in shock acceleration of compressible fluids. *Commun. Pur. Appl. Math* **13** (2), 297–319.

Rikanati, A, Alon, U & Shvarts, D. 1998 Vortex model for the nonlinear evolution of the multimode Richtmyer-Meshkov instability at low Atwood numbers. *Phys. Rev. E.* **58** (6), 7410.

Roberts, MS & Jacobs, JW. 2016 The effects of forced small-wavelength, finite-bandwidth initial perturbations and miscibility on the turbulent Rayleigh–Taylor instability. *J. Fluid Mech.* **787**, 50–83.

Rosenhead, L. 1931 The formation of vortices from a surface of discontinuity. *Proc. R. Soc. Lond. A* **134** (823), 170–192.

Ryutov, D.D. & Remington, B.A. 2002 Scaling astrophysical phenomena to high-energy-density laboratory experiments. *Plasma Phys. Control. Fusion.* **44** (12B), B407.

Sadot, O, Erez, L, Alon, U, Oron, Dan, Levin, LA, Erez, G, Ben-Dor, G & Shvarts, D 1998 Study of nonlinear evolution of single-mode and two-bubble interaction under Richtmyer-Meshkov instability. *Phys. Rev. Lett.* **80** (8), 1654.

Saffman, PG. 1992 *Vortex dynamics*. Cambridge University Press.

Samtaney, R, Ray, J & Zabusky, NJ. 1998 Baroclinic circulation generation on shock accelerated slow/fast gas interfaces. *Phys. Fluids* **10** (5), 1217–1230.

Samtaney, R & Zabusky, NJ. 1994 Circulation deposition on shock-accelerated planar and curved density-stratified interfaces: models and scaling laws. *J. Fluid Mech.* **269**, 45–78.

Schilling, O, Latini, M & Don, WS. 2007 Physics of reshock and mixing in single-mode Richtmyer-Meshkov instability. *Phys. Rev. E.* **76** (2), 026319.

Shpuntova, G.V, Rodriguez, M., Pellone, S., Austin, J.M & Johnsen, E. 2021 A potential flow model of asymmetric gas cylinder collapse. *J. Fluid Mech (in preparation)* .

Smalyuk, VA, Hansen, JF, Hurricane, OA, Langstaff, G, Martinez, D, Park, H-S, Raman, K, Remington, BA, Robey, HF, Schilling, O & others. 2012 Experimental observations of turbulent mixing due to Kelvin–Helmholtz instability on the OMEGA laser facility. *Phys. Plasmas* **19** (9), 092702.

Sohn, SI. 2004 Vortex model and simulations for Rayleigh-Taylor and Richtmyer-Meshkov instabilities. *Phys. Rev. E.* **69** (3), 036703.

Sohn, SI. 2011 Late-time vortex dynamics of Rayleigh–Taylor instability. *J. Phys. Soc. Japan.* **80** (8), 084401.

Sohn, SI, Yoon, D & Hwang, W. 2010 Long-time simulations of the Kelvin-Helmholtz instability using an adaptive vortex method. *Phys. Rev. E.* **82** (4), 046711.

Sohn, S-I. 2003 Simple potential-flow model of Rayleigh-Taylor and Richtmyer-Meshkov instabilities for all density ratios. *Phys. Rev. E.* **67** (2), 026301.

Stock, MJ. 2006 A regularized inviscid vortex sheet method for three dimensional flows with density interfaces. PhD thesis.

Stock, M.J., Dahm, W.J.A. & Tryggvason, G. 2008 Impact of a vortex ring on a density interface using a regularized inviscid vortex sheet method. *J. Comput. Phys.* **227** (21), 9021–9043.

Taylor, GI. 1950 The instability of liquid surfaces when accelerated in a direction perpendicular to their planes. i. *Proc. R. Soc., Series A.* **201** (1065), 192–196.

Thomson Lord Kelvin, W. 1871 Hydrokinetic solutions and observations. *Philos. Mag* **42** (281), 362–377.

Toro, E.F. 2013 *Riemann solvers and numerical methods for fluid dynamics: a practical introduction*. Springer Science & Business Media.

Tryggvason, G. 1988 Numerical simulations of the Rayleigh-Taylor instability. *J. Comput. Phys.* **75** (2), 253–282.

Tryggvason, G. 1989 Simulation of vortex sheet roll-up by vortex methods. *J.Comput. Phys.* **80** (1), 1–16.

Van Dyke, M. 1982 *An album of fluid motion*. Parabolic Press Stanford.

Vasilenko, AM, Buryakov, OV, Kuropatenko, VF, Olkhovskaya, VI, Ratnikov, VP & Jakovlev, VG. 1992 Experimental research of gravitational instability and turbulization of flow at the noble gases interface. *Tech. Rep.*.

Vorobieff, P, Mohamed, N-G, Tomkins, C, Goodenough, C, Marr-Lyon, M & Benjamin, RF. 2003 Scaling evolution in shock-induced transition to turbulence. *Phys. Rev. E* **68** (6), 065301.

Vorobieff, P, Tomkins, C, Kumar, S, Goodenough, C, Mohamed, NG & Benjamin, RF 2004 Secondary instabilities in shock-induced transition to turbulence. *Advances in Fluid Mechanics* **45**.

Wadas, MJ & Johnsen, E 2020 Interactions of two bubbles along a gaseous interface undergoing the Richtmyer-Meshkov instability in two dimensions. *Physica D: Nonlinear Phenomena* p. 132489.

Waitz, lA, Marble, FE & Zukoski, EE. 1993 Investigation of a contoured wall injector for hypervelocity mixing augmentation. *AIAA journal* **31** (6), 1014–1021.

Wan, WC, Malamud, Guy, Shimony, A, Di Stefano, CA, Trantham, MR, Klein, SR, Shvarts, D, Drake, RP & Kuranz, CC. 2017 Observation of dual-mode, Kelvin-Helmholtz instability vortex merger in a compressible flow. *Phys. Plasmas* **24** (5), 055705.

Wan, WC, Malamud, Guy, Shimony, A, Di Stefano, CA, Trantham, MR, Klein, SR, Shvarts, D, Kuranz, CC & Drake, RP. 2015 Observation of single-mode, Kelvin-Helmholtz instability in a supersonic flow. *Phys. Rev. Lett.* **115** (14), 145001.

Wouchuk, JG & Nishihara, K. 1996 Linear perturbation growth at a shocked interface. *Phys. Plasmas* **3** (10), 3761–3776.

Wouchuk, JG & Nishihara, K. 1997 Asymptotic growth in the linear Richtmyer–Meshkov instability. *Phys. Plasmas* **4** (4), 1028–1038.

Wu, JZ. 1995 A theory of three-dimensional interfacial vorticity dynamics. *Phys. Fluids* **7** (10), 2375–2395.

Wu, JZ, Ma, HY & Zhou, MD. 2007 *Vorticity and vortex dynamics*. Springer Science & Business Media.

Wu, JZ, Yang, YT, Luo, YB & Pozrikidis, C. 2005 Fluid kinematics on a deformable surface. *J. Fluid Mech.* **541**, 371.

Yang, J, Kubota, T & Zukoski, EE. 1994*a* A model for characterization of a vortex pair formed by shock passage over a light-gas inhomogeneity. *J. Fluid Mech.* **258**, 217–244.

Yang, Y, Zhang, Q & Sharp, DH. 1994*b* Small amplitude theory of Richtmyer–Meshkov instability. *Phys. Fluids* **6** (5), 1856–1873.

Yule, AJ, Chigier, NA, Ralph, S, Boulderstone, R & Ventura, J. 1981 Combustion-transition interaction in a jet flame. *AIAA Journal* **19** (6), 752–760.

Zabusky, NJ. 1999 Vortex paradigm for accelerated inhomogeneous flows: Visiometrics for the Rayleigh-Taylor and Richtmyer-Meshkov environments. *Annu. Rev. Fluid Mech.* **31** (1), 495–536.

Zabusky, NJ, Kotelnikov, AD, Gulak, Y & Peng, G. 2003 Amplitude growth rate of a Richtmyer–Meshkov unstable two-dimensional interface to intermediate times. *J. Fluid Mech.* **475**, 147–162.

Zabusky, NJ & Zeng, SM 1998 Shock cavity implosion morphologies and vortical projectile generation in axisymmetric shock–spherical fast/slow bubble interactions. *J. Fluid Mech.* **362**, 327–346.

Zabusky, NJ & Zhang, S 2002 Shock–planar curtain interactions in two dimensions: Emergence of vortex double layers, vortex projectiles, and decaying stratified turbulence. *Phys. Fluids* **14** (1), 419–422.

Zhang, Q & Sohn, S-I. 1996 An analytical nonlinear theory of Richtmyer-Meshkov instability. *Phys. Lett. A.* **212** (3), 149–155.

Zhang, Qiang & Sohn, S-I. 1997*a* Nonlinear theory of unstable fluid mixing driven by shock wave. *Phys. Fluids* **9** (4), 1106–1124.

Zhang, Q & Sohn, S-I. 1997*b* Padé approximation to an interfacial fluid mixing problem. *Appl. Math. Lett.* **10** (5), 121–127.

Zhang, S & Zabusky, NJ 2003 Shock-planar curtain interactions: Strong secondary baroclinic deposition and emergence of vortex projectiles and late-time inhomogeneous turbulence. *Laser Part. Beams* **21** (3), 463.

Zhou, Ye. 2017*a* Rayleigh–Taylor and Richtmyer–Meshkov instability induced flow, turbulence, and mixing. i. *Phys. Rep.* **720**, 1–136.

Zhou, Ye. 2017*b* Rayleigh–Taylor and Richtmyer–Meshkov instability induced flow, turbulence, and mixing. ii. *Phys. Rep.* **723**, 1–160.

Zufiria, JA. 1988 Vortex-in-cell simulation of bubble competition in a Rayleigh–Taylor instability. *Phys. Fluids* **31** (11), 3199–3212.